UNIVERSITEIT VAN PRETORIA
UNIVERSITY OF PRETORIA
YUNIBESITHI YA PRETORIA

OPTIMISING PRESSURE PROFILES IN SUPERPLASTIC FORMING

by

Marlise Sunné Cowley

Submitted in partial fulfillment of the requirements for the degree

Master of Engineering (Mechanical Engineering)

in the

Department of Mechanical and Aeronautical Engineering
Faculty of Engineering, Built Environment and Information Technology
UNIVERSITY OF PRETORIA

February 2017

SUMMARY

OPTIMISING PRESSURE PROFILES IN SUPERPLASTIC FORMING

by

Marlise Sunné Cowley

Supervisor:	Prof Schalk Kok (University of Pretoria)
Industry mentor:	Mr Gary Corderley (Council for Scientific and Industrial Research)
Department:	Mechanical and Aeronautical Engineering
University:	University of Pretoria
Degree:	MEng (Mechanical Engineering)
Keywords:	optimisation, superplastic forming, material model, radial basis function, metamodel

Some metals, such as Ti-6Al-4V, have a high elongation to failure when strained at certain rates and temperatures. Superplastic forming is the utilisation of this property, and it can be used to form thin, geometrically complex components. Superplastic forming is a slow process, and this is one of the reasons why it is an expensive manufacturing process. Localised thinning occurs if the specimen is strained too quickly, and components with locally thin wall thickness fail prematurely. The goal of this study is to find a technique that can be used to minimise the forming time while limiting the minimum final thickness.

The superplastic forming process is investigated with the finite element method. The finite element method requires a material model which describes the superplastic behaviour of the metal. Several material models are investigated in order to select a material model that can show localised thinning at higher strain rates. The material models are calibrated with stress-strain data, grain size-time data and strain rate sensitivity-strain data. The digitised data from literature is for Ti-6Al-4V with three different initial grain sizes strained at different strain rates at 927°C.

The optimisation of the forming time is done with an approximate optimisation algorithm.

This algorithm involves fitting a metamodel to simulated data, and using the metamodels to find the optimum instead of using the finite element model directly. One metamodel is fitted to the final forming time results, and another metamodel is fitted to the final minimum thickness results.

A regressive radial basis function method is used to construct the metamodels. The interpolating radial basis function method proved to be unreliable at the design space boundaries due to non-smooth finite element results. The non-smooth results are due to the problem being path dependent.

The final forming time of the superplastic forming of a rectangular box was successfully minimised while limiting the final minimum thickness. The metamodels predicted that allowing a 4% decrease in the minimum allowable thickness (1.0 mm to 0.96 mm) and a 1 mm gap between the sheet and the die corner the forming time is decreased by 28.84%. The finite element verification indicates that the final minimum thickness reduced by 3.8% and that the gap between the sheet and the die corner is less than 1 mm, resulting in the forming time being reduced by 28.81%.

TABLE OF CONTENTS

LIST OF FIGURES

LIST OF TABLES

LIST OF SYMBOLS

Acronyms

CPU	Central Processing Unit
DACE	Design and Analysis of Computer Experiments
DOE	Design Of Experiments
FEM	Finite Element Method
lb	Lower Bounds
LOOCV	Leave-One-Out Cross-Validation
MARS	Multivariate Adaptive Regression Splines
RBF	Radial Basis Function
Res	Residual
RMSE	Root Mean Square Error
SV	State Variable
ub	Upper Bounds

Greek Letters

α_1	Constant [$\mathrm{m{\cdot}s^{-1}}$]

α_2	Constant [s^{-1}]
β	Constant
β_1	Constant [$m \cdot s^{-1}$]
β_2	Constant [Pa]
γ	Constant [m·s]
γ_0	Constant [s^{-1}]
$\boldsymbol{\sigma'}$	Deviatoric component of the Cauchy stress tensor [Pa]
$\boldsymbol{\sigma}$	Cauchy stress tensor [Pa]
$\dot{\bar{\varepsilon}}$	Equivalent strain rate [s^{-1}]
$\dot{\varepsilon}$	Strain rate [s^{-1}]
ε	Strain
θ	Angle between the slip plane normal and the load direction [degrees or radians]
μ	Shear modulus [Pa]
ν	Poisson's ratio
$\bar{\sigma}$	Equivalent stress [Pa]
σ	Stress [Pa]
$\sigma_\star$	Threshold stress [Pa]
τ	Resolved shear stress [Pa]
τ	Shear stress [Pa]
ϕ	Constant [s^{-1}]

φ Angle between the slip plane and the load direction [degrees or radians]

Roman Letters

a Grain growth exponent [$\mathrm{kg \cdot m^{-2} \cdot s^{-2}}$]

A Constant [$\mathrm{s^{-1}}$]

b Burgers vector [m]

b Constant [Pa]

a_1 Constant [$\mathrm{s^{-1}}$]

a_2 Constant [$\mathrm{s^{-1}}$]

a_3 Constant [$\mathrm{kg \cdot m^{-1} \cdot s^{-1}}$]

c_1 Constant [$\mathrm{kg \cdot m^{-1} \cdot s^{-1}}$]

c_2 Constant [$\mathrm{s^{-1}}$]

c_3 Constant [$\mathrm{s^{-1}}$]

c_4 Constant [$\mathrm{s^{-1}}$]

c_5 Constant [$\mathrm{kg \cdot m^{-1} \cdot s^{-1}}$]

$\boldsymbol{D'}$ Deviatoric component of the deformation tensor [$\mathrm{m \cdot s^{-2}}$]

$\boldsymbol{D}$ Rate of deformation tensor [$\mathrm{m \cdot s^{-2}}$]

$\mathcal{D}$ Coefficient of diffusion [$\mathrm{m^2 \cdot s^{-1}}$]

d Grain size [m]

E Young's modulus [Pa]

E Young's modulus [Pa]

e	Error
f	Function
$\mathcal{g}$	Inequality constraint
g	Gap [m]
$\mathcal{h}$	Equality constraint
h	Thickness [m]
$\boldsymbol{I}$	Identity matrix
K	Constant [Pa]
k	Constant [Pa]
L	Length [m]
L	Length [m]
m	Strain rate sensitivity [$\mathrm{kg{\cdot}m^{-1}{\cdot}s^{-1}}$]
N	Normal of a plane
n	Strain hardening exponent [Pa]
p	Pressure [Pa]
Q	Constant [Pa]
q	Activation energy [J]
$\mathcal{R}$	Universal gas constant [$\mathrm{J{\cdot}(mol \cdot K)^{-1}}$]
R	Isotropic hardening [Pa]
r	Ratio

S	Schmidt factor
T	Temperature [°C or K]
t	Time [s]
v	Speed [m·s]
w	Weight factor
$\boldsymbol{x}$	Design vector

Superscripts

$^{\mathsf{T}}$	Transpose
sp	Superplastic

Subscripts

d	Grain size [m]
diff.	Diffusion
disloc.	Dislocation movement
e	Elastic
gb	Grain boundary
L	Lattice diffusion
N	Normal
p	Plastic
R	Isotropic hardening [Pa]
T	Total

vol Volumetric component

CHAPTER 1

INTRODUCTION

1.1 PROBLEM STATEMENT

Superplasticity is the high elongation to failure that some metals exhibit when strained at certain strain rates and temperatures [1]. The utilisation of this property is called superplastic forming, and this process can be used to form thin, geometrically complex components such as dental prostheses [2]. Superplastic forming is however a slow process, which is one of the reasons why it is an expensive manufacturing process. Localised thinning takes place if the sheet metal is strained too quickly [3], and the formed component will fail prematurely if there is excessive thinning.

1.2 OBJECTIVE

The objective of this study is to find a technique that can be used to minimise the forming time of the superplastic forming of a rectangular box while limiting the final minimum thickness.

1.3 CONTEXT

Superplastic forming can be investigated with the finite element method. The finite element method requires a material model that describes superplastic behaviour. The material model must be able to show the onset of localised thinning at higher strain rates in order to investigate how the forming time of the superplastic forming process can be minimised.

1.4 SCOPE

The stress-strain, strain rate sensitivity-strain and grain size-time data of Ghosh and Hamilton [4] are used to calibrate the material models. Ghosh and Hamilton [4] investigated the superplastic forming of Ti-6Al-4V sheet at 927°C. The material models investigated consist only of a flow rule i.e. the equivalent plastic strain rate as a function of the Von Mises equivalent stress.

1.5 RESEARCH GAP

The research gap is that the forming time of a superplastic forming process has not yet been successfully minimised. Several authors [5, 6, 7] have used an adaptive optimisation strategy to optimise superplastic forming. The adaptive strategy changes the pressure applied to the forming sheet such that a target strain rate is maintained in the forming sheet. This approach to optimising superplastic forming is not necessary since a high strain rate sensitivity is not required during the first stages of forming but later during the forming process [8, 9]. Nazzal, *et al.* [9] and Sorgente and Tricarico [10] also used an adaptive optimisation strategy to optimise a superplastic forming process, but only the strain rate of the area of the most deformation is controlled instead of strain rate of the whole sheet.

An approximate optimisation algorithm is used during this study in order to minimise the forming time directly. An approximate optimisation algorithm involves constructing metamodels from the results of finite element analyses. The metamodels are then used to minimise the final forming time.

1.6 THESIS OVERVIEW

Chapter 2 gives background on superplastic deformation and failure. Different superplastic material models are also discussed this chapter. Different material models are implemented, calibrated and compared in Chapter 3. The material model sensitivity to strain rate is investigated.

The optimisation of the pressure profile of a superplastic forming of a rectangular box is done in Chapter 4. A two dimensional optimisation problem is used to demonstrate the

minimisation of the forming time.

The contributions of the research are reviewed, and possible directions for future research are listed in Chapter 5.

CHAPTER 2

BACKGROUND TO SUPERPLASTICITY

2.1 INTRODUCTION

The goal of this chapter is to discuss the superplastic behaviour of metals at strain rates that are considered on the high end for this forming technique. The different types of superplastic material models that can be used in finite element analyses are also discussed.

2.2 SUPERPLASTIC METALS

Superplasticity is the almost neck-free elongation of several hundreds of per cent that can be observed in some metals when the metal is strained at a certain rate and temperature. This is due to a high strain rate sensitivity. Two types of superplasticity can be observed in metals [1], namely

1. Structural superplasticity

2. Environmental superplasticity

The microstructural characteristics of structural superplasticity are given in Table 2.1. These characteristics can be achieved through processes such as cold or warm working followed by recrystallisation, amongst other processes [11]. Some of these processes are complex and expensive, and some materials that exhibit these microstructural characteristics have novel compositions. Commercially available superplastic metals include Ti-6Al-4V, IN 100, Supral and AA 700 series alloys [11]. Structural superplasticity is utilised with superplastic forming. Superplastic forming is a sheet metal forming process that is performed at high temperatures

which is typically half the melting temperature.

Table 2.1: Microstructural characteristics of structural superplasticity [11]

Microstructural charactristic	Reason for characteristic
A grain size of typically smaller than 10 µm in diameter.	Small grains have a low flow stress and an increased strain rate sensitivity at high temperatures.
High-angle, equiaxed grains.	Promotes grain boundary sliding.
The presence of a second phase material.	The second or β phase material retards grain growth. The amount of α and β phase at high temperature affects the strain rate sensitivity.
The strength of the second phase material is of the same order as that of the matrix. If the second phase is hard, then it is finely dispersed throughout the matrix.	Prevents internal cavitation during superplastic forming.
The grain boundaries are resistant to tensile separation.	Some fine grain polycrystalline ceramics have strain rate sensitivities close to unity, but they are not superplastic materials due to tensile separation at the grain boundaries.

Environmental superplasticity occurs under special conditions such as temperature cycling under a small applied stress [1].

2.3 FAILURE

The relationship between logarithmic flow stress, $\log \sigma$, and logarithmic strain rate, $\log \dot{\varepsilon}$, for superplastic metals during uniaxial tensile tests has a sigmoid shape at high temperatures [1, 12, 13]. A typical sigmoid curve is given in Figure 2.1. The strain rate sensitivity m is defined as the slope of the sigmoid curve [14]

$$m = \frac{\partial \log \sigma}{\partial \log \dot{\varepsilon}} \ . \tag{2.1}$$

The strain rate sensitivity is plotted against logarithmic strain rate in Figure 2.2.

Figures 2.1 and 2.2 are divided into three strain rate regions. Region I is the high strain rate

region, region II is the superplastic strain rate region, and region III is the low strain rate region. Region II has the highest strain rate sensitivity whereas the strain rate sensitivity decreases in regions I and III.

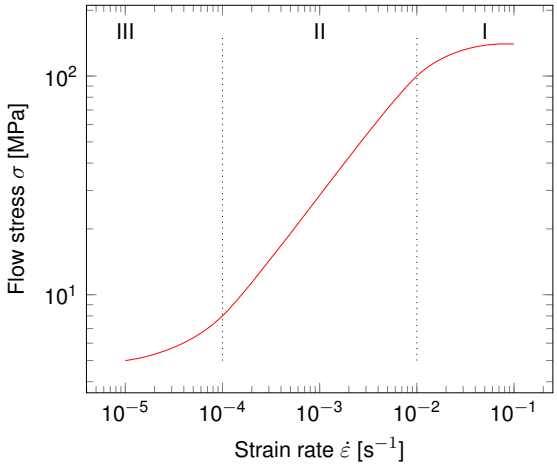

Figure 2.1: Sigmoid relationship between $\log \sigma$ and $\log \dot{\varepsilon}$

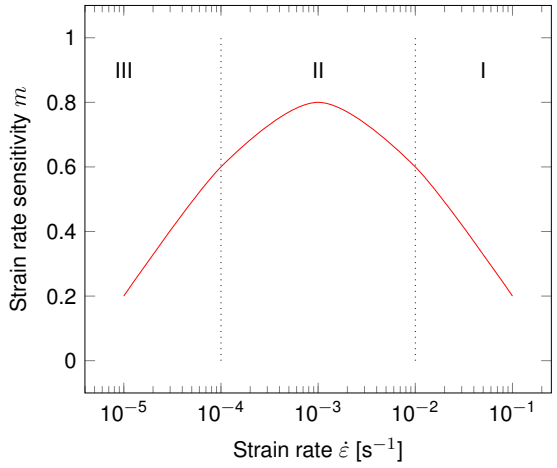

Figure 2.2: Strain rate sensitivity as the slope of the $\log \sigma$-$\log \dot{\varepsilon}$ curve

Figure 2.3 shows a high elongation to failure in region II. The high elongation to failure in region II is linked to a high strain rate sensitivity [15]. The elongation to failure is lower in strain rate regions I and III. It can also be observed from Figure 2.3 that the maximum elongation to failure decreases with decreasing forming temperature.

Although the high elongation to failure can be correlated to a high strain rate sensitivity, the

strain rate sensitivity is not a sufficient parameter for obtaining the optimum superplastic ductility. Langdon [3] found that the gauge length of the tensile test specimen plays an important role in superplastic ductility. Short gauge lengths are more favourable for quasi-stable plastic flow.

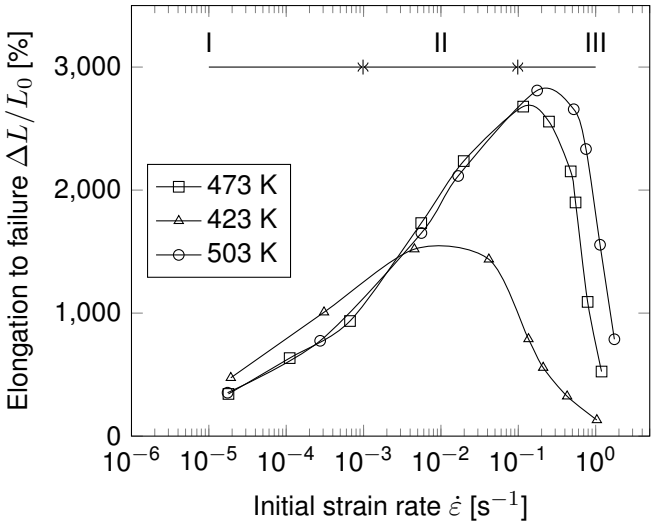

Figure 2.3: Elongation to failure versus initial strain rate for superplastic Zn-22Al eutectoid alloy with an average initial grain size of 2.5 µm [3]

The tensile test specimen fails in a different way for each of the strain rate regions [3]. The three regions and their failure types are given in Table 2.2. The two factors that control superplastic failure under any selected test conditions are the strain rate sensitivity, which dominates necking failure, and the ease of internal cavity interlinkage [3].

Table 2.2: Superplastic failure types with their associated strain rate regions [3]

Failure type	Strain rate region
Failure by quasi-stable flow of material	II
Failure by necking	I and III
Failure by cavitation	I, II and III
Quasibrittle failure	I

Optimal superplastic behaviour occurs when failure is by quasi-stable flow. The deformation in region II is uniform and the material stretches to a fine point. The elongation to failure

is high for quasi-stable flow, and the neck is diffuse. Localised necking and internal cavity interlinkage are suppressed during quasi-stable flow.

The stress in the gauge section is not redistributed during localised necking. The deformation is not uniform and the elongation is restricted to the necked area during localised necking [3].

Cavitation failure can occur in all three strain rate regions to different degrees of severity, but it is the most likely to occur at lower strain rates [3]. Langdon [3] found that cavitation failure actually occurs during the interlinkage of cavities and to a lesser extent due to cavity formation and growth. Failure by cavitation interlinkage is abrupt with a little or no necking. The damaging effect of cavitation can be observed in Figure 2.4. Cavitation failure is not investigated in this study. A superplastic material model that accounts for hardening, softening and damage has been proposed by Alabort, *et al.* [16].

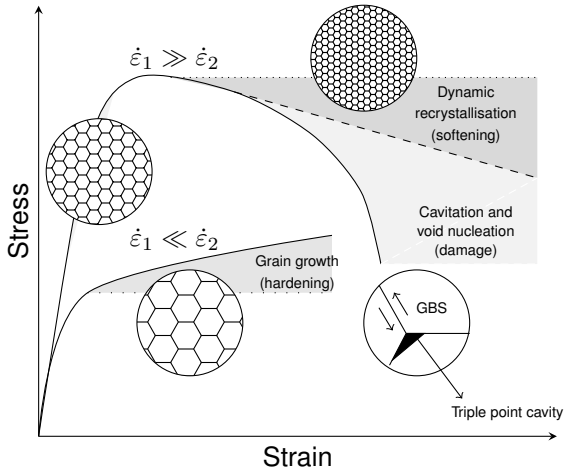

Figure 2.4: Mechanisms during hot deformation of Ti-6Al-4V [16]

Quasi-brittle failure occurs at low temperatures and high strain rates. It has, for example, been observed for Zn-22Al at 423 K that failed at approximately 70% strain at an initial strain rate of 1.33 s^{-1} [3]. Quasi-brittle failure is not investigated in this study.

2.4 SUPERPLASTIC FORMING

Superplasticity can be utilised to form components. Forming techniques include vacuum forming, blow forming and drape forming [1]. The focus of this study is superplastic blow forming. Superplastic blow forming starts by heating the die and the sheet metal to superplastic temperatures in an inert gas atmosphere. Gas pressure is then used to push the sheet until it conforms to the die surface [17].

Superplastic forming can be used to form thin, geometrically complex components for the automotive, aerospace, medical, construction and rail industries. The Ford Motor Company used superplastic forming to produce body panels for the Ford GT [18]. Li and Soo [2] made a dental prosthesis from Ti-6Al-4V alloy using superplastic forming. Superplastic forming has also been used to manufacture panels for the Las Vegas monorail [18].

Superplastic forming together with diffusion bonding has been used to manufacture sandwich panels for airplane wings [11]. Diffusion bonding is a solid state bonding process where the two bonded faces cannot be distinguished at high magnification after bonding. This leads to a very strong bond, because it has little to no inherent stress concentrations, unlike conventionally welded joints.

Superplastic forming has many advantages as a manufacturing technique, but this forming process is not widely used due to a number of drawbacks. Some of the advantages and disadvantages of superplastic forming are summarised in Table 2.3.

Table 2.3: Advantages and disadvantages of superplastic forming [17]

Advantages	Disadvantages
Low stress forming process (< 10 MPa) to achieve large strains.	High working temperature ($\sim 0.5T_{\text{melt}}$) and inert gas atmosphere required.
Used to form large, as well as small, complex, thin components with little to no springback. Good dimensional accuracy.	Superplastic metals are usually expensive. Superplastic forming is a slow process due to the low strain rates.
Formed components usually have a good surface finish that requires little to no machining.	Expensive dies and tooling required.

The high tooling cost for superplastic forming may be justified if superplastic forming can be done at higher strain rates and more components can be produced for the same time.

2.5 MATERIAL MODELS

Superplastic behaviour can be described with a material model when utilizing the finite element method to simulate superplastic forming. A material model should have the ability to show the correct behaviour outside the fitted data range in order to produce the correct material behaviour during a simulation where the forming time is minimised.

There are two types of material models, namely

1. Phenomenological models

2. Micro-mechanical models

Phenomenological models are functions which best fit measured data with the fewest number of variables. Phenomenological models are usually fitted to uniaxial tensile test data, and they need to be modified for use in multi-axial finite element models. Micro-mechanical models are derived from the first principals of thermodynamics and continuum mechanics. Micro-mechanical models are formulated in three dimensions.

2.5.1 Phenomenological models

The functional form of the uniaxial flow stress σ as a function f of strain ε, strain rate $\dot{\varepsilon}$ and grain size d is given by [19]

$$\sigma = f(\varepsilon, \dot{\varepsilon}, d) \ , \tag{2.2}$$

or in logarithmic form

$$\log(\sigma) = F(\log(\varepsilon), \log(\dot{\varepsilon}), \log(d)) \ . \tag{2.3}$$

Eq. (2.3) may take a power law form, which is given by

$$\sigma = K\varepsilon^n \dot{\varepsilon}^m d^a \ , \tag{2.4}$$

where K, n, m and a are constants, when Taylor's series expansion at a given equilibrium state is used and higher order terms are ignored [5, 7, 19]. The constant m is the strain rate

sensitivity that is defined by Eq. (2.1). The strain hardening exponent n is defined as

$$n = \frac{\partial \log \sigma}{\partial \log \varepsilon} \ , \tag{2.5}$$

and the grain growth exponent a is defined as

$$a = \frac{\partial \log \sigma}{\partial \log d} \ . \tag{2.6}$$

The superplastic flow stress σ has been found to have a strong dependence on strain rate $\dot{\varepsilon}$ and a weaker dependence on strain ε and grain size d [6, 19]. Eq. (2.4) can therefore be simplified to

$$\sigma = K\dot{\varepsilon}^m \ . \tag{2.7}$$

Some of the early phenomenological superplastic material models were based on the deformation mechanisms that result in superplastic behaviour. The main deformation mechanism responsible for the high elongation to failure in the superplastic strain rate region is grain boundary sliding. Grain boundary sliding occurs when one grain shears over an adjacent grain [1, 13]. Grains cannot however slide over each other without leaving voids or creating distortion. It is known that localised necking is suppressed during quasi-stable flow, and therefore grain boundary sliding is accompanied by some other mechanism. Grain boundary sliding is usually accompanied by diffusion and/or dislocation movement. One example of a deformation mechanism-based material model is the Ball-Hutchison equation which is based on grain boundary sliding accommodated by dislocation climb [19]

$$\dot{\varepsilon} = K \left(\frac{b}{d}\right)^2 \mathcal{D}_{\text{gb}} \left(\frac{\sigma}{E}\right)^2 \ , \tag{2.8}$$

where K is a constant, b is Burgers vector, $\mathcal{D}_{\text{gb}}$ is the coefficient of grain boundary diffusion, and E is Young's modulus. Deformation mechanism models usually have a power law form with a fixed strain rate sensitivity.

Phenomenological models are usually fitted to uniaxial tensile test data. A flow criterion can be used to convert the kinetic and kinematic quantities of a phenomenological model into equivalent quantities in order to use the uniaxial material model in multi-axial finite element analyses [17]. The flow criterion defines the onset of plastic flow under a multi-axial stress state. Plastic flow starts when the stress in the material is equal to the yield stress of the material.

The Von Mises flow criterion states that flow stress depends only on the deviatoric stress component and not on the hydrostatic stress component. The equivalent form of the power law model given in Eq. (2.7) can then be written as

$$\bar{\sigma} = K\dot{\bar{\varepsilon}}^m \ , \tag{2.9}$$

where the Von Mises equivalent flow stress $\bar{\sigma}$ and strain rate $\dot{\bar{\varepsilon}}$ are given by [17]

$$\bar{\sigma}^2 = \frac{3}{2}\boldsymbol{\sigma'} : \boldsymbol{\sigma'} \ , \tag{2.10}$$

and

$$\dot{\bar{\varepsilon}}^2 = \frac{2}{3}\boldsymbol{D'} : \boldsymbol{D'} \ , \tag{2.11}$$

respectively. The deviatoric component of the Cauchy stress tensor $\boldsymbol{\sigma'}$ is given by

$$\boldsymbol{\sigma} = \boldsymbol{\sigma'} + \sigma_{\text{mean}}\boldsymbol{I} \ , \tag{2.12}$$

where σ_{mean} is the hydrostatic or mean stress and $\boldsymbol{I}$ is the identity matrix. The deviatoric component of the rate of deformation tensor $\boldsymbol{D'}$ is given by

$$\boldsymbol{D} = \boldsymbol{D'} + \frac{1}{3}I_{\text{vol}}\boldsymbol{I} \ , \tag{2.13}$$

where I_{vol} is the volumetric component of the rate of deformation tensor. The rate of deformation tensor $\boldsymbol{D}$ is the symmetric part of the velocity gradient $\nabla\boldsymbol{v}$ which is given by

$$\boldsymbol{D} = \frac{1}{2}(\nabla\boldsymbol{v}^{\intercal} + \nabla\boldsymbol{v}) \ . \tag{2.14}$$

2.5.2 Micro-mechanical models

Micro-mechanical models are derived from the microscopic or grain level and extended to the macroscopic or matrix level. It is known that the primary strain-producing mechanism in superplastic deformation is grain boundary sliding, and the total strain is driven by the strain rate of the accommodating mechanisms such as grain boundary diffusion and dislocation creep. Chandra, *et al.* [19] developed a micro-mechanical material model to describe superplastic deformation. Their model for dual phase materials, which they validated against test data for Ti-6Al-4V, is described below as a example of a micro-mechanical model.

Each grain is viewed as an inclusion or single crystal in an infinite matrix. This is shown in Figure 2.5. The polycrystal or matrix is subjected to a constant strain rate in Figure 2.5. The stress tensor of the inclusion is given by $\boldsymbol{\sigma}$ and the superplastic strain tensor of the inclusion is given by $\boldsymbol{\varepsilon}^{\mathrm{sp}}$. The stress tensor of the matrix is given by $\bar{\boldsymbol{\sigma}}$ and the superplastic strain tensor of the matrix is given by $\bar{\boldsymbol{\varepsilon}}^{\mathrm{sp}}$. The resolved shear stress τ on the k-th slip plane of the inclusion in the case of uniaxial loading is also shown in Figure 2.5.

The superplastic strain rate is only dependent on the current stress. The grains that are aligned with the applied stress will deform more easily and relieve stress in the polycrystal. The stress is then redistributed to the grains in less favourable orientations. The stress redistribution process is a heterogeneous process due to the different grain orientations. This is true even when a constant stress is applied to the polycrystal. The local stress affects the accommodation activity. The amount of accommodation activity of the grains in turn affects the superplastic deformation of the polycrystal.

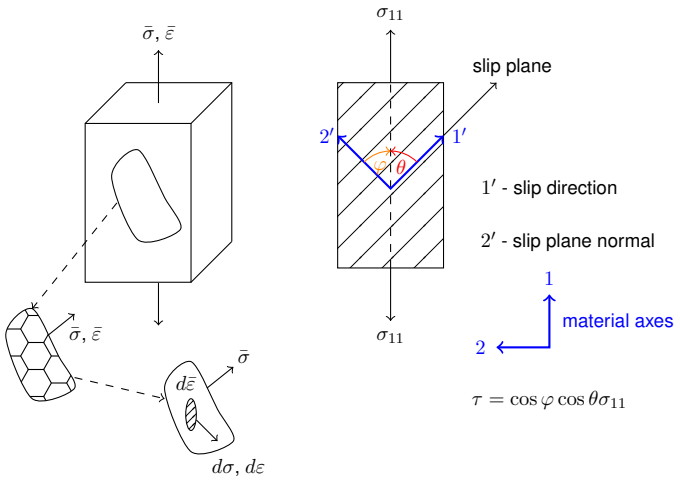

Figure 2.5: A micro-mechanical material model [19]

The concentration of phase B increases with an increase in temperature [19]. If elastic isotropy and spherical inclusions are assumed, the incremental stress of phase A $d\boldsymbol{\sigma}_{\mathrm{A}}$ is given by

$$d\boldsymbol{\sigma}_{\mathrm{A}} = d\bar{\boldsymbol{\sigma}} - 2\mu_{\mathrm{A}}\left(1-\beta\right)\left(\frac{\mu_{\mathrm{A}}}{\left(\mu_{\mathrm{A}}-\mu\right)\beta+\mu}\right)\left(d\boldsymbol{\varepsilon}_{\mathrm{A}}^{\mathrm{sp}} - d\bar{\boldsymbol{\varepsilon}}^{\mathrm{sp}}\right) \ . \tag{2.15}$$

The incremental stress of phase B $d\boldsymbol{\sigma}_{\mathrm{B}}$ is likewise given by

$$d\boldsymbol{\sigma}_{\mathrm{B}} = d\bar{\boldsymbol{\sigma}} - 2\mu_{\mathrm{B}}\left(1-\beta\right)\left(\frac{\mu_{\mathrm{B}}}{\left(\mu_{\mathrm{B}}-\mu\right)\beta+\mu}\right)\left(d\boldsymbol{\varepsilon}_{\mathrm{B}}^{\mathrm{sp}} - d\bar{\boldsymbol{\varepsilon}}^{\mathrm{sp}}\right) \ , \tag{2.16}$$

where μ, μ_{A} and μ_{B} are the shear moduli of the matrix, phase A, and phase B, respectively. The parameter β is given by

$$\beta = \frac{2\left(4-5\nu\right)}{15\left(1-\nu\right)} \ , \tag{2.17}$$

where ν is Poisson's ratio. Eq. (2.15) and Eq. (2.16) are consistent with Kröner's self-consistent relation.

The inclusion is reintroduced into the matrix and the induced stress increment $d\bar{\boldsymbol{\sigma}}$ is computed as the average of $d\boldsymbol{\sigma}$ across all grain orientations. The grains that are aligned with the applied load have $d\boldsymbol{\varepsilon}^{\mathrm{sp}} > d\bar{\boldsymbol{\varepsilon}}^{\mathrm{sp}}$ and $\beta < 1$, and their stresses are relieved incrementally.

The superplastic strain rate of the inclusion $\dot{\varepsilon}^{\mathrm{sp}}$ is related to the strain rate of the accommodation activity on the inclusion's k slip systems. The superplastic strain rate of the inclusion $\dot{\varepsilon}^{\mathrm{sp}}$ is given by

$$\dot{\varepsilon}_{ij}^{\mathrm{sp}} = \sum_{k}\left(\mu_{ij}^{(k)} - \frac{1}{3}\delta_{ij}\right)\dot{\varepsilon}_{\mathrm{diff.}}^{(k)} + \sum_{k} S_{ij}^{(k)}\,\dot{\varepsilon}_{\mathrm{disloc.}}^{(k)} \ , \tag{2.18}$$

where $\dot{\varepsilon}_{\mathrm{diff.}}^{(k)}$ is the strain rate on the k-th slip system due to diffusion and $\dot{\varepsilon}_{\mathrm{disloc.}}^{(k)}$ is the strain rate on the k-th slip system due to dislocation movement. The strain rate due to diffusion on the k-th slip system $\dot{\varepsilon}_{\mathrm{diff.}}^{(k)}$ is given by

$$\dot{\varepsilon}_{\mathrm{diff.}}^{(k)} = a_1\left(\frac{1}{Td^2}\exp\left(\frac{-q_{\mathrm{L}}}{\mathcal{R}T}\right)\left(\sigma_{\mathrm{N}}^{(k)} - \sigma_{\star}\right) + a_2\frac{1}{Td^3}\exp\left(\frac{-q_{\mathrm{gb}}}{\mathcal{R}T}\right)\left(\sigma_{\mathrm{N}}^{(k)} - \sigma_{\star}\right)\right) \ , \tag{2.19}$$

where T is the absolute temperature, $\mathcal{R}$ is the universal gas constant, $\sigma_{\mathrm{N}}^{(k)}$ is the resolved normal stress on the k-th slip system, $\sigma_{\star}$ is the threshold stress, q_{L} is the activation energy for lattice diffusion, q_{gb} is the activation energy for grain boundary diffusion, and a_1 and a_2 are constants. The strain rate due to dislocation movement $\dot{\varepsilon}_{\mathrm{disloc.}}$ is given by

$$\dot{\varepsilon}_{\mathrm{disloc.}} = A\frac{1}{T}\exp\left(\frac{-q_{\mathrm{L}}}{\mathcal{R}T}\right)\sigma^{a_3} \ , \tag{2.20}$$

where A and a_3 are constants.

Figure 2.5 also illustrates the resolved shear stress on a slip plane of the inclusion in the case of uniaxial loading. The resolved shear stress on the k-th slip plane of the inclusion $\tau^{(k)}$ is

related to the local stress σ_{ij} in the inclusion which is given by

$$\tau^{(k)} = S_{ij}^{(k)} \sigma_{ij} \ , \tag{2.21}$$

where $S_{ij}^{(k)}$ is the Schmid factor tensor of the k-th slip system which is given by

$$S_{ij}^{(k)} = \frac{1}{2} \left(b_i N_j + b_j N_i \right) \ , \tag{2.22}$$

where N_i is the normal of the slip plane.

Micro-mechanical models have more constants to determine than phenomenological material models. Micro-mechanical models also require considerably more effort to implement in a finite element package. An example of how a micro-mechanical material model is implemented as a user material into a finite element package is given by Nedoushan, *et al.* [20].

2.6 CONCLUSION

Some metals have certain microstructural characteristics that, when strained at a certain rate and temperature, enable them to deform superplastically. The low strain rates of superplastic deformation is the reason why superplastic forming is a slow process.

The deformation changes from quasi-stable flow to localised necking when a superplastic tensile specimen is strained too quickly. A material model that can show the onset of necking should be used to minimise the forming time of the superplastic forming process.

There are two types of material models namely phenomenological and micro-mechanical material models. Phenomenological material models are functions that best fit measured data with the fewest number of variables. Phenomenological models are usually fitted to uniaxial tensile test data, and they have to be converted to an equivalent form, with for example the Von Mises yield criterion, in order to use them in multi-axial finite element models. Micro-mechanical models are derived from the first principals of thermodynamics and continuum mechanics. Micro-mechanical models are formulated in three dimensions.

CHAPTER 3

EVALUATION OF MATERIAL MODELS

3.1 INTRODUCTION

The goal of this chapter is to select a material model suitable for the minimisation of the forming time of a superplastic forming process. The material model should be able to show the onset of localised thinning. Only phenomenological models are investigated.

3.2 MATERIAL MODELS

Four material models are investigated in this chapter. The first is a state variable sinh strain rate model, denoted as the SV-sinh model. The SV-sinh model is given by [21, 22]

$$\dot{\varepsilon} = \alpha_2 \sinh\left(\beta_2 \left(\sigma - R - k\right)\right) d^{-\gamma} \ , \tag{3.1}$$

where the evolution of isotropic hardening R is given by [21, 22]

$$\dot{R} = b(Q - R)\dot{\varepsilon} \ , \tag{3.2}$$

and the evolution of grain size d is given by [21]

$$\dot{d} = \alpha_1 d^{-\gamma_0} + \beta_1 \dot{\varepsilon} d^{-\phi} \ . \tag{3.3}$$

Here α_1, α_2, γ, γ_0, ϕ, β_1, β_2, k, b and Q are material parameters.

Lin [21] used the grain size evolution equation Eq. (3.3) in conjunction with a power law strain rate equation, but selected γ_0 and ϕ to be identical when he used Eq. (3.1). Eq. (3.1) with the grain growth model with $\gamma_0 = \phi$ is the second model investigated in this study, and it is denoted as Lin's model.

The third model investigated in this study is the power law model given by Eq. (2.7). The fourth model investigated in this study is a tanh-model given by

$$\log \sigma = c_1 \left(\tanh(c_2(\log \dot{\varepsilon} + c_3)) + c_4\right) + c_5 \log \dot{\varepsilon} \ , \tag{3.4}$$

where c_1 to c_5 are material parameters.

The tanh-model is considered due to its shape being similar to the sigmoid curve given in Figure 2.1. The power law model has a constant strain rate sensitivity, whereas the slope of the tanh-model fits the slope of the sigmoid curve which is given in Figure 2.2.

The SV-sinh model fits strain rate sensitivity-strain data from a strain rate jump test. The strain rate sensitivity calculated from the slope of the sigmoid curve is different from the strain rate sensitivity calculated from a strain rate jump test. The difference is shown in Figure 3.1.

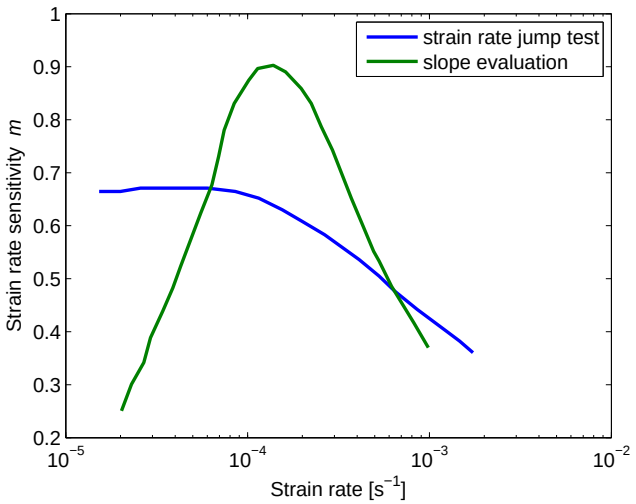

Figure 3.1: Strain rate sensitivity calculated from the slope of the $\log \sigma$-$\log \dot{\varepsilon}$ curve and from a strain rate jump test [23]

3.3 IMPLEMENTATION

The power law model is available in Abaqus, but the tanh-model, Lin's model and the SV-sinh model have to be implemented into Abaqus using a creep subroutine. The implementation of the SV-sinh model is described below. The implementation of Lin's model is similar to the

implementation of the SV-sinh model with the exception that $\gamma_0 = \phi$. The implementation of the tanh-model is given in Appendix A.

The increment in equivalent plastic strain $\Delta\bar{\varepsilon}_\mathrm{p} = \Delta\varepsilon_\mathrm{p}$ and its derivative with respect to Von Mises equivalent flow stress $\frac{d\Delta\bar{\varepsilon}_\mathrm{p}}{d\bar{\sigma}} = \frac{d\Delta\varepsilon_\mathrm{p}}{d\sigma}$ are updated in the creep subroutine. The inputs to the subroutine include the initial conditions to the state variables R and d, the equivalent flow stress $\bar{\sigma} = \sigma$ and the increment in time Δt.

There is viscoplastic flow if $\sigma \geq (k + R)$ in Eq. (3.1), otherwise $\Delta\varepsilon_\mathrm{p}$ and $\frac{d\Delta\varepsilon}{d\sigma}$ are zero, and R and d remain unchanged. The increment in plastic strain $\Delta\varepsilon_\mathrm{p}$ can be calculated with the implicit trapezoidal integration method if there is viscoplastic flow

$$\Delta\varepsilon_\mathrm{p} = \frac{\Delta t}{2}\left(\dot{\varepsilon}_{n+1} + \dot{\varepsilon}_n\right) \ . \tag{3.5}$$

The current strain rate $\dot{\varepsilon}_n$ is given by

$$\dot{\varepsilon}_n = \alpha_2 \sinh\left(\beta_2(\sigma_n - R_n - k)\right) d_n^{-\gamma} \ , \tag{3.6}$$

and the updated strain rate $\dot{\varepsilon}_{n+1}$ is given by

$$\dot{\varepsilon}_{n+1} = \alpha_2 \sinh\left(\beta_2(\sigma_{n+1} - R_{n+1} - k)\right) d_{n+1}^{-\gamma} \ . \tag{3.7}$$

The state variables R_{n+1} and d_{n+1} can be updated using the Newton-Rhapson method

$$\frac{d\mathbf{Res}}{d\boldsymbol{y}}\Delta\boldsymbol{y} = -\mathbf{Res} \ , \tag{3.8}$$

where $\boldsymbol{y}$ contains the state variables

$$\boldsymbol{y} = \begin{Bmatrix} R_{n+1} \\ d_{n+1} \end{Bmatrix} \ , \tag{3.9}$$

$\Delta\boldsymbol{y}$ contains the change in the state variables

$$\Delta\boldsymbol{y} = \begin{Bmatrix} \Delta R \\ \Delta d \end{Bmatrix} \ , \tag{3.10}$$

and $\mathbf{Res}$ contains the residual of the state variables

$$\mathbf{Res} = \begin{Bmatrix} \mathrm{Res}_R \\ \mathrm{Res}_d \end{Bmatrix} \ . \tag{3.11}$$

The implicit trapezoidal method is used again to find the residuals Res_R and Res_d which are given by

$$\text{Res}_R = R_{n+1} - R_n - \frac{\Delta t}{2}\left(\dot{R}_{n+1} + \dot{R}_n\right) \ , \tag{3.12}$$

and

$$\text{Res}_d = d_{n+1} - d_n - \frac{\Delta t}{2}\left(\dot{d}_{n+1} + \dot{d}_n\right) \ , \tag{3.13}$$

respectively. The current rate of isotropic hardening $\dot{R}_n$ is given by

$$\dot{R}_n = b(Q - R_n)\dot{\varepsilon}_n \ , \tag{3.14}$$

and the updated rate of isotropic hardening $\dot{R}_{n+1}$ is given by

$$\dot{R}_{n+1} = b(Q - R_{n+1})\dot{\varepsilon}_{n+1} \ . \tag{3.15}$$

The current rate of grain growth $\dot{d}_n$ is given by

$$\dot{d}_n = \alpha_1 d_n^{-\gamma_0} + \beta_1 d_n^{-\phi}\dot{\varepsilon}_n \ , \tag{3.16}$$

and the updated rate of grain growth $\dot{d}_{n+1}$ is given by

$$\dot{d}_{n+1} = \alpha_1 d_{n+1}^{-\gamma_0} + \beta_1 d_{n+1}^{-\phi}\dot{\varepsilon}_{n+1} \ . \tag{3.17}$$

The derivative of the residual of the state variables with respect to the state variables $\frac{d\mathbf{Res}}{d\boldsymbol{y}}$ (the system Jacobian) is given by

$$\frac{d\mathbf{Res}}{d\boldsymbol{y}} = \begin{bmatrix} \frac{\partial \text{Res}_R}{\partial R_{n+1}} & \frac{\partial \text{Res}_R}{\partial d_{n+1}} \\ \frac{\partial \text{Res}_d}{\partial R_{n+1}} & \frac{\partial \text{Res}_d}{\partial d_{n+1}} \end{bmatrix} \ . \tag{3.18}$$

The individual entries of the system Jacobian are given by

$$\begin{aligned} \frac{\partial \text{Res}_R}{\partial R_{n+1}} = 1 - \frac{\alpha_2 b \Delta t}{2 d_{n+1}^{\gamma}} &\left(\sinh\left(\beta_2(R_{n+1} + k - \sigma_{n+1})\right)\right. \\ &\left. -\beta_2 \cosh\left(\beta_2(R_{n+1} + k - \sigma_{n+1})\right)(Q - R_{n+1})\right) \ , \end{aligned} \tag{3.19}$$

$$\frac{\partial \text{Res}_R}{\partial d_{n+1}} = -\frac{\alpha_2 b \Delta t \gamma \sinh\left(\beta_2(R_{n+1} + k - \sigma_{n+1})\right)(Q - R_{n+1})}{2 d_{n+1}^{\gamma+1}} \ , \tag{3.20}$$

$$\frac{\partial \text{Res}_d}{\partial R_{n+1}} = \frac{\alpha_2 \beta_1 \beta_2 \Delta t \cosh\left(\beta_2(R_{n+1} + k - \sigma_{n+1})\right)}{2 d_{n+1}^{\gamma} d_{n+1}^{\phi}} \ , \tag{3.21}$$

$$\begin{aligned} \frac{\partial \text{Res}_d}{\partial d_{n+1}} = 1 - \frac{\Delta t}{2} &\left(\frac{\alpha_2 \beta_1 \gamma \sinh\left(\beta_2(R_{n+1} + k - \sigma_{n+1})\right)}{d_{n+1}^{\phi} d_{n+1}^{\gamma+1}}\right. \\ &\left. -\frac{\alpha_1 \gamma_0}{d_{n+1}^{\gamma_0+1}} + \frac{\alpha_2 \beta_1 \phi \sinh\left(\beta_2(R_{n+1} + k - \sigma_{n+1})\right)}{d_{n+1}^{\gamma} d_{n+1}^{\phi+1}}\right) \ . \end{aligned} \tag{3.22}$$

$$\tag{3.23}$$

The derivative of the increment in strain with respect to flow stress $\frac{d\Delta\varepsilon}{d\sigma_{n+1}}$ can be found using the chain rule of differentiation

$$\frac{d\Delta\varepsilon}{d\sigma_{n+1}} = \frac{\partial\Delta\varepsilon}{\partial\sigma_{n+1}} + \frac{\partial\Delta\varepsilon}{\partial R_{n+1}}\frac{dR_{n+1}}{d\sigma_{n+1}} + \frac{\partial\Delta\varepsilon}{\partial d_{n+1}}\frac{dd_{n+1}}{d\sigma_{n+1}} , \tag{3.24}$$

where $\frac{\partial\Delta\varepsilon}{\partial\sigma_{n+1}}$ is given by

$$\frac{\partial\Delta\varepsilon}{\partial\sigma_{n+1}} = \frac{\alpha_2\beta_2\Delta t\cosh\left(\beta_2(R_{n+1}+k-\sigma_{n+1})\right)}{2d_{n+1}^{\gamma}} , \tag{3.25}$$

$\frac{\partial\Delta\varepsilon}{\partial R_{n+1}}$ is given by

$$\frac{\partial\Delta\varepsilon}{\partial R_{n+1}} = -\frac{\alpha_2\beta_2\Delta t\cosh\left(\beta_2(R_{n+1}+k-\sigma_{n+1})\right)}{2d_{n+1}^{\gamma}} , \tag{3.26}$$

and $\frac{\partial\Delta\varepsilon}{\partial d_{n+1}}$ is given by

$$\frac{\partial\Delta\varepsilon}{\partial d_{n+1}} = \frac{\alpha_2\gamma\Delta t\sinh\left(\beta_2(R_{n+1}+k-\sigma_{n+1})\right)}{2d_{n+1}^{\gamma+1}} . \tag{3.27}$$

$\frac{dR_{n+1}}{d\sigma_{n+1}}$ and $\frac{dd_{n+1}}{d\sigma_{n+1}}$ can be calculated using the Newton-Rhapson method

$$\frac{d\mathbf{Res}}{d\boldsymbol{y}}\frac{d\boldsymbol{y}}{d\sigma} = -\frac{\partial\mathbf{Res}}{\partial\sigma} , \tag{3.28}$$

where $\frac{d\boldsymbol{y}}{d\sigma}$ contains the derivatives of the state variables with respect to flow stress

$$\frac{d\boldsymbol{y}}{d\sigma} = \begin{Bmatrix} \frac{dR_{n+1}}{d\sigma} \\ \frac{dd_{n+1}}{d\sigma} \end{Bmatrix} , \tag{3.29}$$

and $\frac{d\mathbf{Res}}{d\sigma}$ contains the derivatives of the residual of the state variables with respect to flow stress

$$\frac{\partial\mathbf{Res}}{\partial\sigma} = \begin{Bmatrix} \frac{\partial\mathrm{Res}_R}{\partial\sigma} \\ \frac{\partial\mathrm{Res}_d}{\partial\sigma} \end{Bmatrix} . \tag{3.30}$$

The derivative $\frac{\partial\mathrm{Res}_R}{\partial\sigma}$ is given by

$$\frac{\partial\mathrm{Res}_R}{\partial\sigma} = -\frac{\alpha_2 b\beta_2\Delta t\cosh\left(\beta_2(R_{n+1}+k-\sigma)\right)(Q-R_{n+1})}{2d_{n+1}^{\gamma}} . \tag{3.31}$$

The derivative $\frac{\partial\mathrm{Res}_d}{\partial\sigma}$ is given by

$$\frac{\partial\mathrm{Res}_d}{\partial\sigma} = -\frac{\alpha_2\beta_1\beta_2\Delta t\cosh\left(\beta_2(R_{n+1}+k-\sigma_{n+1})\right)}{2d_{n+1}^{\gamma}d_{n+1}^{\phi}} . \tag{3.32}$$

The subroutine of the SV-sinh model consists of Eq. (3.5) to Eq. (3.32). The subroutine that is implemented into Abaqus is given in Appendix A.

The subroutine can be tested as a standalone routine by also computing the equivalent stress increment $\Delta\sigma$ using the Newton-Rhapson method

$$\frac{d\Delta\varepsilon}{d\sigma}\Delta\sigma = -\text{Res}_\sigma \ , \tag{3.33}$$

where $\frac{d\Delta\varepsilon}{d\sigma}$ is the derivative of the equivalent strain increment with respect to Von Mises equivalent flow stress. The residual of stress Res_σ is given by

$$\text{Res}_\sigma = \Delta\varepsilon - \Delta\varepsilon_{\text{target}} \ , \tag{3.34}$$

where $\Delta\varepsilon$ is the strain increment and $\Delta\varepsilon_{\text{target}}$ is the target strain increment. The strain increment $\Delta\varepsilon$ is the sum of its elastic $\Delta\varepsilon_{\text{e}}$ and plastic $\Delta\varepsilon_{\text{p}}$ components, where the increment in elastic strain $\Delta\varepsilon_{\text{e}}$ is given by

$$\Delta\varepsilon_{\text{e}} = \frac{\Delta\sigma}{E} \ , \tag{3.35}$$

where E is Young's modulus. The plastic component is calculated in the subroutine. The target strain increment $\Delta\varepsilon_{\text{target}}$ is given by

$$\Delta\varepsilon_{\text{target}} = \Delta t\dot{\varepsilon}_{\text{target}} \ , \tag{3.36}$$

where $\dot{\varepsilon}_{\text{target}}$ is the target strain rate and Δt is the time increment.

3.4 CALIBRATION

The material parameters are found by calibrating the material models for a specific superplastic metal. The data, digitised from the experimental work by Gosh and Hamilton [4], is used to calibrate the material models. The data is for Ti-6Al-4V with three different initial grain sizes that were strained at different strain rates at a temperature of 927°C.

Lin [21] calibrated his material models using only stress-strain and grain size-time data. The SV-sinh model is also calibrated with strain rate sensitivity-strain data in this study, because accurate strain rate sensitivity is critical to predict localised thinning at higher strain rates [3, 4, 23]. Gosh and Hamilton [4] found the strain rate sensitivity-strain data using strain rate jump tests. The strain rate sensitivity found with a strain rate jump test has been found to be more accurate than evaluating the slope of the $\log\sigma$-$\log\dot{\varepsilon}$ curve [24].

The tanh-model and the power law model are fitted to strain rate sensitivity-strain rate data calculated from stress-strain rate data from Gosh and Hamilton [15] for Ti-6Al-4V with an initial grain size of 6.4 µm.

The calibration of a material model can be treated as a nonlinear, unconstrained, continuous, multi-variate, multi-objective optimisation problem. Background on these types of optimisation problems are given in the following section.

3.4.1 Background

3.4.1.1 Multi-objective optimisation

A general, nonlinear, constrained, single objective optimisation problem can be described as follows:

$$\begin{gathered} \text{Minimise } f(\boldsymbol{x}) \\ \text{subject to} \\ \boldsymbol{h}(\boldsymbol{x}) = \mathbf{0} \\ \boldsymbol{g}(\boldsymbol{x}) \leq \mathbf{0} \\ \mathbf{lb} \leq \boldsymbol{x} \leq \mathbf{ub} \end{gathered}$$

Here $\boldsymbol{h}(\boldsymbol{x}) = \{h_1(\boldsymbol{x}), h_2(\boldsymbol{x}), \ldots, h_i(\boldsymbol{x})\}$ are the equality constraints, and $\boldsymbol{g}(\boldsymbol{x}) = \{g_1(\boldsymbol{x}), g_2(\boldsymbol{x}), \ldots, g_j(\boldsymbol{x})\}$ are the inequality constraints. The lower and upper bounds of the boundary constraints are given by **lb** and **ub**, respectively. The design vector is given by $\boldsymbol{x}$, and the objective function is $f(\boldsymbol{x})$.

A single objective optimisation problem can have global and local minima. An objective function $f(\boldsymbol{x})$ has a global minimum at $\boldsymbol{x}^*$ if

$$f(\boldsymbol{x}^*) \leq f(\boldsymbol{x}) \ , \tag{3.37}$$

in the feasible set $\mathcal{S}$. A strict inequality means that $\boldsymbol{x}^*$ is a strong global minimum, otherwise $\boldsymbol{x}^*$ is a weak global minimum [25]. An objective function $f(\boldsymbol{x})$ likewise has a local minimum at $\boldsymbol{x}^*$ if condition (3.37) is satisfied in a small neighbourhood $\mathcal{N}$ of $\boldsymbol{x}^*$ in the feasible set $\mathcal{S}$. $\mathcal{N}$ is given by

$$\mathcal{N} = \{\boldsymbol{x} | \boldsymbol{x} \in \mathcal{S} \text{ with } \|\boldsymbol{x} - \boldsymbol{x}^*\| < \delta\} \ , \tag{3.38}$$

where δ is a small positive number value. The different minima are shown in Figure 3.2.

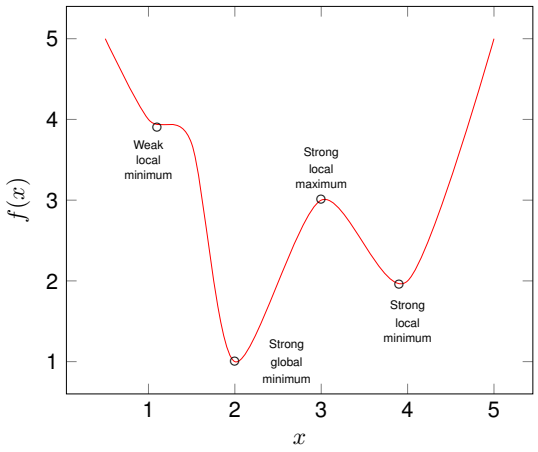

Figure 3.2: Different types of minima

The definition of optimality for multi-objective optimisation problems is not as simple as condition (3.37). The goal of multi-objective optimisation problems is to balance the objective functions such that the solution cannot improve one objective without degrading another objective. Such a solution is called a Pareto optimal solution [25, 26, 27]. There are multiple Pareto optimal solutions for a multi-objective optimisation problem.

There are two types of methods that can be used to find Pareto optimal solutions for multi-objective optimisation problems. They are scalarisation methods and vector methods [25]. Objective functions are combined to form a scalar objective function with scalarisation methods, whereas each objective function is treated separately with vector methods. Well-known single objective optimisation algorithms can be used to minimise scalarised multi-objective optimisation problems.

A popular scalarisation method is to minimise the weighted sum of the objective functions U, which is given by

$$U = \sum_{i=1}^{k} w_i f_i(\boldsymbol{x}) \ , \tag{3.39}$$

where $f_i(\boldsymbol{x})$ is the i-th objective function and w_i is the i-th weight. The weights indicate the importance of each objective function. A different Pareto optimal solution is obtained each time the weights are changed.

The weighted sum method is easy to implement. This method will always yield a minimum

that is Pareto optimal if all of the weights are positive [25]. There are however some disadvantages to the weighted sum method. An *a priori* selection of weights will not necessarily result in an acceptable final solution. A consistent and continuous variation of weights may not result in a similarly consistent and continuous distribution of Pareto optimal points nor lead to yielding the entire Pareto optimal set.

An example of a vector method for solving multi-objective optimisation problems is the lexicographic method [25]. The objective functions are ordered according to significance and each objective function $f_i(\boldsymbol{x})$ is minimised subject to the condition given by

$$f_j(\boldsymbol{x}) \leq f_j(\boldsymbol{x}_j^*) \ , \tag{3.40}$$

where i is the position of the function, which is greater than one, and $j = 1$ to $(i-1)$. $f_j(\boldsymbol{x}_j^*)$ is the minimum of the j-th objective function for the j-th optimisation problem. This method is usually terminated once two consecutive optimisation problems yield the same minimum.

The lexicographic method has the advantage that it always yields a Pareto optimal solution if a global optimisation algorithm is used. The disadvantages of the lexicographic method is that many single objective optimisation problems have to be solved in order to find a solution [25].

3.4.1.2 Optimisation algorithms

There are two types of methods that can be used to find the minimum of an optimisation problem, namely:

1. Optimality criteria methods

2. Search methods

Optimality criteria methods require that the objective function satisfy certain conditions at its minimum. Search methods start off with an estimate of the minimum, which usually does not satisfy optimality criteria, and is improved iteratively until the final improvement satisfies optimality criteria [25]. Optimality criteria can either be used to find a local minimum or to check if a point is a local minimum. Optimality criteria are the necessary and sufficient

conditions that a point $\boldsymbol{x}$ must satisfy in order to qualify as a minimum.

The first order necessary condition for the objective function $f(\boldsymbol{x})$ of an unconstrained optimisation problem to have a local minimum at $\boldsymbol{x}^*$ is given by

$$\frac{\partial f(\boldsymbol{x}^*)}{\partial x_i} = 0, \quad i = 1, 2, \ldots, n \tag{3.41}$$

where n is the length of $\boldsymbol{x}$ [25, 26]. The second order necessary condition requires that the Hessian matrix $\boldsymbol{H}(\boldsymbol{x}^*)$, which is given by

$$\boldsymbol{H}(\boldsymbol{x}^*) = \left[\frac{\partial^2 f}{\partial x_i \partial x_j}\right]_{n \times n} , \tag{3.42}$$

is positive semi-definite or positive definite at $\boldsymbol{x}^*$. If the Hessian matrix is positive definite, it satisfies the second order sufficiency condition and $\boldsymbol{x}^*$ is a local minimum. These conditions are subject to the assumption that the design variables and functions are continuous and at least twice continuously differentiable.

Search methods such as classic iterative optimisation algorithms or direct search methods, and adaptive or indirect search methods have been used to calibrate material models [16, 26, 28]. Iterative optimisation algorithms include the conjugate gradient method, quasi-Newton methods and sequential quadratic programming [28]. Adaptive search methods include neural networks and genetic algorithms.

The general iterative process of a classic iterative optimisation algorithm can be described with

$$\boldsymbol{x}^{k+1} = \boldsymbol{x}^k + \Delta \boldsymbol{x}^k , \tag{3.43}$$

where $\boldsymbol{x}^k$ is the design vector of the k-th iteration and $\Delta \boldsymbol{x}^k$ is the change in the design of the k-th iteration which is given by

$$\Delta \boldsymbol{x}^k = a_k \boldsymbol{d}^k , \tag{3.44}$$

where $\boldsymbol{d}^k$ is the search direction and a_k is the step size [25]. From Eq. (3.43) it can be observed that a starting point $\boldsymbol{x}_0$ is required for the iterative process. An algorithm is robust if it is able to converge to a local minimum from an arbitrary starting point that is in the feasible or infeasible set.

If $\boldsymbol{x}^k$ is not a minimum of $f(\boldsymbol{x})$, in other words the optimality criteria described above are not satisfied at $\boldsymbol{x}^k$, then there may be a point $\boldsymbol{x}^{k+1}$ with a smaller function value than $\boldsymbol{x}^k$ which is given by

$$f(\boldsymbol{x}^{k+1}) < f(\boldsymbol{x}^k) \ . \tag{3.45}$$

If Eq. (3.43) is substituted into condition (3.45), then

$$f(\boldsymbol{x}^k + a_k \boldsymbol{d}^k) < f(\boldsymbol{x}^k) \ . \tag{3.46}$$

If the left side of condition (3.46) is approximated with a linear Taylor series expansion, then

$$\nabla f(\boldsymbol{x}^k) \cdot \boldsymbol{d}^k < 0 \ , \tag{3.47}$$

where $\nabla f(\boldsymbol{x}^k)$ is the gradient of $f(\boldsymbol{x})$. The search direction $\boldsymbol{d}^k$ can be calculated with a method such as the steepest descent method where the descent condition (3.47) is satisfied with $\boldsymbol{d}^k = -\nabla f(\boldsymbol{x}^k)$ [25]. The way the search direction is calculated distinguishes the different direct search methods.

A small move along the search direction $\boldsymbol{d}^k$ reduces the cost function $f(\boldsymbol{x})$. Once the search direction is known, the step size a_k can be computed by minimising the line search function $f(a_k)$. Analytically this can be done by satisfying optimality criteria. The necessary condition, which is given by

$$\frac{df(\boldsymbol{x}^{k+1})}{da_k} = \frac{\partial f^{\intercal}(\boldsymbol{x}^{k+1})}{\partial \boldsymbol{x}} \frac{d(\boldsymbol{x}^{k+1})}{da_k} = \nabla f(\boldsymbol{x}^{k+1}) \cdot \boldsymbol{d}^k = 0 \ , \tag{3.48}$$

reveals that $\nabla f(\boldsymbol{x}^{k+1})$ is orthogonal to the search direction $\boldsymbol{d}^k$. The smallest root of Eq. (3.48) is a_k. Eq. (3.48) can also be used as the termination criterion in numerical procedures that are used to find a_k. It may not however be possible to obtain an explicit line function $f(a_k)$. A numerical method such as the golden section search method can be used to find a_k in such cases [25].

There may be also be cases where the calculation of the gradient of the cost function $\nabla f(\boldsymbol{x})$ is too expensive. A direct search method that does not make use of gradient information is the Nelder-Mead simplex method. This search method is available in Matlab as *fminsearch*, and the algorithm is discussed by Lagarias, *et al.* [29].

Iterative optimisation algorithms may get stuck in local minima and the global minimum will not be found if the optimisation problem is multi-modal. This happens when the starting point is far from the global minimum. The starting point is almost never known *a priori*. An iterative optimisation algorithm can be started multiple times at different random points in the design space in order to find the global minimum [28, 30]. This technique requires many function evaluations, but iterative search methods have been found to converge to a local minimum in relatively few iterations for low dimensional problems [31].

Adaptive search methods do not require a starting point, and they tend to converge to a global minimum [26, 28]. There is however no guarantee that the adaptive search method has converged to the global minimum [25]. Adaptive search methods are suitable for non-smooth and highly nonlinear functions, and very large optimisation problems.

An example of an adaptive search method is a genetic algorithm. Genetic algorithms use random numbers, and information from previous iterations to a evaluate and improve a group of promising solutions rather than a single solution. The general steps of a genetic algorithm are described by Arora [25] and Bonte [28].

Genetic algorithms have the disadvantage that they require many function evaluations even for reasonably sized optimisation problems. Genetic algorithms are also not as widely known as classic iterative search methods. Genetic algorithms have however been used to calibrate material models for superplastic forming [16, 26].

3.4.2 Method of calibration of the SV-sinh model

The objective function for the calibration of the SV-sinh model is given by

$$f(\boldsymbol{x}) = e_{\mathrm{T}} = w_\sigma e_\sigma + w_m e_m + w_d e_d \ , \tag{3.49}$$

where e_{T} is the total error, e_σ is the stress error, e_m is the strain rate sensitivity error and e_d is the grain size error. The stress error weight is given by w_σ, the strain rate sensitivity error weight is given by w_m, and w_d is the grain size error weight. The material parameters $\boldsymbol{x}$ are given by

$$\boldsymbol{x} = \left\{ \gamma \quad \beta_2 \quad k \quad \alpha_2 \quad b \quad Q \quad \alpha_1 \quad \beta_1 \quad \gamma_0 \quad \phi \right\} \ . \tag{3.50}$$

The stress error e_σ is given by

$$e_\sigma = \sqrt{\sum_{i=1}^{k} \left(\sigma_i - \sigma_i^{\text{data}}\right)^2} \ . \tag{3.51}$$

The superplastic stress-strain data is given at a specific strain rate. The equivalent stress increment $\Delta\sigma$ at a specific strain rate can be calculated using Eq. (3.33).

The strain rate sensitivity error e_m is similarly given by

$$e_m = \sqrt{\sum_{i=1}^{k} \left(m_i - m_i^{\text{data}}\right)^2} \ . \tag{3.52}$$

The strain rate jump test is replicated numerically in order to calculate the strain rate sensitivities at the same points as the data points. The strain rate is kept constant at $\dot{\varepsilon}$ s^{-1}. The strain rate is then increased to $1.25\dot{\varepsilon}$ s^{-1} and held there for approximately 2 to 3% plastic strain. The strain rate is then stepped down to $\dot{\varepsilon}$. The stress just before the strain rate decrease from $1.25\dot{\varepsilon}$ s^{-1} to $\dot{\varepsilon}$ s^{-1} is given by σ_2. The stress at $\dot{\varepsilon}$ s^{-1} at the corresponding total strain is given by σ_1. The strain rate sensitivity m is therefore given by

$$m = \frac{\log\left(\sigma_2/\sigma_1\right)}{\log(1.25)} \ . \tag{3.53}$$

More detail on strain rate jump tests is given by Hedworth and Stowell [14] and ASTM standard E2448-112011 [32]. An example of a numerical strain rate jump test is given in Figure 3.3. The red and blue crosses indicate σ_1 and σ_2, respectively.

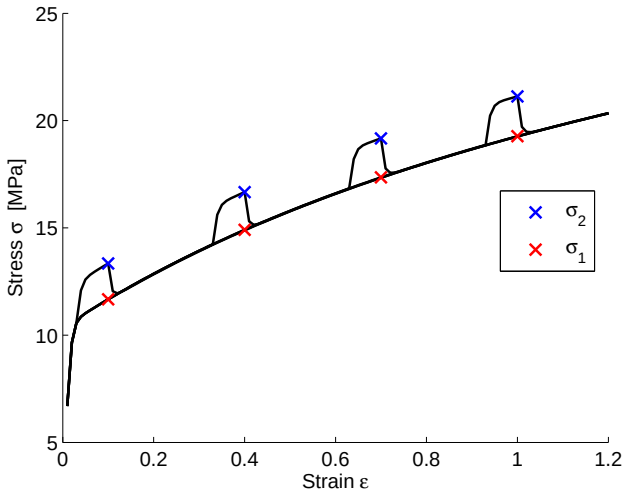

Figure 3.3: Numerical strain rate jump test

The grain size error e_d is given by

$$e_d = \sqrt{\sum_{i=1}^{k} \left(d_i - d_i^{\text{data}}\right)^2} \ . \tag{3.54}$$

The grain size error e_d has static $e_{d_{\text{static}}}$ and dynamic $e_{d_{\text{dynam.}}}$ components. The dynamic grain size $d_{\text{dynam.}}$ is calculated in the subroutine. The static grain size d_{static} is given by

$$d_{\text{static}} = \left(d_0^{\gamma_0+1} + (\gamma_0+1)\alpha_1 t\right)^{1/(\gamma_0+1)} \ , \tag{3.55}$$

if $\dot{\varepsilon} = 0$ is substituted into Eq. (3.3). The initial grain size is given by d_0.

The total error e_{T} is minimised using the Nelder-Mead simplex method. The Nelder-Mead simplex method requires a starting point. The starting point is given by [26, 33]

$$\begin{aligned} \boldsymbol{x}_0 &= \left\{\gamma \quad \beta_2 \quad k \quad \alpha_2 \quad b \quad Q \quad \alpha_1 \quad \beta_1 \quad \gamma_0 \quad \phi\right\} \\ &= \left\{1.408 \quad 0.035 \quad 0.242 \quad 0.042 \quad 2.854 \quad 3.933 \quad 73.408 \quad 2.188 \quad 5.751 \quad 0.141\right\} \ . \end{aligned} \tag{3.56}$$

3.4.3 Results of the calibration of the SV-sinh model

3.4.3.1 Effect of error weights

The errors e_σ, e_m and e_d are each calibrated individually in order to see what the smallest error is for each part of the objective function $f(\boldsymbol{x}) = e_{\text{T}}$. The influence of each error is used to determine an appropriate choice of error weights. The weights $\boldsymbol{w} = \{\, w_\sigma \ w_m \ w_d \,\}$, optimised material parameters $\boldsymbol{x}_{\text{opt}}$ and final errors $\boldsymbol{e} = \{\, e_\sigma \ e_m \ e_d \,\}$ for this investigation are given in Table 3.1.

The constants of Eq. (3.2) and Eq. (3.3) do no affect the grain size evolution and can therefore not be estimated for the $\boldsymbol{w} = \{\, 0\ 0\ 1 \,\}$ case. The material parameters of Eq. (3.3) may however have been misused to improve the fit of the stress-strain and strain rate sensitivity-strain experimental data for the $\boldsymbol{w} = \{\, 1\ 0\ 0 \,\}$ and $\boldsymbol{w} = \{\, 0\ 1\ 0 \,\}$ cases.

Table 3.1: Optimised material parameters and final errors of the individual optimisation of e_σ, e_m and e_d

$\boldsymbol{w}$	$\boldsymbol{x}_{\text{opt}}$	$\boldsymbol{e}$
1 0 0	2.3098 0.10792 $1.6474e{-12}$ 0.055116 11.325 1.1328 0.015947 3.5595 1.4241 0.13712	58.809 0.075357 1404.4
0 1 0	3.94 0.095286 0.3936 1.3312 0.0010763 877.52 26 029 2.0574 9.833 $2.2217e{-15}$	12 132 0.0098247 272.7
0 0 1	N/A N/A N/A N/A N/A N/A 7.9798 163.74 4.8108 $1.0543e{-20}$	N/A N/A 5.8768

The stress-strain experimental and model data for the $\boldsymbol{w} = \{1\,0\,0\}$ and $\boldsymbol{w} = \{0\,1\,0\}$ cases are compared in Figure 3.4. The stress error for the $\boldsymbol{w} = \{0\,1\,0\}$ case is 205 times larger than the stress error for the $\boldsymbol{w} = \{1\,0\,0\}$ case. The stress-strain model data with an initial grain size of 9 µm strained a strain rate of 10^{-3} s^{-1} is swapped with stress-strain model data with an initial grain size of 11.5 µm strained a strain rate of 2×10^{-4} s^{-1} for the $\boldsymbol{w} = \{0\,1\,0\}$ case. This may be due to a lack of strain rate sensitivity-strain experimental data for these initial grain sizes and strain rates.

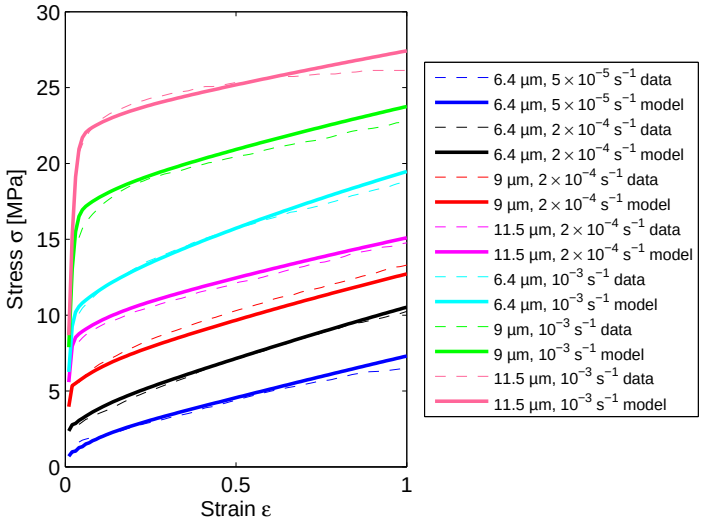

(a)

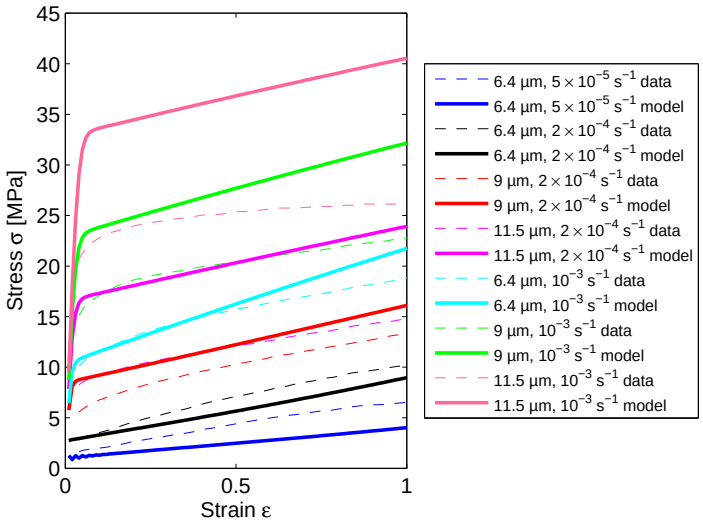

(b)

Figure 3.4: Stress-strain experimental and model data for the (a) $\boldsymbol{w} = \{1\,0\,0\}$ and (b) $\boldsymbol{w} = \{0\,1\,0\}$ cases

The strain rate sensitivity-strain experimental and model data for the $\boldsymbol{w} = \{1\,0\,0\}$ and $\boldsymbol{w} = \{0\,1\,0\}$ cases are compared in Figure 3.5. The strain rate sensitivity error for the $\boldsymbol{w} = \{0\,1\,0\}$ case is 87% smaller than the strain rate sensitivity error for the $\boldsymbol{w} = \{1\,0\,0\}$ case.

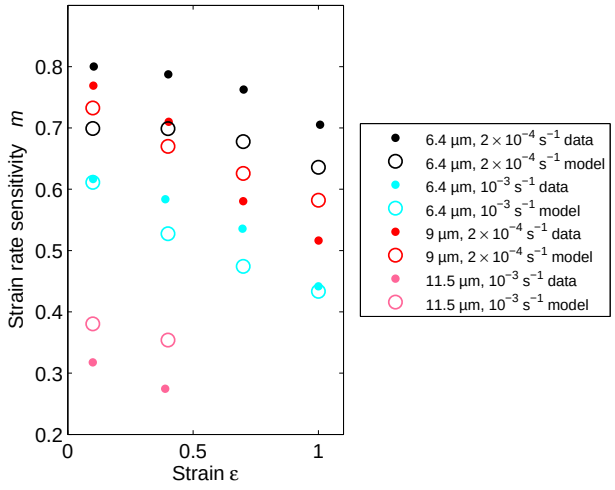

(a)

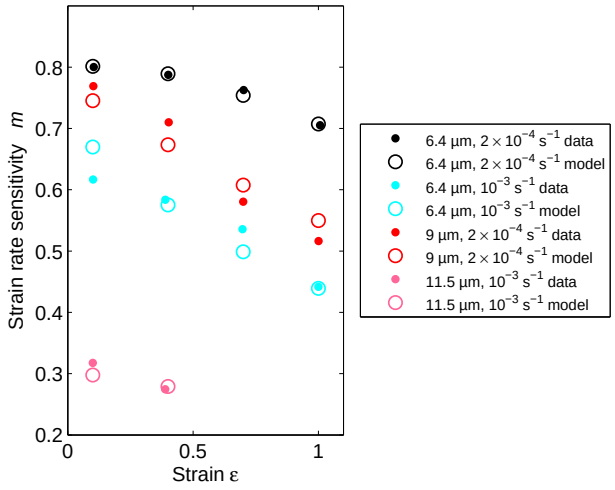

(b)

Figure 3.5: Strain rate sensitivity-strain experimental and model data for the (a) $\boldsymbol{w} = \{1\,0\,0\}$ and (b) $\boldsymbol{w} = \{0\,1\,0\}$ cases

The grain size-time experimental and model data for the three different cases of $\boldsymbol{w}$ with initial grain sizes 6.4 μm, 9 μm and 11.5 μm are compared in Figures 3.6, 3.7 and 3.8, respectively. The static grain size-time experimental data is not captured for the $\boldsymbol{w} = \{1\,0\,0\}$ and $\boldsymbol{w} = \{0\,1\,0\}$ cases.

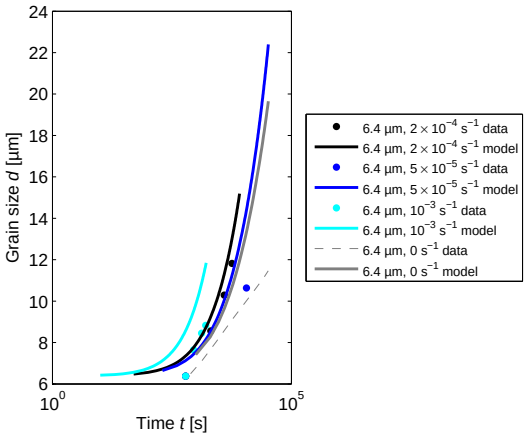

(a)

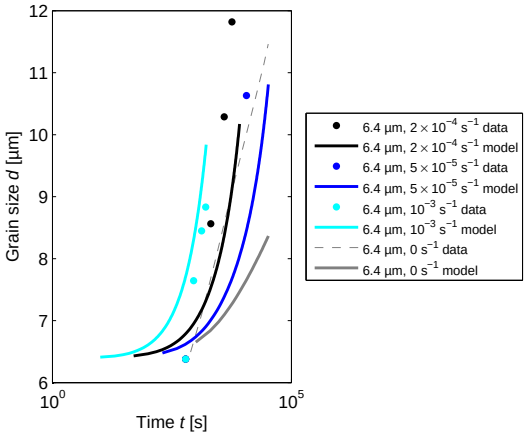

(b)

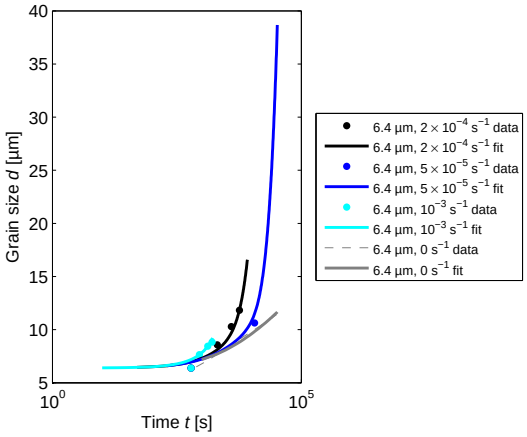

(c)

Figure 3.6: Grain size-time experimental and model data with an initial grain size of 6.4 µm for the (a) $\boldsymbol{w} = \{1\ 0\ 0\}$, (b) $\boldsymbol{w} = \{0\ 1\ 0\}$ and (c) $\boldsymbol{w} = \{0\ 0\ 1\}$ cases

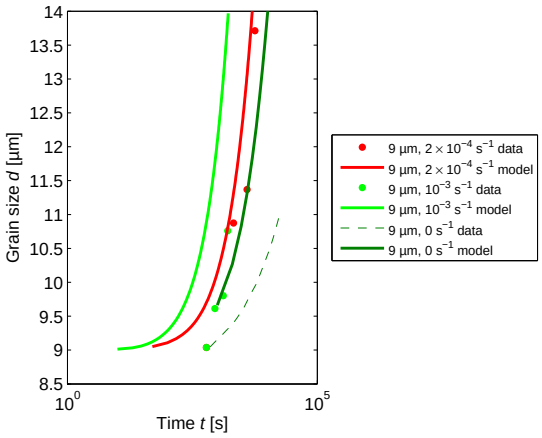

(a)

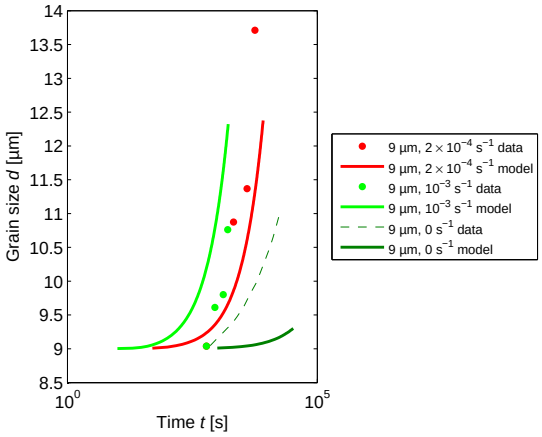

(b)

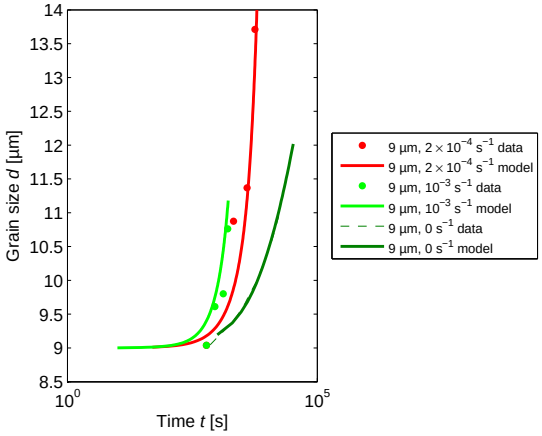

(c)

Figure 3.7: Grain size-time experimental and model data with an initial grain size of 9 µm for the (a) $\boldsymbol{w} = \{1\ 0\ 0\}$, (b) $\boldsymbol{w} = \{0\ 1\ 0\}$ and (c) $\boldsymbol{w} = \{0\ 0\ 1\}$ cases

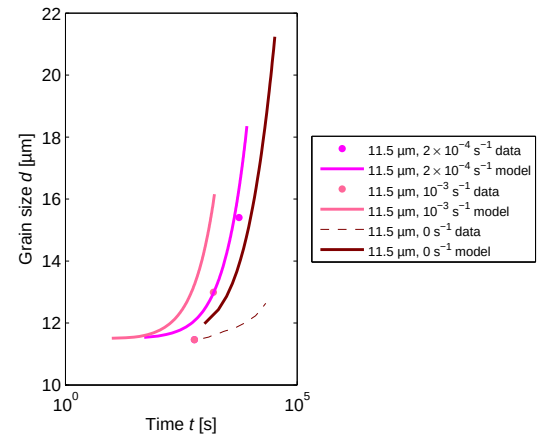

(a)

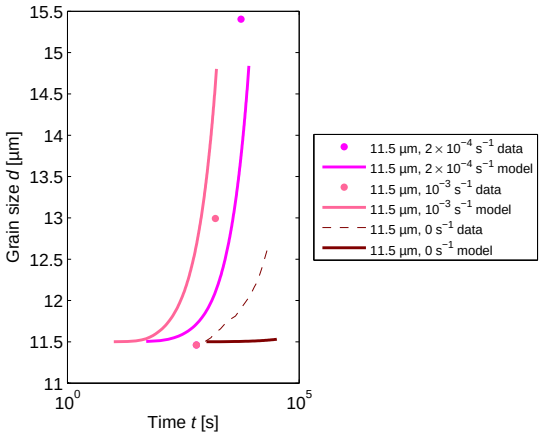

(b)

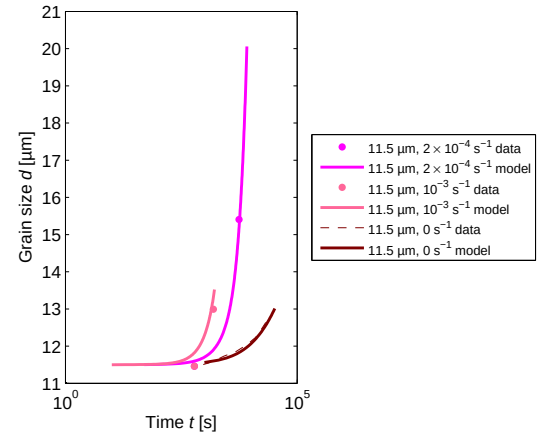

(c)

Figure 3.8: Grain size-time experimental and model data with an initial grain size of 11.5 µm for the (a) $\boldsymbol{w} = \{1\ 0\ 0\}$, (b) $\boldsymbol{w} = \{0\ 1\ 0\}$ and (c) $\boldsymbol{w} = \{0\ 0\ 1\}$ cases

Three sets of error weights are investigated, as summarised in Table 3.2. The first set of weights $\boldsymbol{w} = \{1\ 1\ 1\}$ results in errors $\boldsymbol{e} = \{82.185\ 0.17902\ 27.988\}$. This choice of weights therefore prioritises the stress error. The second set prioritises the strain rate sensitivity-strain data. Set 3 aims to balance the fit of the stress-strain and strain rate sensitivity-strain experimental data. The optimised constants $\boldsymbol{x}_{\text{opt}}$ and final errors $\boldsymbol{e}$ are also given in Table 3.2.

Table 3.2: Optimised material parameters and final errors for the different sets of weights investigated

Set	$\boldsymbol{w}$	$\boldsymbol{x}_{\text{opt}}$	$\boldsymbol{e}$
1	1 1 1	2.3079 0.11325 $1.3318e{-17}$ 0.04818 1.5114 5.2662 0.85654 1.8277 3.7841 0.12167	82.185 0.17902 27.988
2	0.5 12 000 5.4	2.9162 0.11952 $2.64e{-17}$ 0.14636 0.32491 3.8655 8.9568 1.8241 4.8116 $6.4877e{-08}$	524.77 0.030841 29.297
3	2 3 000 5.4	2.4253 0.11532 $1.5603e{-15}$ 0.057089 1.033 4.5091 9.0249 1.7347 4.8029 $6.9144e{-20}$	125.1440 0.0930 28.8268

The stress-strain experimental and model data for set 1, 2 and 3 are compared in Figure 3.9. The stress error of set 1 is 84% smaller than the stress error of set 2. The stress error of set 1 is 34% smaller than the stress error of set 3.

The strain rate sensitivity-strain experimental and model data for set 1, 2 and 3 are compared in Figure 3.10. The strain rate sensitivity-strain model data with an initial grain size of 6.4 µm strained at 2×10^{-4} s^{-1} and the strain rate sensitivity-strain model data with an initial grain size of 9 µm strained at 2×10^{-4} s^{-1} lie almost on top of each other for set 1 and 3. The strain rate sensitivity error of set 2 is 83% smaller than the strain rate sensitivity error of set 1. The strain rate sensitivity error of set 2 is 67% smaller than the strain rate sensitivity

error of set 3.

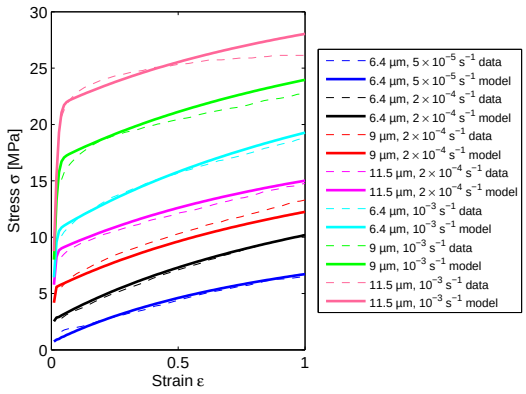

(a)

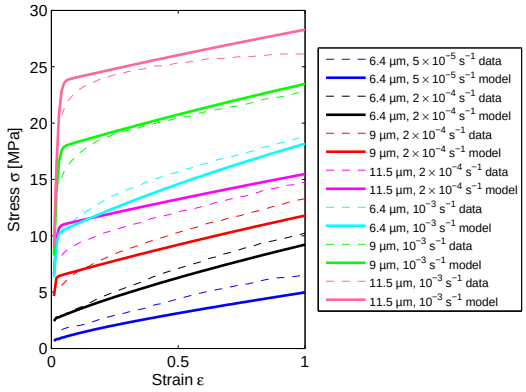

(b)

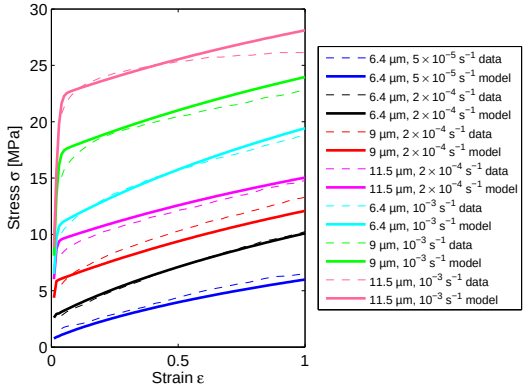

(c)

Figure 3.9: Stress-strain experimental and model data for (a) set 1, (b) 2 and (c) 3 of the SV-sinh model

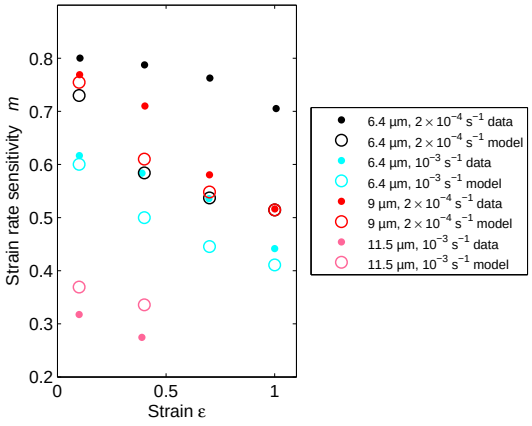

(a)

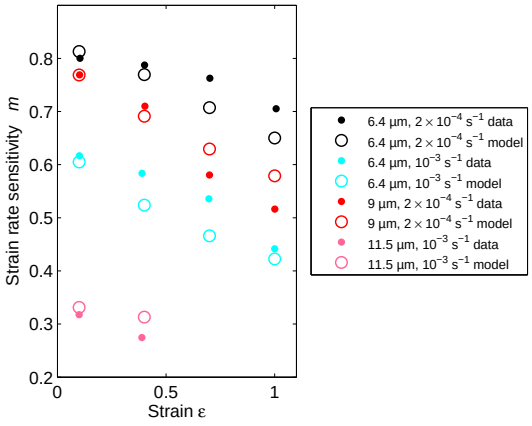

(b)

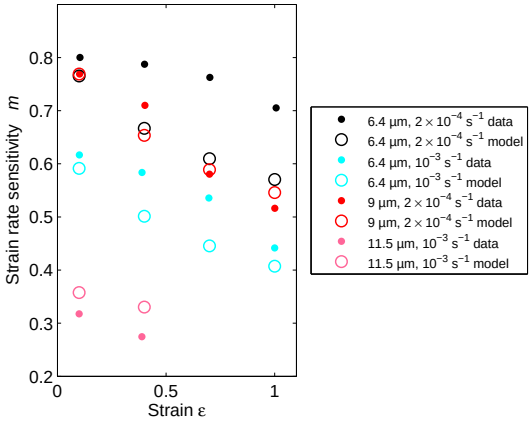

(c)

Figure 3.10: Strain rate sensitivity-strain experimental and model data for (a) set 1, (b) 2 and (c) 3 of the SV-sinh model

The grain size-time experimental and model data for the three different sets of weights with initial grain sizes 6.4 µm, 9 µm and 11.5 µm samples are compared in Figures 3.11, 3.12 and 3.13, respectively. The grain size errors for all three sets are almost the same with set 1 having the smallest grain size error.

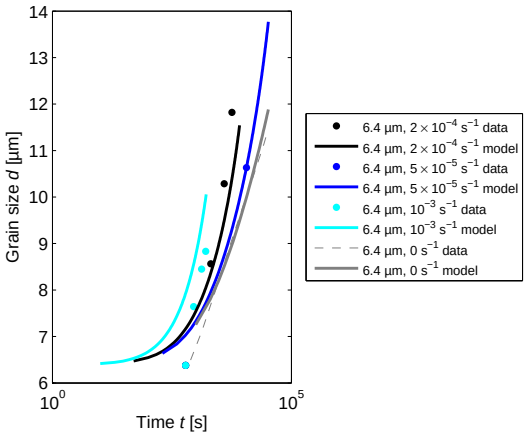

(a)

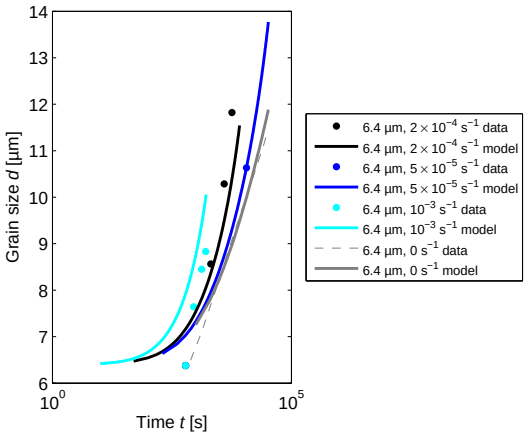

(b)

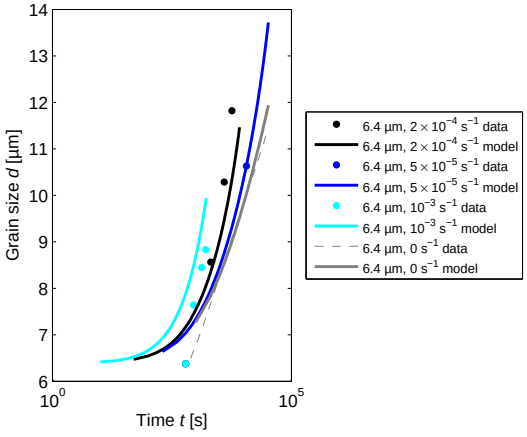

(c)

Figure 3.11: Grain size-time experimental and model data with an initial grain size of 6.4 µm for (a) set 1, (b) 2 and (c) 3 of the SV-sinh model

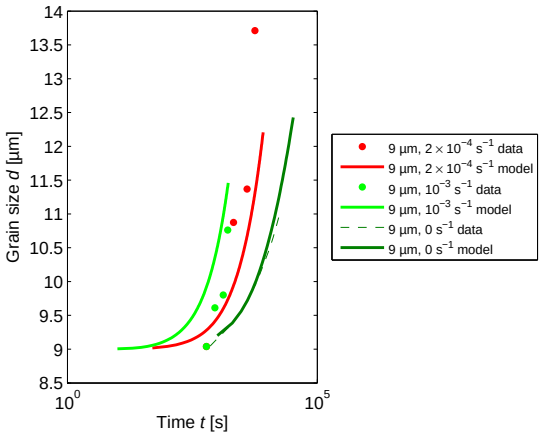

(a)

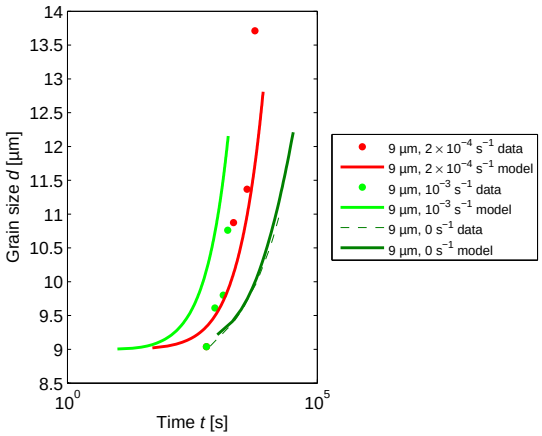

(b)

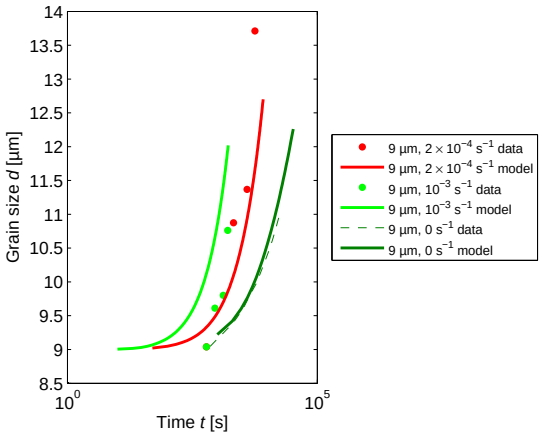

(c)

Figure 3.12: Grain size-time experimental and model data with an initial grain size of 9 µm for (a) set 1, (b) 2 and (c) 3 of the SV-sinh model

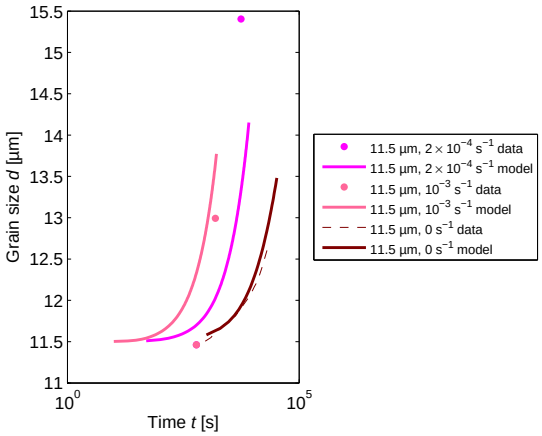

(a)

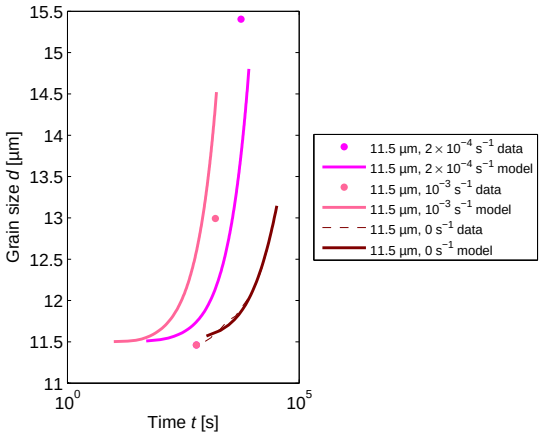

(b)

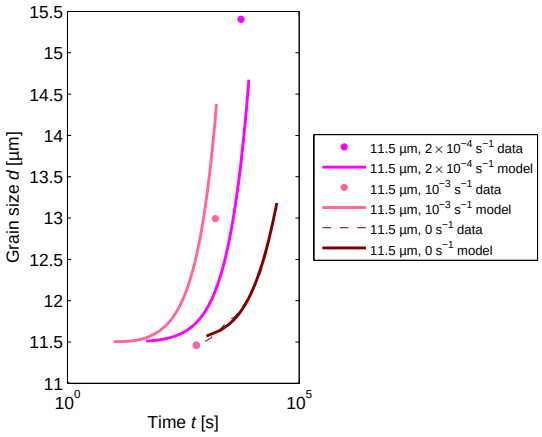

(c)

Figure 3.13: Grain size-time experimental and model data with an initial grain size of 11.5 µm for (a) set 1, (b) 2 and (c) 3 of the SV-sinh model

3.4.3.2 Effect of the amount of data

The effect that the amount of data used for the calibration has on the prediction of material behaviour outside the fitted data range is investigated. The weights of set 3 are used for this investigation. The optimised constants $\boldsymbol{x}_{\text{opt}}$ and final errors $\boldsymbol{e}$ for this investigation are given in Table 3.3. It can be observed that the stress error increases and the strain rate sensitivity error decreases when less data is used to calibrate the material model. The grain size error remains almost unchanged.

Table 3.3: Optimised material parameters and final errors for the different amounts of data used to calibrate the SV-sinh model

Data used	$\boldsymbol{x}_{\text{opt}}$	$\boldsymbol{e}$
6.4 µm only	4.1249 0.097067 0.27881 1.6971 $1.3181e{-09}$ 51.739 6.8653 1.0064 4.722 $1.2782e{-13}$	12 992 0.017553 28.327
6.4 µm and 9 µm	2.7731 0.11972 $7.2671e{-08}$ 0.10883 1.2079 3.2098 23.157 1.7486 5.2317 $2.3821e{-10}$	280.89 0.07711 28.785

The stress-strain experimental and model data of this investigation are compared in Figure 3.14. The stress error decreased 98% when the 9 µm data is included, and this error then decreased by another 55% when the 11.5 µm data is also included. It can be observed in Figure 3.14 that the prediction of material behaviour improved outside the fitted data range as more data is included in the calibration of the SV-sinh model. A material model should therefore not only be fitted to data of only one grain size and strain rate if the material model is going to be used in multi-axial simulations. This is because the material sees many grain sizes and strain rates during a multi-axial simulation. This happens when some parts of the sheet are in contact with the die (low strain rates in the forming sheet) and other parts are still forming into the die cavity (higher strain rates in the forming sheet) [9].

When Figure 3.14(a), Figure 3.14(b) and Figure 3.9(c) are compared it can be observed that

the lack of strain rate sensitivity data for the 6 µm sample strained at 5×10^{-5} s^{-1}, which is a sample with small grains strained at a relatively low strain rate, did not influence the stress-strain fit of this sample.

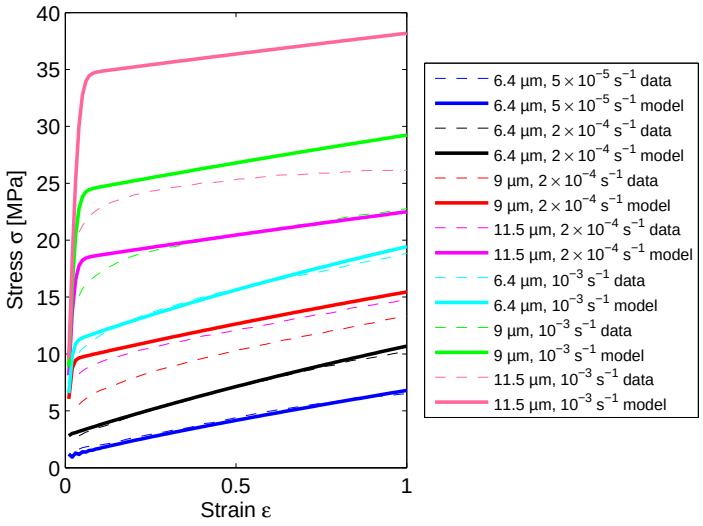

(a)

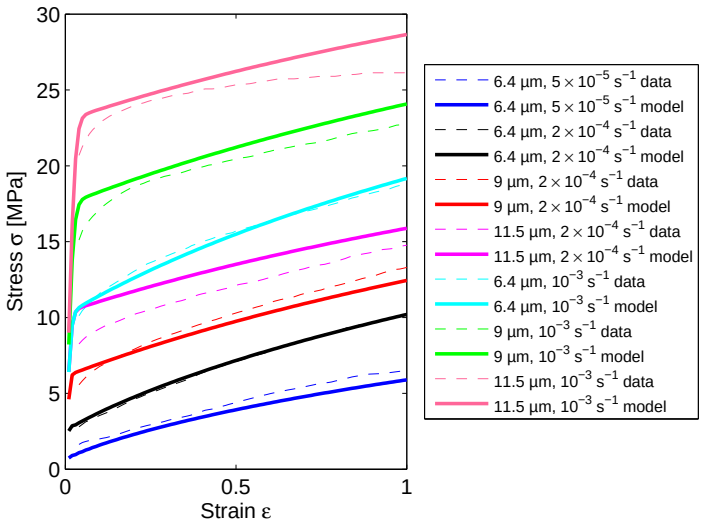

(b)

Figure 3.14: Stress-strain experimental and model data calibrated to data with an initial grain size of (a) 6.4 µm only, and (b) initial grain sizes of 6.4 µm and 9 µm

The strain rate sensitivity-strain experimental and model data for this investigation are

compared in Figure 3.15. The strain rate sensitivity error increased when more data is included in the calibration of the SV-sinh model. This result may be due to missing strain rate sensitivity data for the 9 µm sample strained at 10^{-3} s^{-1}, the 6 µm sample strained at 5×10^{-5} s^{-1}, and the 11.5 µm sample strained at 2×10^{-4} s^{-1}. It may also be may be due to uncertainty regarding the experimental stress-strain data from Ghosh and Hamilton [4], because homogeneous deformation is assumed for the experimental stress-strain curves. It may also be due to a lack of flexibility in the SV-sinh model, and the model cannot capture all of the data.

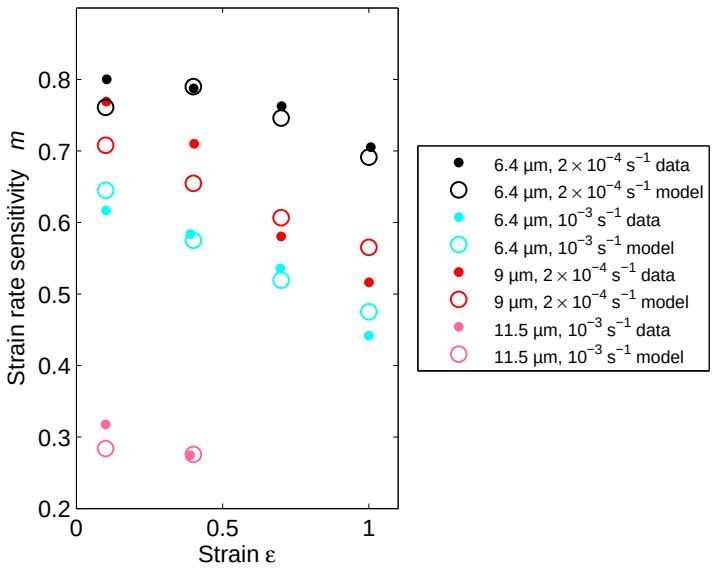

(a)

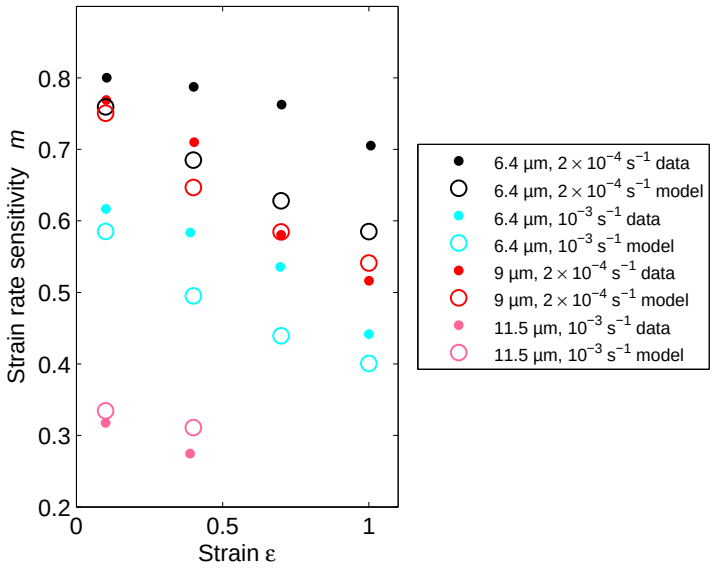

(b)

Figure 3.15: Strain rate sensitivity-strain experimental and model data calibrated to data with an initial grain size of (a) 6.4 µm only, and (b) initial grain sizes of both 6.4 µm and 9 µm

3.4.3.3 Verification of the calibration of the SV-sinh model

The implementation of the SV-sinh model is verified with a single element test in Abaqus. A 1 m × 1 m × 1 m cube, which consists of only one element, is strained to 100% at a strain rate of 10^{-3} s^{-1}. The constant strain rate is achieved by applying a velocity boundary condition to one surface. The magnitude of the applied velocity boundary condition v is given by [15]

$$v = L_0 \dot{\varepsilon} \exp(\dot{\varepsilon} t) \ , \tag{3.57}$$

where L_0 is the initial gauge length and t is the time from the start of the test.

The material is assumed to be Ti-6Al-4V with an initial grain size of 6.4 µm. The material parameters of set 3 are used in this investigation.

The stress at a node of the single element is compared to the stress-strain experimental data in Figure 3.16. It can be observed that the stress-strain model data matches the stress-strain experimental data. This confirms that the SV-sinh model is implemented correctly into Abaqus.

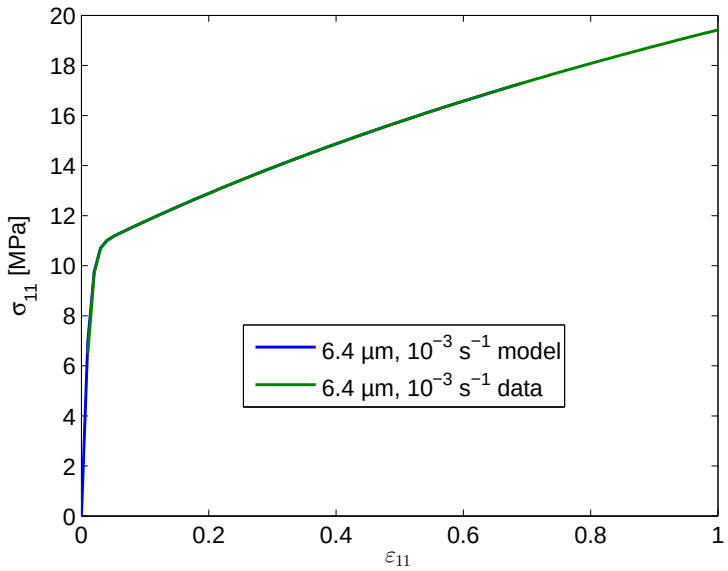

Figure 3.16: Stress-strain experimental and model data for the single element test

3.5 COMPARISON OF MATERIAL MODELS

3.5.1 Background

The calibrated material parameters of the tanh-model are $c_1 = 1.206$, $c_2 = 0.596$, $c_3 = 3.696$, $c_4 = 1.132$ and $c_5 = 0.167$. The calibrated material parameters of the power law model are $K = 10520.3$ and $m = 0.886$. The strain rate sensitivity-strain rate experimental and model data for the power law model and the tanh-model are compared in Figure 3.17. Notice that the strain rate sensitivity of the power law model does not vary with strain rate.

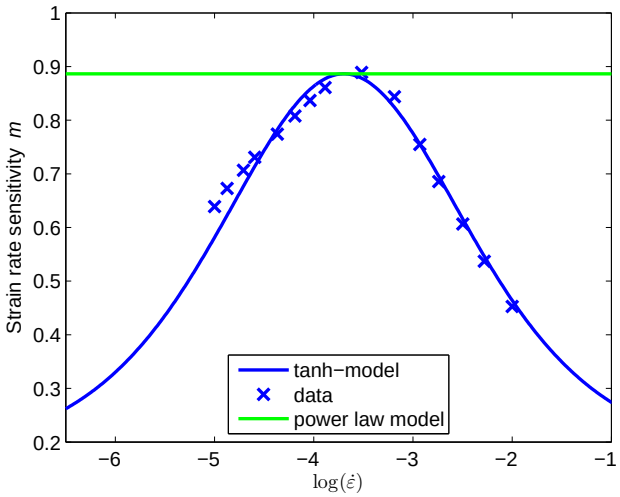

Figure 3.17: Strain rate sensitivity-strain rate experimental and model data for the power law model and the tanh-model

The material parameters of Lin's model is given by [21]

$$\begin{aligned} \boldsymbol{x} &= \left\{ \gamma \quad \beta_2 \quad k \quad \alpha_2 \quad b \quad Q \quad \alpha_1 \quad \beta_1 \quad \gamma_0 \quad \phi \right\} \\ &= \left\{ 1.408 \quad 0.035 \quad 0.242 \quad 0.042 \quad 1.729 \quad 6.345 \quad 1.2 \quad 3460.5 \quad 3.7 \quad 3.7 \right\} . \end{aligned} \tag{3.58}$$

The stress-strain experimental and model data for Lin's model are compared in Figure 3.18. Lin only used stress-strain and grain size-time experimental data with an initial grain size of 6.4 µm to calibrate his model. The consequence is that the fit of the stress-strain experimental data with initial grain sizes other than 6.4 µm are not as good as the fit of the stress-strain experimental data with an initial grain size of 6.4 µm. The stress error for Lin's model is

2109.8. This is 96%, 75% and 94% larger than the stress errors of set 1, 2 and 3 of the SV-sinh model, respectively.

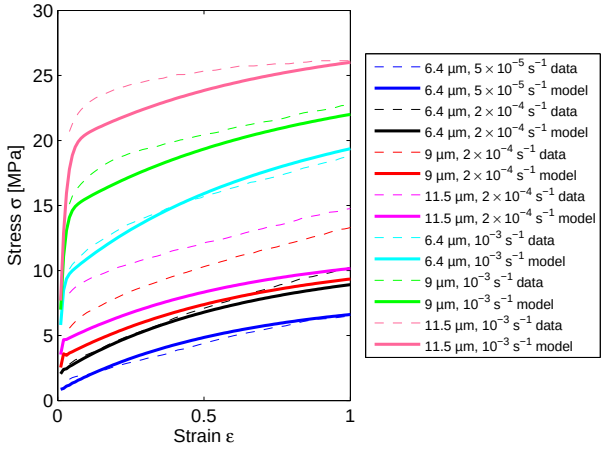

Figure 3.18: Stress-strain experimental and model data for Lin's model

The strain rate sensitivity-strain experimental and model data for Lin's model are compared in Figure 3.19. Lin did not use strain rate sensitivity-strain experimental data to calibrate his model. Limiting our attention to the 6.4 μm data, notice that the model strain rate sensitivity for a strain rate of 2×10^{-4} s^{-1} is significantly less than the strain rate sensitivity for a strain rate of 10^{-3} s^{-1}, where the opposite is observed experimentally. The strain rate sensitivity error is 1.3011. This is 86%, 98% and 93% larger than the strain rate sensitivity errors of set 1, 2 and 3 of the SV-sinh model, respectively.

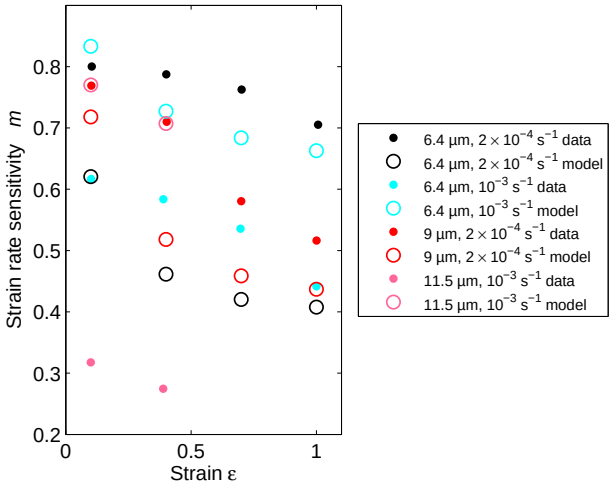

Figure 3.19: Strain rate sensitivity-strain experimental and model data for Lin's model

The grain size-time experimental data and model data with initial grain sizes 6.4 µm, 9 µm and 11.5 µm for Lin's model are compared in Figures 3.20, 3.21 and 3.22, respectively. It can be observed that the static grain size-time model data does not match the static grain size-time experimental data. The grain size error is 92.438 for Lin's model. This is 70%, 68% and 69% larger than the grain size errors of set 1, 2 and 3 of the SV-sinh model, respectively.

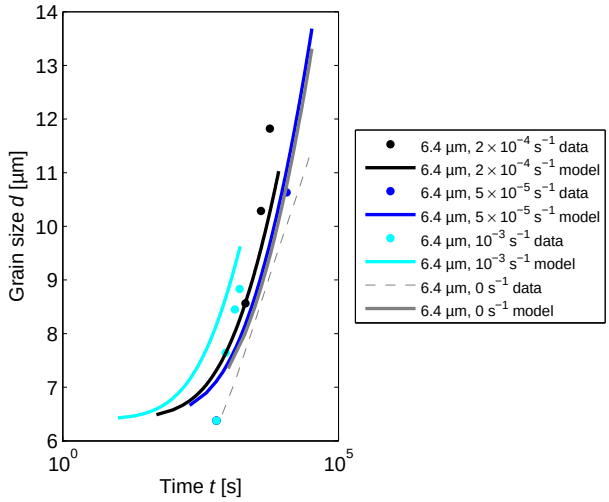

Figure 3.20: Grain size-time experimental and model data with an initial grain size of 6.4 µm sample for Lin's model

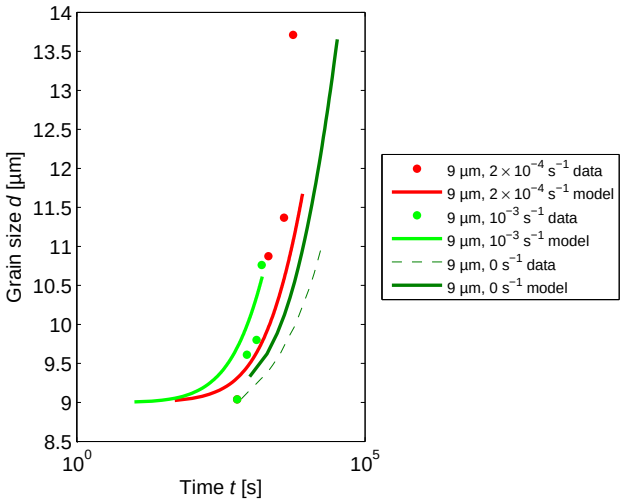

Figure 3.21: Grain size-time experimental and model data with an initial grain size of 9 µm sample for Lin's model

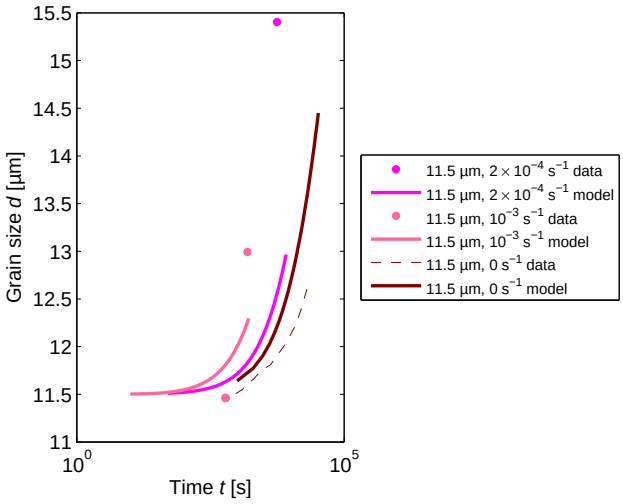

Figure 3.22: Grain size-time experimental and model data for Lin's model for the 11.5 µm sample

The finite element method is used to compare the four material models to each other. Two finite element models are used for this investigation:

1. A tensile test

2. The superplastic forming of a rectangular box

The finite element package used is Abaqus version 6.14 [34].

3.5.2 Tensile test

3.5.2.1 Method

The dimensions of the tensile test model are given in Figure 3.23. All of the dimensions are given in millimetres. The plate is 1.63 mm thick. The geometry is from Ghosh and Hamilton [15].

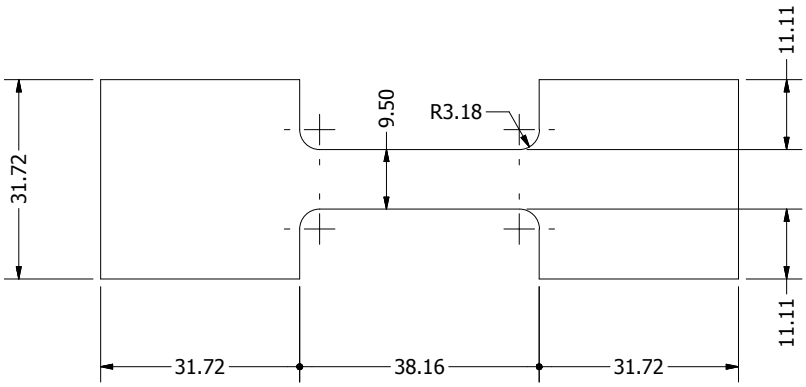

Figure 3.23: Dimensions of the tensile test model

The tensile test model is meshed with two layers of C3D8 elements. The meshed model is shown in Figure 3.24. The element and mesh refinement study are given in Appendix B.

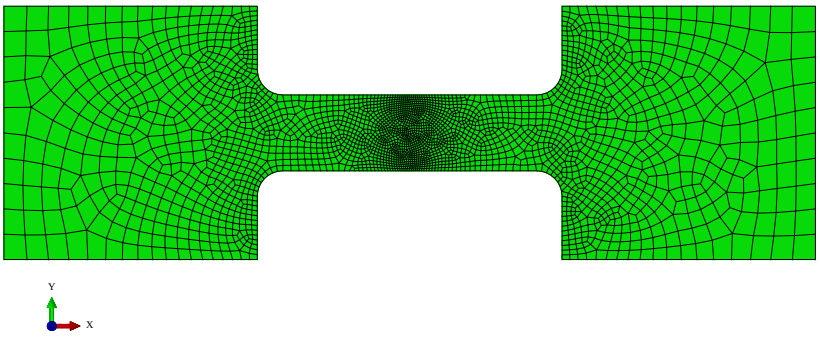

Figure 3.24: Meshed tensile test model

The boundary conditions of the tensile test model are shown in Figure 3.25. The boundary conditions of the tensile test model are based on the ASTM standard E2448-112011 [32]. The top and bottom surfaces of the tabs cannot displace in the y-direction. The middle line along the leftmost and righmost surfaces cannot displace in the z-direction. The left shoulder cannot displace in the x-direction. A velocity boundary condition is applied to the right shoulder of the specimen. The magnitude of the velocity boundary condition is given by Eq. (3.57). The tensile test model is strained to 250% at constant strain rates 10^{-3} s^{-1}, 2×10^{-3} s^{-1} and 5×10^{-3} s^{-1} for this investigation.

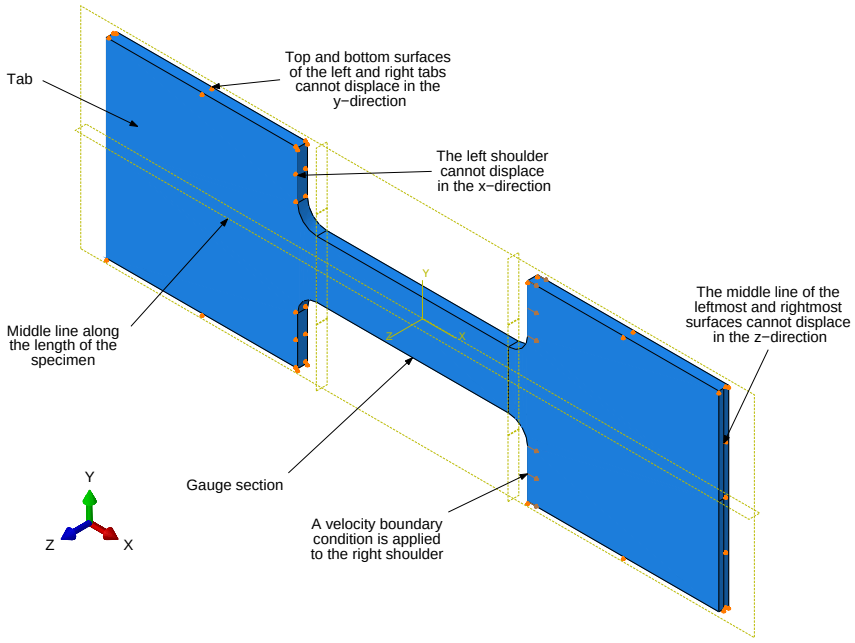

Figure 3.25: Boundary conditions of the tensile test model

3.5.2.2 Results

The final thickness distribution results of the tensile test model for the power law model, tanh-model, Lin's model and the SV-sinh model at 10^{-3} s^{-1} are given in Figure 3.26. The method used to calculate the thickness is described in Appendix B. It can be observed in Figure 3.26 that only set 1 and 3 of the SV-sinh model show thinning in the gauge section at this strain rate.

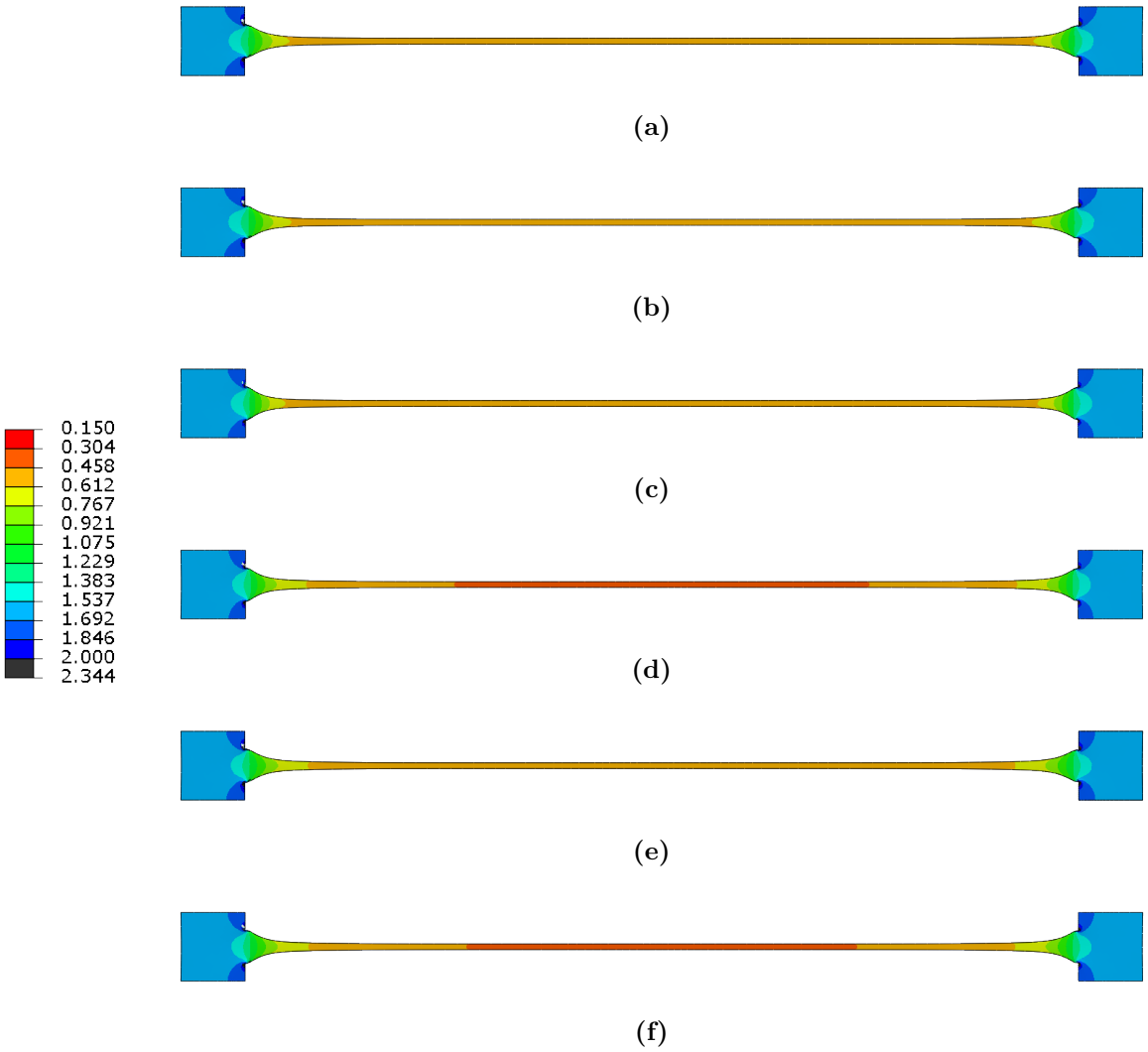

Figure 3.26: Final thickness results of the tensile test for the (a) power law model, (b) tanh-model, (c) Lin's model and (d) set 1, (e) set 2, and (f) set 3 of the SV-sinh model at 10^{-3} s^{-1}

The final thickness distribution results of the tensile test model for the power law model, tanh-model, Lin's model and the SV-sinh model at 2×10^{-3} s^{-1} are given in Figure 3.27. The power law model, tanh-model and Lin's model do not seem to be as sensitive to an increase in strain rate as compared to the SV-sinh model.

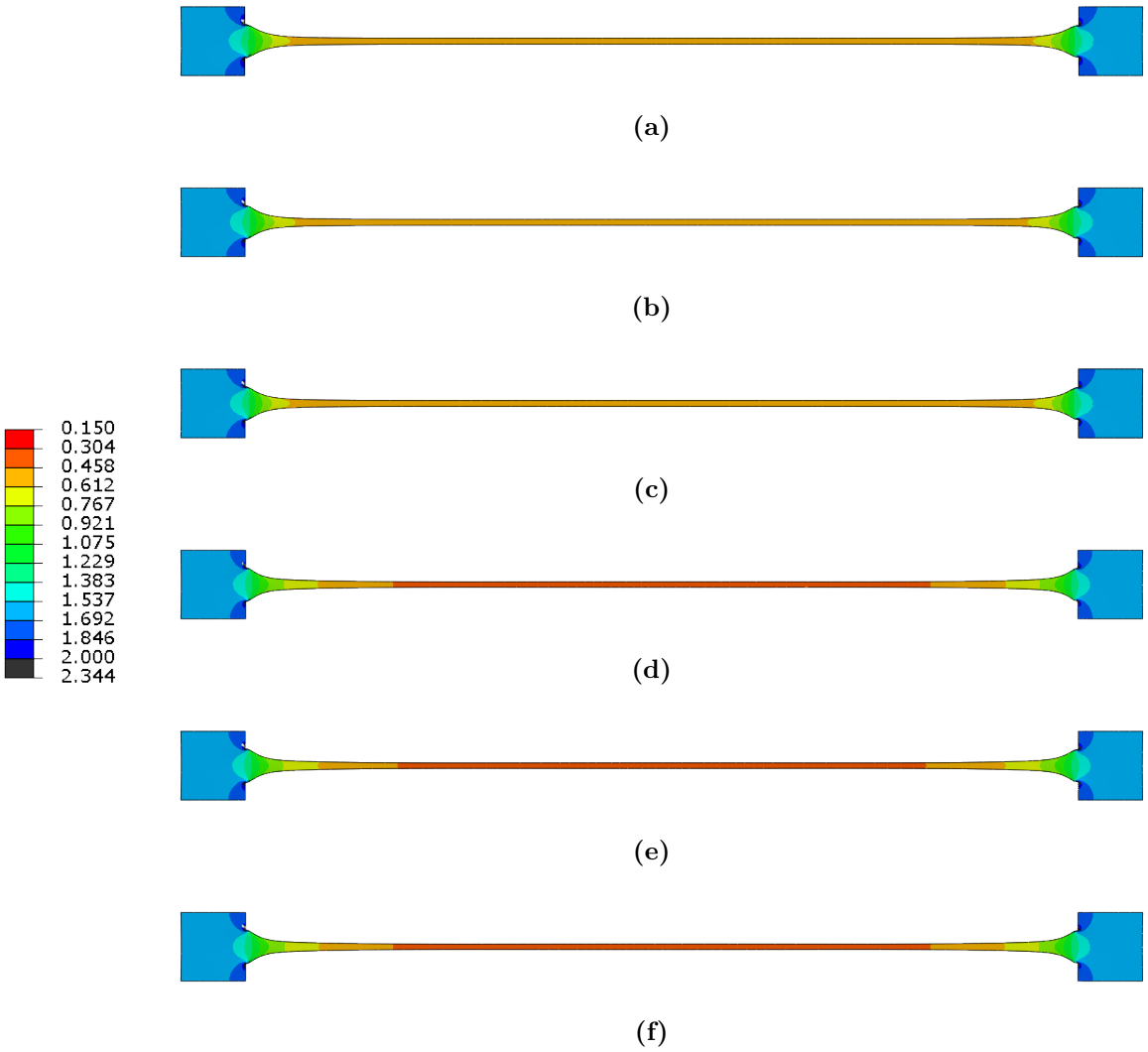

Figure 3.27: Final thickness results of the tensile test for the (a) power law model, (b) tanh-model, (c) Lin's model and (d) set 1, (e) set 2, and (f) set 3 of the SV-sinh model at 2×10^{-3} s^{-1}

The final thickness distribution results of the tensile test model for the power law model, tanh-model, Lin's model and the SV-sinh model at 5×10^{-3} s^{-1} are given in Figure 3.28. The power law model and Lin's model do not show as strong a diffuse neck in the gauge section at 5×10^{-3} s^{-1} as compared to the other models. The SV-sinh model fails at this strain rate.

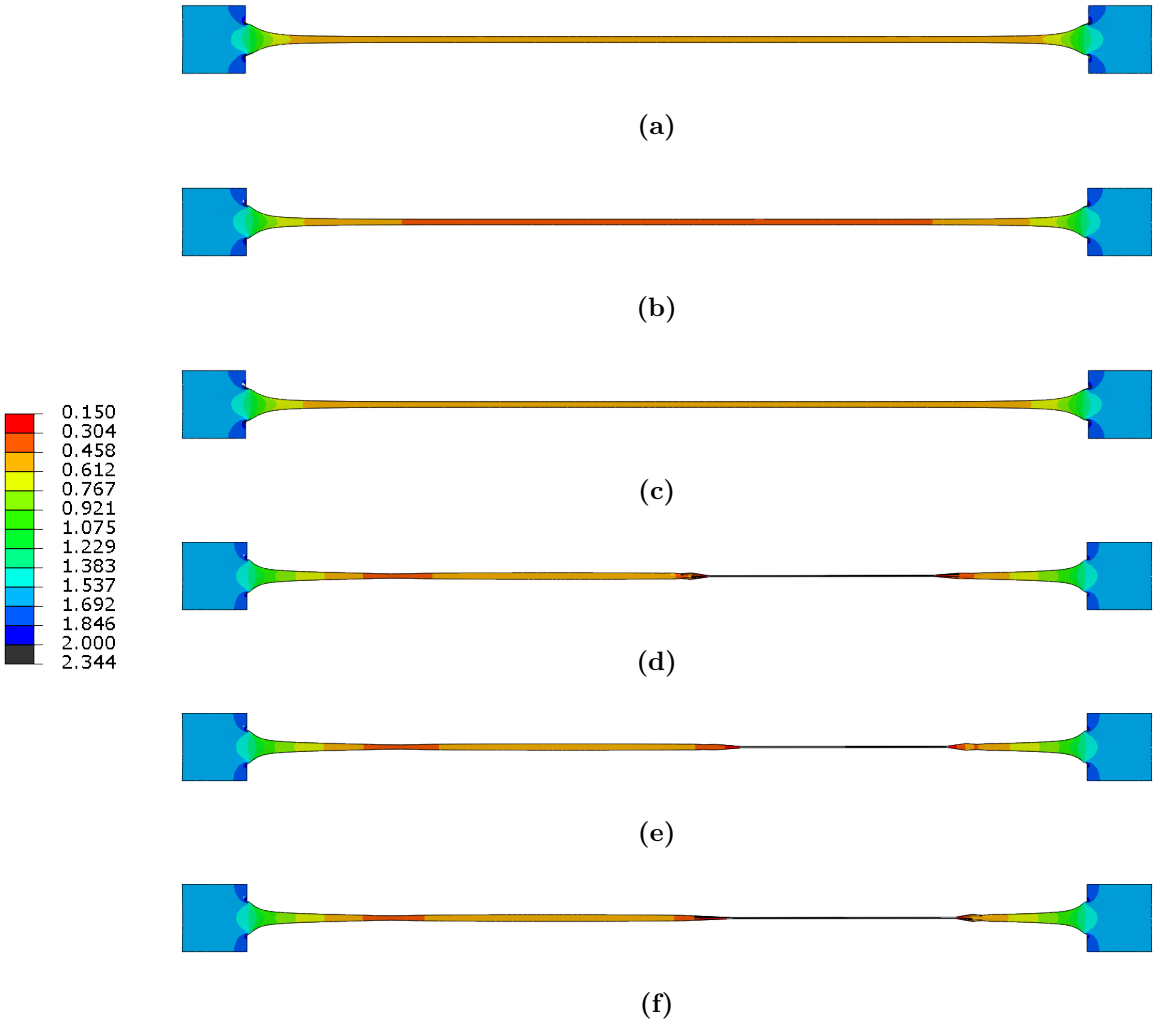

Figure 3.28: Final thickness results of the tensile test for the (a) power law model, (b) tanh-model, (c) Lin's model and (d) set 1, (e) set 2, and (f) set 3 of the SV-sinh model at 5×10^{-3} s^{-1}

The final thickness results along the middle of the tensile test model for the power law model, tanh-model, Lin's model and the SV-sinh model at 10^{-3} s^{-1}, 2×10^{-3} s^{-1} and 5×10^{-3} s^{-1} are given in Figure 3.29. The middle is the line along the x-axis of the tensile test model. It can be observed that most of the deformation is in the gauge section. The thickness results are non-uniform in the gauge section for the SV-sinh model at 5×10^{-3} s^{-1} unlike the power law model, tanh-model and Lin's model. This indicates that the SV-sinh model failed at or near the end of the 5×10^{-3} s^{-1} simulation.

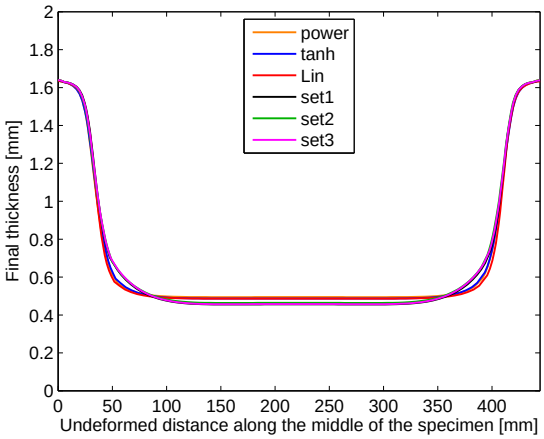

(a)

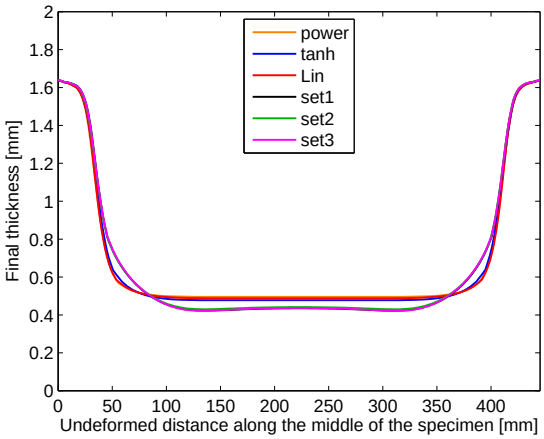

(b)

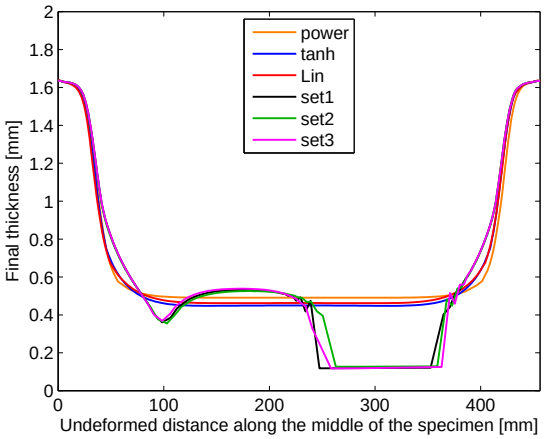

(c)

Figure 3.29: Final thickness results along the middle of the tensile test model for the different material models at (a) 10^{-3} s^{-1}, (b) 2×10^{-3} s^{-1} and (c) 5×10^{-3} s^{-1}

The final minimum thickness $h_{\text{f,min}}$ results of the tensile test model for the power law model, tanh-model, Lin's model and the SV-sinh model at 10^{-3} s^{-1}, 2×10^{-3} s^{-1} and 5×10^{-3} s^{-1} are given in Table 3.4. The final minimum thickness results of the power law model shows the least variation with increasing strain rate where the difference between the final minimum thickness results at 10^{-3} s^{-1} and 5×10^{-3} s^{-1} is 0.73%. Lin's model is in second place with only a 5% difference between the final minimum thickness results at 10^{-3} s^{-1} and 5×10^{-3} s^{-1}. The tanh-model is in third place with an 8% difference between the final minimum thickness results at 10^{-3} s^{-1} and 5×10^{-3} s^{-1}.

The final minimum thickness results of the SV-sinh model decreased the most with increasing strain rate. The difference between the final minimum thickness results at 10^{-3} s^{-1} and 2×10^{-3} s^{-1} is 7.2%, 7.3% and 7.7% for set 1, 2 and 3, respectively. The difference between the final minimum thickness results at 2×10^{-3} s^{-1} and 5×10^{-3} s^{-1} is 72%, 71% and 72% for set 1, 2 and 3, respectively.

Table 3.4: Final minimum thickness results of the material models investigated at 10^{-3} s^{-1}, 2×10^{-3} s^{-1} and 5×10^{-3} s^{-1} for the tensile test

Material model	$h_{\text{f,min}}$ at 10^{-3} s^{-1} [mm]	$h_{\text{f,min}}$ at 2×10^{-3} s^{-1} [mm]	$h_{\text{f,min}}$ at 5×10^{-3} s^{-1} [mm]
SV-sinh model, set 1	0.4554	0.4225	0.1178 *
SV-sinh model, set 2	0.4633	0.4295	0.1263 *
SV-sinh model, set 3	0.4567	0.4215	0.1173 *
Power law model	0.4942	0.4952	0.4906
tanh-model	0.4869	0.4776	0.4479
Lin's model	0.4860	0.4878	0.4619

* Value may be inaccurate due to localised thinning at or near the end of the simulation

The distance between the bottom and top midnodes of the middle (along the y-axis) of the gauge specimen is recorded with time. The results are plotted against normalised time in Figure 3.30. The distance results of the power law model is the same for all three strain rates. The distance results of the tanh-model and Lin's model only changed at 5×10^{-3} s^{-1}. The distance results of the SV-sinh model changed the most with increasing strain rate. The flat part of the curves in Figures 3.30(d), 3.30(e) and 3.30(f) for the SV-sinh model is nonsensical

and indicates localised thinning at or near the end of the simulation.

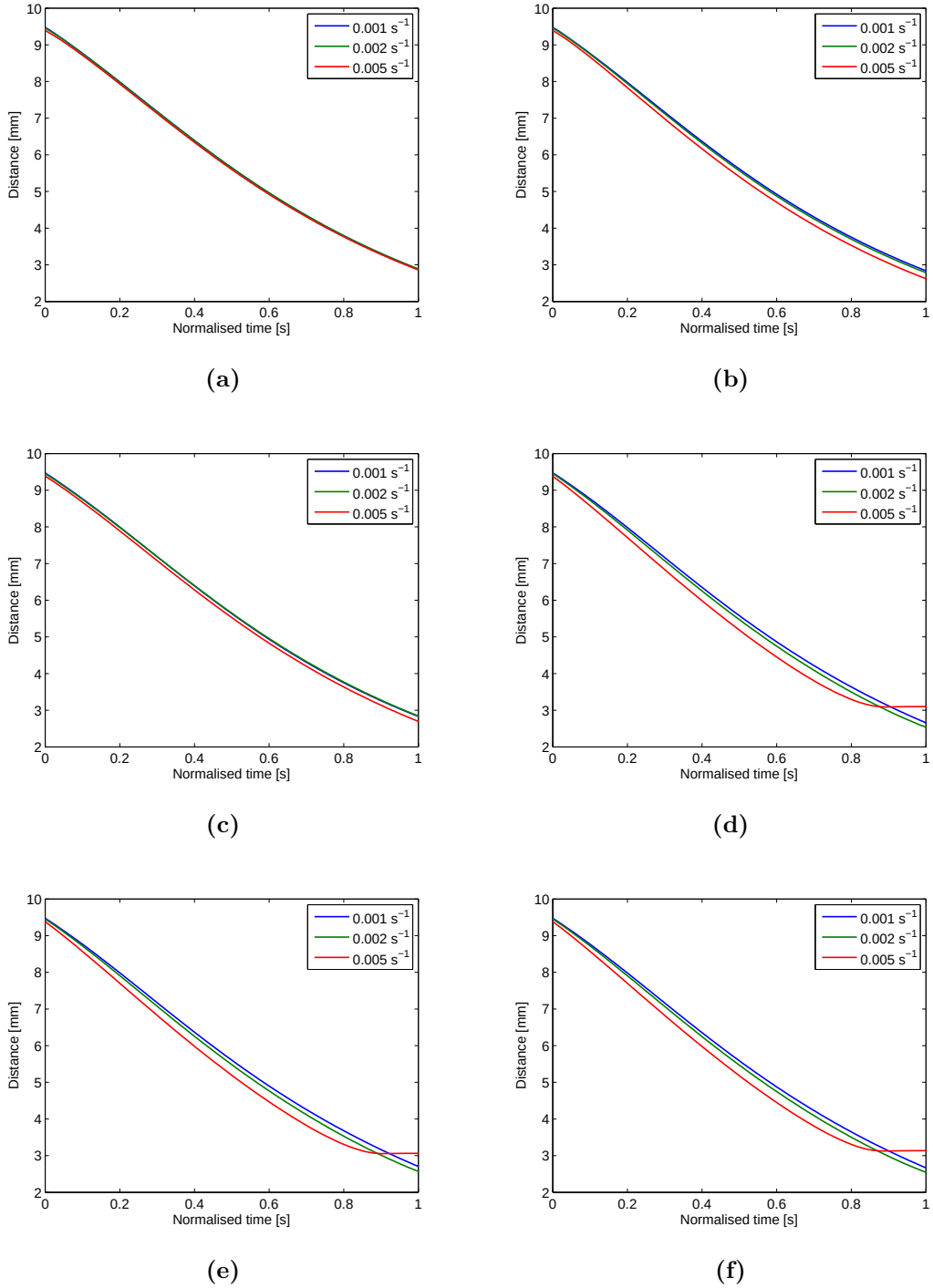

Figure 3.30: Distance between the bottom and top nodes of the middle of the gauge specimen against time for the (a) power law model, (b) tanh-model, (c) Lin's model, and (d) set 1, (e) set 2 and (f) set 3 of the SV-sinh model

The maximum strain rate versus the deformed, normalised deformed and undeformed distance along the middle of the specimen with time for set 3 of the SV-sinh model at 10^{-3} s^{-1} are shown in Figures 3.31, 3.32 and Figure 3.33, respectively. It can be observed that the strain rate increases with time throughout the gauge section. The increase in strain rate in the gauge section is 57% from 10 s to 2480 s. It can also be observed that there is flow of material from the tabs to the gauge section during deformation which also increases with time.

The stress-strain experimental data is therefore not at the reported constant strain rates. This problem can be solved by

- calibrating the material model with the finite element method in the loop [35],
- redesigning the tensile test specimen, or
- modifying the magnitude of the velocity with time.

These solutions are not included in the scope of the study, because the first solution is computationally expensive, since every function evaluation of the calibration requires a finite element simulation. There are seven stress-strain curves that will each require a finite element model.

The second and third solutions will require experimentation. The calibrated SV-sinh model developed so far does however show the onset of localised thinning with increasing strain rate, and can therefore be used to minimise the final forming time.

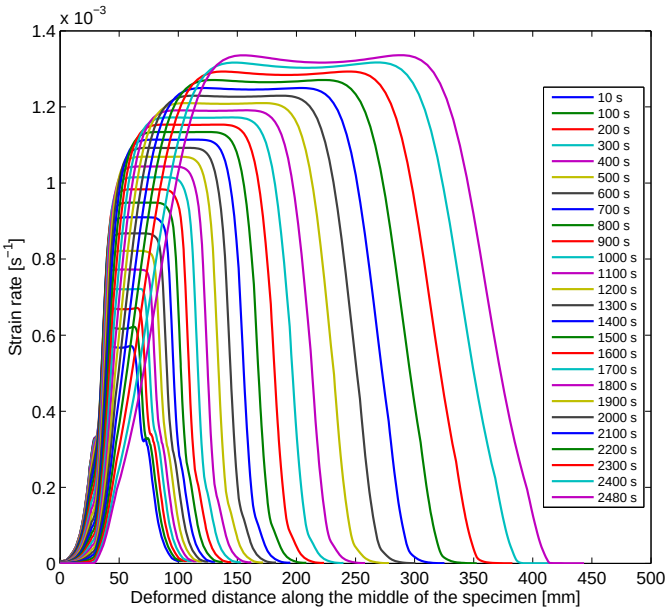

Figure 3.31: Maximum strain rate versus deformed distance along the middle of the specimen with time for set 3 of the SV-sinh model at 10^{-3} s^{-1}

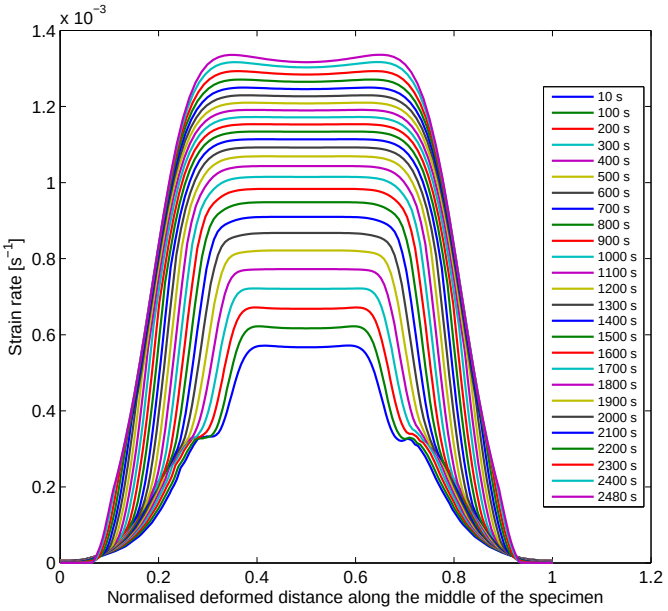

Figure 3.32: Maximum strain rate versus the normalised deformed distance along the middle of the specimen with time for set 3 of the SV-sinh model at 10^{-3} s^{-1}

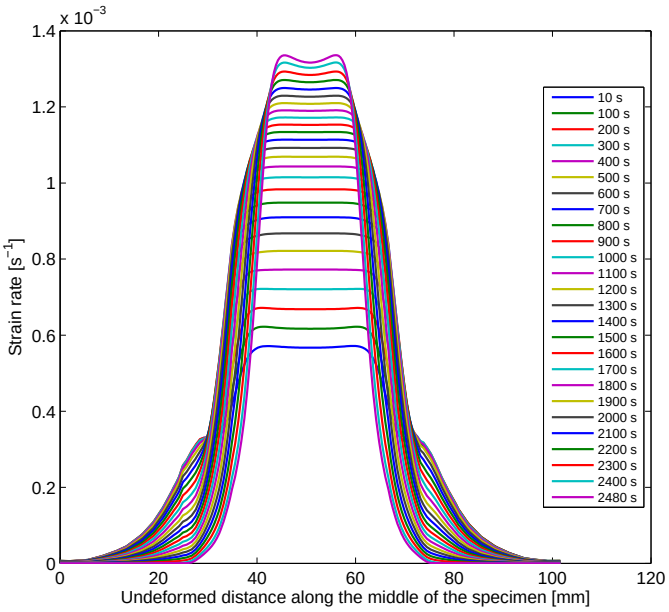

Figure 3.33: Maximum strain rate versus undeformed distance along the middle of the specimen with time for set 3 of the SV-sinh model at 10^{-3} s^{-1}

3.5.3 Superplastic forming of a rectangular box

3.5.3.1 Method

The dimensions of the die are given in Figure 3.34. All of the dimensions are given in millimetres. The geometry is from the Abaqus user guide [34]. Only a quarter of the rectangular box is modelled due to symmetry in two planes. The sheet size is 558.8 mm $\times$ 812.8 mm $\times$ 3.3 mm.

The sheet is meshed with $60 \times 100 \times 1$ C3D8 elements and the die is meshed with R3D4 and R3D3 rigid elements. The meshed model is shown in Figure 3.35. The element and mesh refinement study of this model are given in Appendix B.

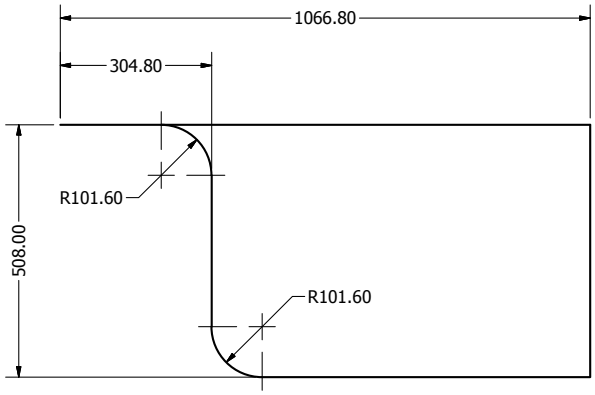

(a)

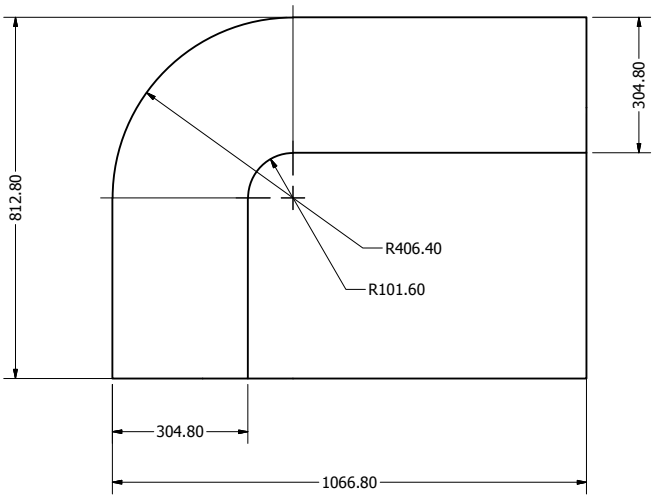

(b)

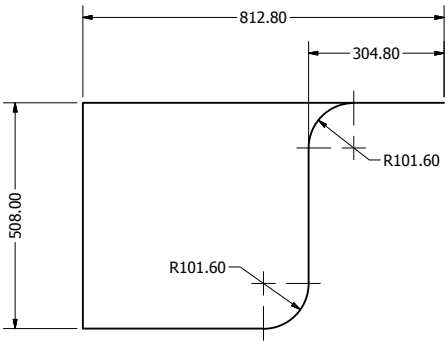

(c)

Figure 3.34: Die dimensions in the (a) xy-view, (b) xz-view and (c) yz-view

The boundary conditions of the box and sheet assembly are also given in Figure 3.35. The die is modelled as a rigid surface, since the die is practically non-deformable in comparison to the large deformations of the forming sheet. Symmetry conditions are applied to the inner edge surfaces of the sheet, whereas the outer edge surfaces of the sheet can only displace in the y-direction. The lower edges of the outer edge surfaces of the sheet are fixed. Pressure is applied to the top surface of the sheet.

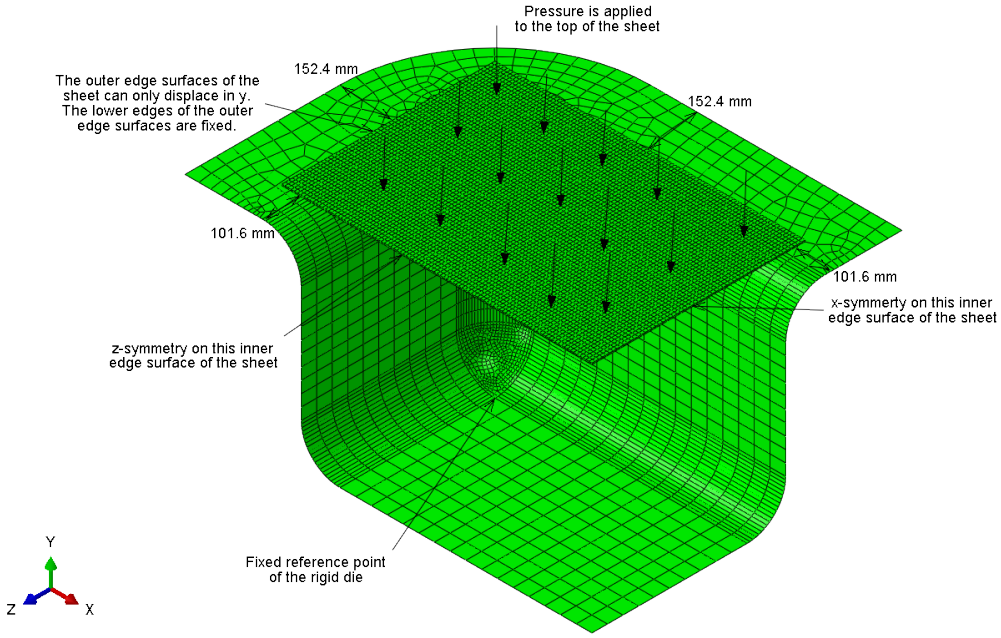

Figure 3.35: Boundary conditions of the superplastic forming of a rectangular box

The pressure is determined using an automatic update procedure or adaptive optimisation strategy denoted as autopress. This solution-dependent pressure is available in Abaqus. Autopress calculates the ratio of the maximum equivalent strain rate to the target strain rate for every integration point in an element of the sheet. This ratio $r_{\max}$ is then compared to the target ratio, which is 1.0, in order to update the magnitude of the pressure for the next iteration p. The autopress routine is summarised below.

$$\text{If } r_{\max} < 0.2, \text{ then } p = 2.0p_{\text{old}}$$

$$\text{If } 0.2 \leq r_{\max} < 0.5, \text{ then } p = 1.5p_{\text{old}}$$

$$\text{If } 0.5 \leq r_{\max} < 0.8, \text{ then } p = 1.2p_{\text{old}}$$

$$\text{If } 0.8 \leq r_{\max} < 1.5, \text{ then } p = p_{\text{old}}$$

$$\text{If } 1.5 \leq r_{\max} < 3.0, \text{ then } p = p_{\text{old}}/1.2$$

$$\text{If } r_{\max} > 3.0, \text{ then } p = 0.5p_{\text{old}} \ ,$$

where p_{old} is the pressure of the previous iteration.

The autopress pressure-times curves are different for each material model. The same pressure is applied in the following investigation in order to compare the different material models to each other. The autopress pressure-time curves for set 3 of the SV-sinh model at target strain rates of 10^{-3} s^{-1}, 2×10^{-3} s^{-1} and 5×10^{-3} s^{-1}, which are shown in Figure 3.36, are used for this investigation.

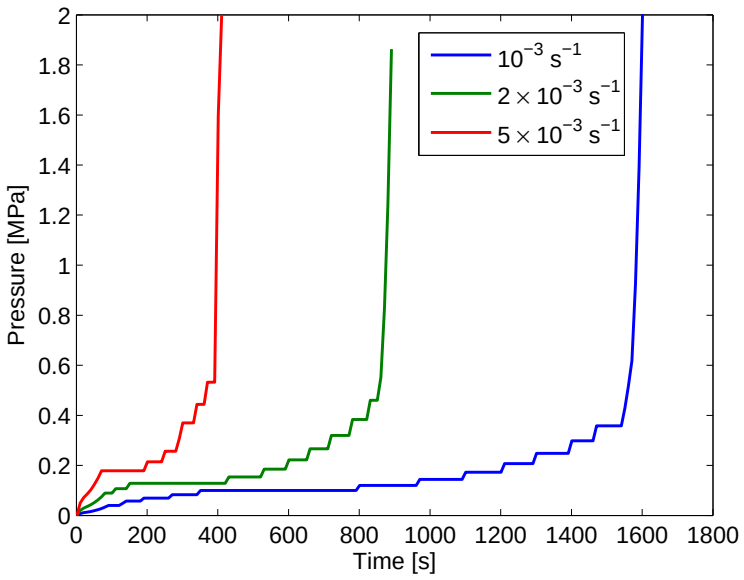

Figure 3.36: Autopress pressure-time curves for set 3 of the SV-sinh model

3.5.3.2 Results

The final thickness distribution results of the formed box for the power law model, tanh-model, Lin's model and the SV-sinh model at 10^{-3} s^{-1} are given in Figure 3.37. It can be observed that the greatest thinning occurs in the die corner which is the last part to make contact with the die surface. The least thinning occurs at the top corner of the formed sheet. The thickness results of the power law model and tanh-model show the least thinning in the die corner, whereas the thickness results of Lin's model and the SV-sinh model show the greatest thinning in the die corner at 10^{-3} s^{-1}.

The final thickness distribution results of the formed box for the power law model, tanh-model, Lin's model and the SV-sinh model at 2×10^{-3} s^{-1} are given in Figure 3.38. The thickness results of the tanh-model and Lin's model are similar in the die corner, whereas the thickness results of the SV-sinh model show the greatest thinning in the die corner at 2×10^{-3} s^{-1}. The area of minimum thickness for the power law model at 2×10^{-3} s^{-1} is smaller than at 10^{-3} s^{-1}. This indicates that the finite element model using the power law material model did not finish forming for the same applied pressure.

The final thickness distribution results of the formed box for the power law model, tanh-model, Lin's model and the SV-sinh model at 5×10^{-3} s^{-1} are given in Figure 3.39. The thickness results of the SV-sinh model shows the greatest thinning at the bottom of the die.

The gradient of the thickness results of the SV-sinh model is greater than the results at the lower strain rates. The difference in thickness results between the three sets of the SV-sinh model does not seem to be significant at the three strain rates investigated.

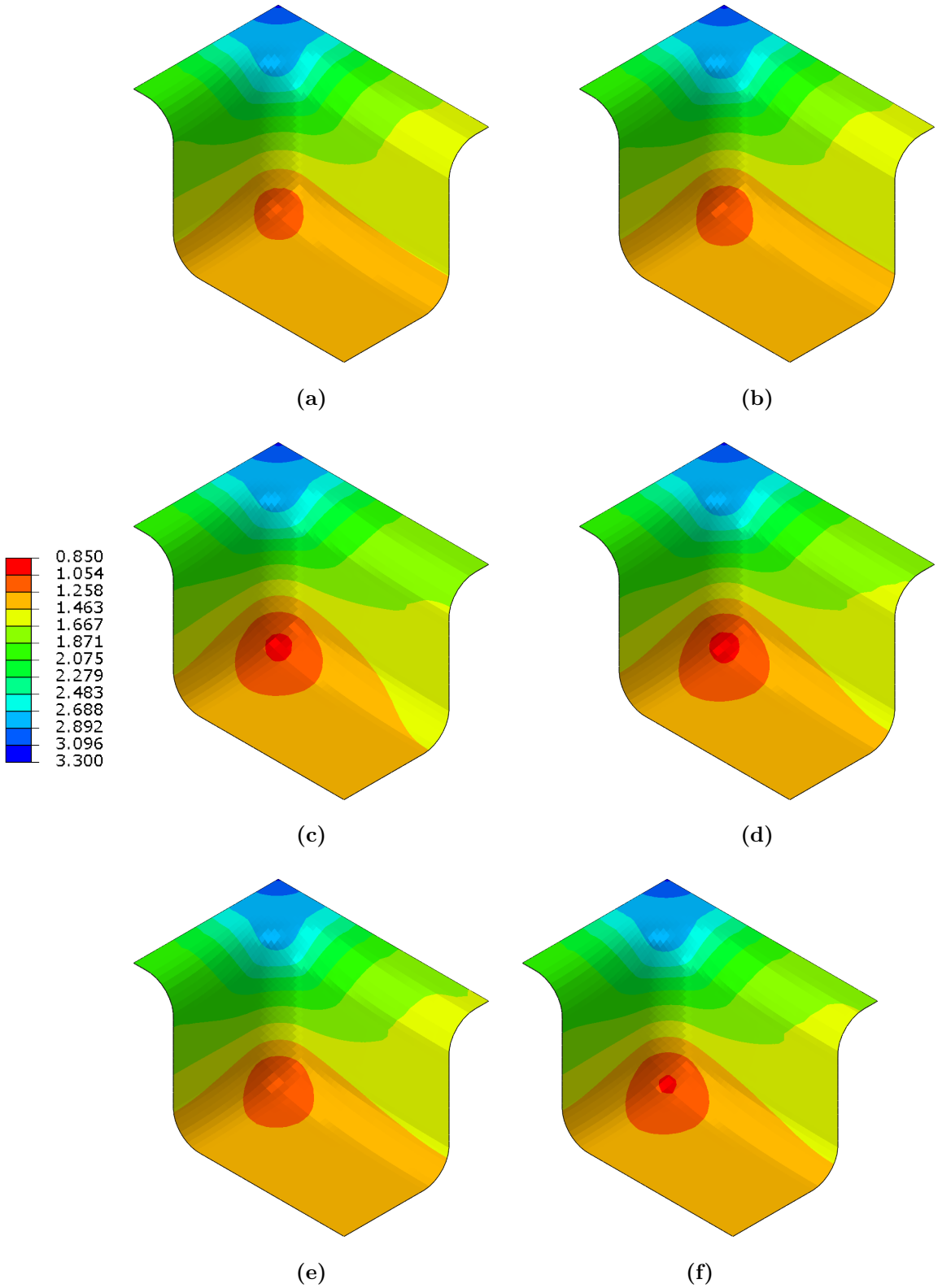

Figure 3.37: Final thickness results of the formed box for the (a) power law model, (b) tanh-model, (c) Lin's model and (d) set 1, (e) set 2, and (f) set 3 of the SV-sinh model at 10^{-3} s^{-1}

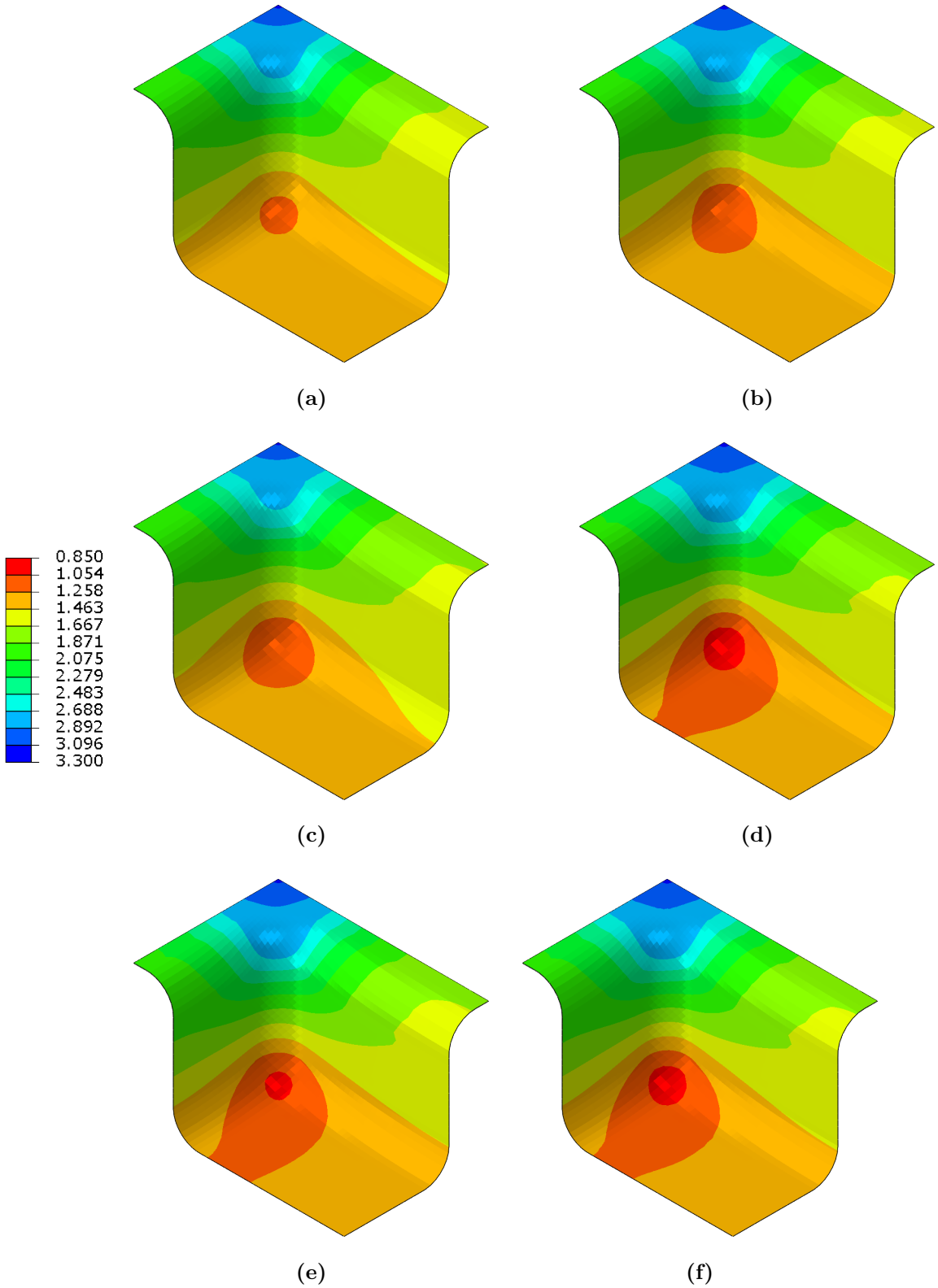

Figure 3.38: Final thickness results of the formed box for the (a) power law model, (b) tanh-model, (c) Lin's model and (d) set 1, (e) set 2, and (f) set 3 of the SV-sinh model at 2×10^{-3} s^{-1}

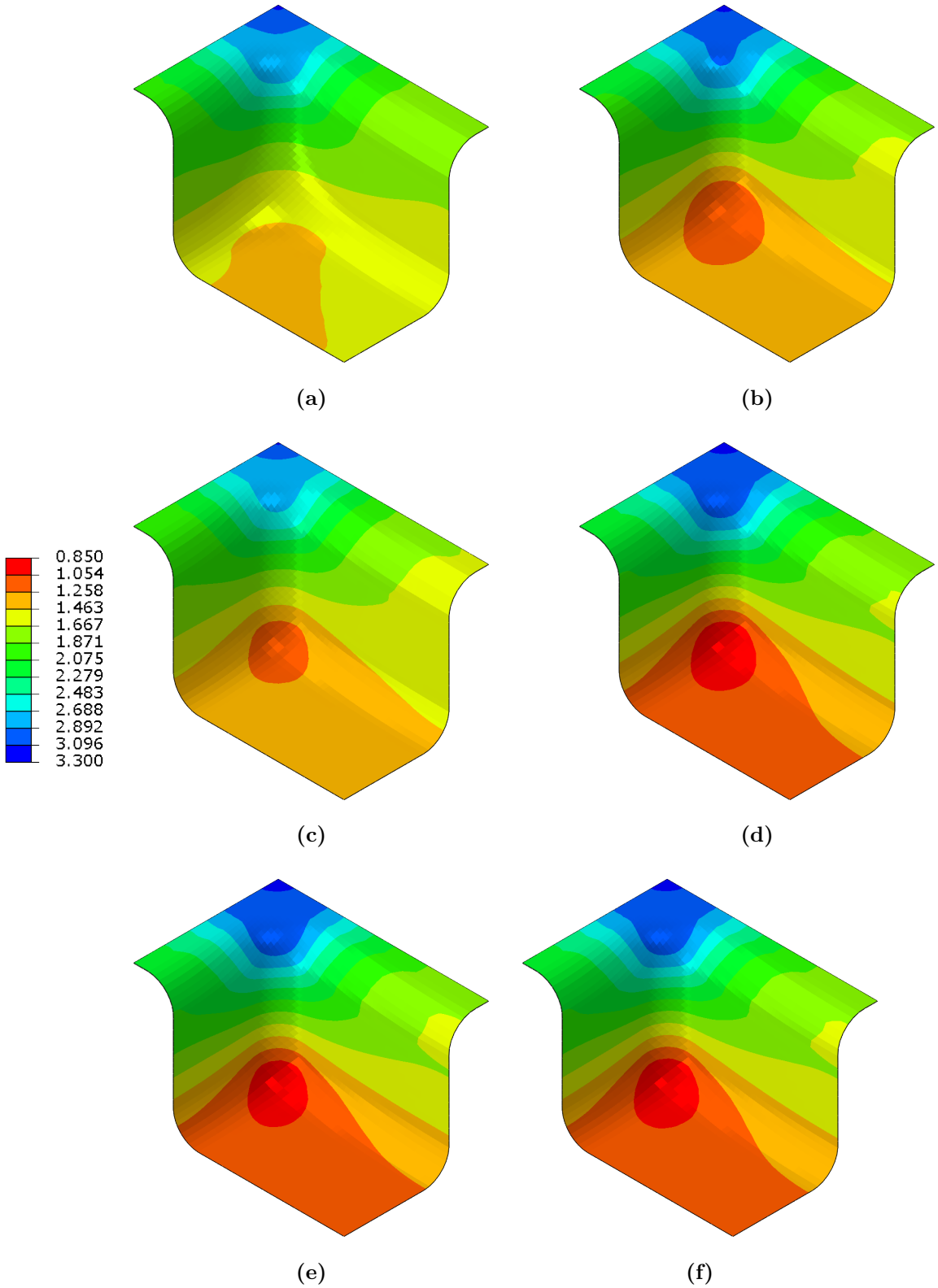

Figure 3.39: Final thickness results of the formed box for the (a) power law model, (b) tanh-model, (c) Lin's model and (d) set 1, (e) set 2, and (f) set 3 of the SV-sinh model at 5×10^{-3} s^{-1}

The final thickness results along the diagonal of the formed box for the power law model, tanh-model, Lin's model and the SV-sinh model at 10^{-3} s^{-1} are given in Figure 3.40. The diagonal is taken as the line 45° from the top corner of the sheet. The final thickness results along the diagonal for Lin's model and the SV-sinh model lie mostly on top of each other at 10^{-3} s^{-1}. The largest difference in thickness results between the different material models are at the die corner at 10^{-3} s^{-1}.

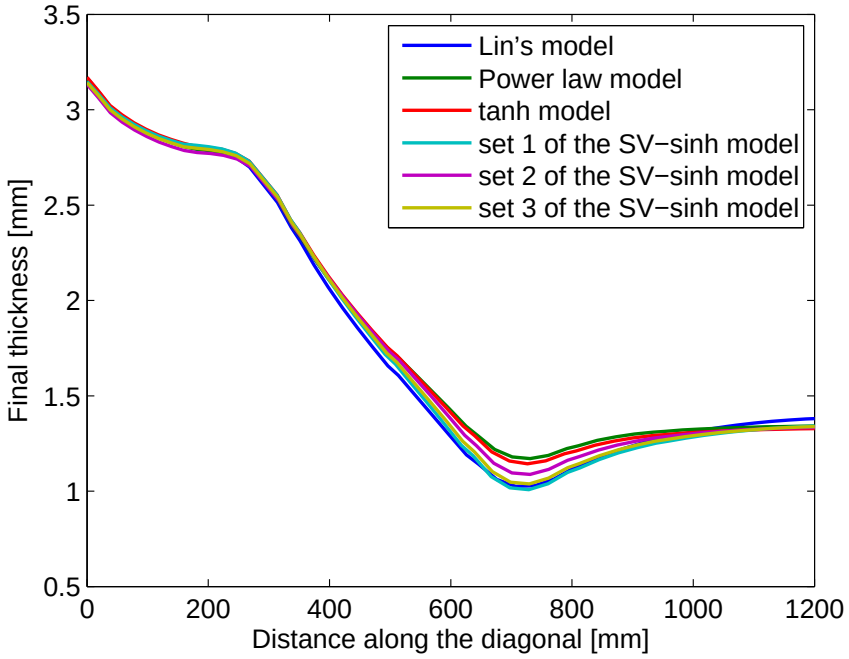

Figure 3.40: Final thickness results along the long the diagonal of the formed box for the power law model, tanh-model, Lin's model and the SV-sinh model at 10^{-3} s^{-1}

The final thickness results along the diagonal of the formed box for the power law model, tanh-model, Lin's model and the SV-sinh model at 2×10^{-3} s^{-1} are given in Figure 3.41. The difference in thickness results between the different material models are at the die corner, die entry radius and die centre. The power law model is not as thin as the other material models at the die corner. This indicates that the finite element model using the power law material model did not finish forming for the same applied pressure.

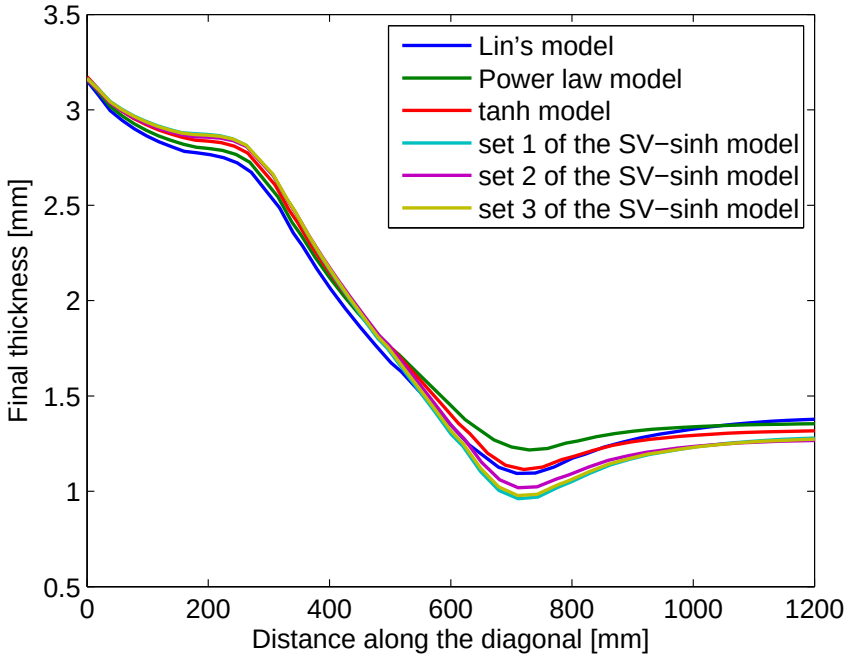

Figure 3.41: Final thickness results along the long the diagonal of the formed box for the power law model, tanh-model, Lin's model and the SV-sinh model at 2×10^{-3} s^{-1}

The final thickness results along the diagonal of the formed box for the power law model, tanh-model, Lin's model and the SV-sinh model at 5×10^{-3} s^{-1} are given in Figure 3.42. The difference in thickness results between the different material models are significant everywhere along the diagonal of the formed sheet at 5×10^{-3} s^{-1}. It can again be observed that the finite element model using the power law material model did not finish forming for the same applied pressure.

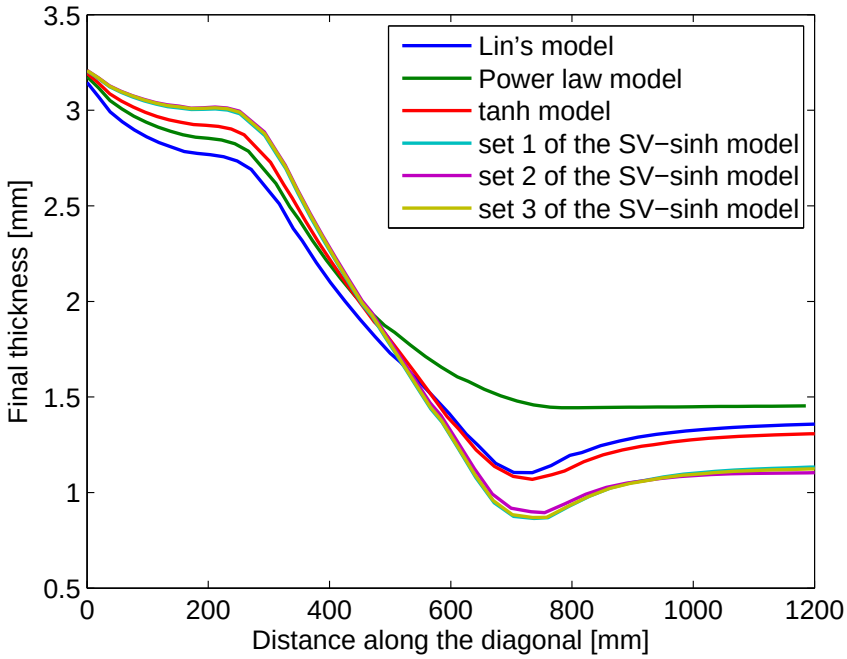

Figure 3.42: Final thickness results along the long the diagonal of the formed box for the power law model, tanh-model, Lin's model and the SV-sinh model at 5×10^{-3} s^{-1}

The final minimum thickness $h_{\text{f,min}}$ results for the material models at the three strain rates are given in Table 3.5. The final gap g_{f} between the die and the sheet is also reported in Table 3.6. The gap g is calculated as the orthogonal projected distance between the die corner node $\boldsymbol{C}_{\text{die}} = \langle -58.659, 42.941, -58.659 \rangle$ and the nodes on the bottom surface of the sheet $\boldsymbol{C}_{\text{sheet}}$

$$g = \|\boldsymbol{C}_{\text{sheet}} - \boldsymbol{C}_{\text{die}}\| \cdot \frac{\boldsymbol{N}}{|\boldsymbol{N}|} \ , \tag{3.59}$$

where normal of the die corner is given by $\boldsymbol{N} = \langle 15.5390, 15.5390, 15.5390 \rangle$ and $|\boldsymbol{N}|$ is the magnitude of the normal of the die corner.

The power law model gives final gaps of 2.8879 mm and 42.942 mm at 10^{-3} s^{-1} and 2×10^{-3} s^{-1} for the same pressure applied. Longer forming times at the strain rates investigated are required for the power law model to finish forming the sheet into the rectangular die.

The final minimum thickness of Lin's model increased by 6.2% from 10^{-3} s^{-1} to 2×10^{-3} s^{-1}, and increased another 0.95% from 2×10^{-3} s^{-1} to 5×10^{-3} s^{-1}. Lin's model therefore does

not seem to be sensitive to an increase in strain rate.

The final minimum thickness of the tanh-model decreased by 2.6% from 10^{-3} s^{-1} to 2×10^{-3} s^{-1}, and decreased another 4.1% from 2×10^{-3} s^{-1} to 5×10^{-3} s^{-1}. The final minimum thickness results of the tanh-model is therefore sensitive to an increase in strain rate.

The SV-sinh model is the most sensitive to an increase in strain rate than the other material models investigated. The final minimum thickness decreased by 4.7%, 6.3% and 5.8% for set 1, set 2 and set 3 of the SV-sinh model from 10^{-3} s^{-1} to 2×10^{-3} s^{-1}, respectively. The final minimum thickness decreased by 10%, 12% and 11% for set 1, set 2 and set 3 of the SV-sinh model from 2×10^{-3} s^{-1} to 5×10^{-3} s^{-1}, respectively.

Table 3.5: Final minimum thickness results of the material models investigated at 10^{-3} s^{-1}, 2×10^{-3} s^{-1} and 5×10^{-3} s^{-1} for the formed box

Material model	$h_{f,min}$ at 10^{-3} s^{-1} [mm]	$h_{f,min}$ at 2×10^{-3} s^{-1} [mm]	$h_{f,min}$ at 5×10^{-3} s^{-1} [mm]
SV-sinh model, set 1	1.0078	0.9607	0.8646
SV-sinh model, set 2	1.0877	1.0187	0.8947
SV-sinh model, set 3	1.0380	0.9778	0.8696
Power law model	1.1703	1.2165	1.4436
tanh-model	1.1438	1.1143	1.0690
Lin's model	1.0252	1.0934	1.1039

Table 3.6: Final gap results of the material models investigated at 10^{-3} s^{-1}, 2×10^{-3} s^{-1} and 5×10^{-3} s^{-1} for the formed box

Material model	g_f at 10^{-3} s^{-1} [mm]	g_f at 2×10^{-3} s^{-1} [mm]	g_f at 5×10^{-3} s^{-1} [mm]
SV-sinh model, set 1	-0.68318	-0.30911	0.13955
SV-sinh model, set 2	-0.74738	-0.11668	0.018995
SV-sinh model, set 3	-0.72885	-0.30732	0.24832
Power law model	-0.67261	2.8879	42.942
tanh-model	-0.63901	-0.22892	8.5555
Lin's model	-0.40443	-0.28943	-0.68272

3.6 CONCLUSION

Four material models were investigated: the power law model, a tanh model, a sinh model by Lin, and Lin's sinh model with a more flexible grain size model (denoted as the SV-sinh model). The power law model did not exhibit increased localised thinning with increasing strain rate unlike the other material models investigated. The SV-sinh model showed the greatest thinning with increasing strain rate for the finite element models investigated. The SV-sinh model is selected for the optimisation of the pressure profiles in superplastic forming.

Three sets of the SV-sinh model were investigated. Set 1 fitted the stress-strain data the best, set 2 fitted the strain rate sensitivity-strain the best, and set 3 aimed to balance the fit of the stress-strain data and strain rate sensitivity-strain data. The thickness results of the three sets did not differ significantly for either the tensile test of superplastic forming of a rectangular box for the same pressure. The models with set 1, 2 and 3 all finished with a had a gap between the die corner and the sheet close to zero. The material parameters of set 3 of the SV-sinh model are selected for the optimisation of the pressure profiles in superplastic forming.

CHAPTER 4

OPTIMISING PRESSURE PROFILES IN SUPERPLASTIC FORMING

4.1 INTRODUCTION

The pressure profile of a superplastic forming process is a function of time. A larger pressure typically leads to a faster forming rate at the risk of inducing localised thinning. Hence, there is a trade-off between decreasing the forming time and retaining some minimum thickness. The goal of this chapter is to optimise the pressure profiles of the superplastic forming of a rectangular box such that the forming time is minimised and the final minimum thickness is limited.

4.2 BACKGROUND

An approximate optimisation strategy instead of an adaptive optimisation strategy is used to minimise the forming time. Background on the optimisation strategy used in this study is discussed in the following section.

4.2.1 Optimisation of metal forming processes

Optimisation strategies that have previously been used to solve metal forming optimisation problems before include [31]:

- Iterative optimisation strategies

- Adaptive optimisation strategies
- Optimisation strategies inspired by nature
- Approximate strategies

Iterative and adaptive optimisation strategies have been discussed in Chapter 3. Iterative optimisation strategies require sensitivities that are readily available. Optimisation strategies based on machine learning require many function evaluations or finite element simulations. These strategies have been used for metal forming optimisation problems despite their disadvantages [31].

Adaptive optimisation strategies are usually incorporated into finite element codes. The design variables are changed such that the objective function does not exceed an allowable value. Only one finite element model is required for this optimisation strategy which makes this strategy computationally efficient. Usually only time-dependent variables can be optimised this way. Access to the source code of the finite element package is usually required to implement adaptive optimisation strategies. An example of an adaptive optimisation strategy is the autopress routine in Abaqus which is described in Chapter 3. A number of authors have used an adaptive optimisation strategy to optimise superplastic forming processes [5, 6, 7].

Approximate optimisation strategies involve optimising metamodels and therefore does not have a direct connection to the finite element model [31]. The optimum of a metamodel is an approximation of the actual optimum since the metamodel is an approximation of the results of finite element models. Metamodel validation and sequential improvement is therefore important to ensure that the optimum of the metamodel is a good approximation of the real optimum.

Advantages of approximate optimisation strategies include the tendency to find the global optimum, applicability to parallel computing, efficient sensitivity evaluation, insensitivity to the finite element code used, and not being limited to only optimisation purposes [28]. The optimisation of metamodels is not as computationally expensive as the optimisation of a complex finite element model where each function evaluation requires solving a finite element model. An approximate optimisation strategy is used in this study to optimise the pressure

profiles in superplastic forming.

4.2.2 An approximate optimisation strategy

A diagram of an approximate optimisation strategy is shown in Figure 4.1. Finite element analyses are done for each experiment of the Design Of Experiments (DOE). Each response of the finite element analysis is used to construct a metamodel. The metamodel is validated in order to check how well the metamodel fits the responses of the finite element models. An optimisation algorithm is then applied to the metamodels. The accuracy of the optimum is checked with a finite element model. Sequential improvement of the optimum can be done until the final result is satisfactory.

Different metamodelling techniques include [28]:

1. Response surface method
2. Design and Analysis of Computer Experiments (DACE)
3. Multivariate Adaptive Regression Splines (MARS)
4. Radial Basis Function (RBF)
5. Neural nets
6. Support vector regression

Jin *et al.* [36] compared the response surface method, DACE method with Kriging, the RBF method, and the MARS method. Jin *et al.* [36] used fourteen test problems where the order of nonlinearity, problem size and sample size are varied. They found that the RBF method was the best metamodelling technique in terms of accuracy and robustness for large and small scale problems with a high degree of nonlinearity, and for large scale, highly nonlinear problems with scarce sample sets. The DACE method with Kriging performed the best for large scale problems with a low degree of nonlinearity. The response surface method performed the best for small scale, low order nonlinear problems. The MARS method performed the best for large scale, highly nonlinear problems of large and small sample sizes. The MARS method cannot accommodate scarce sample sets. Jin *et al.* [36] found that the

RBF method performed overall the best in terms of accuracy and robustness in comparison to the other methods.

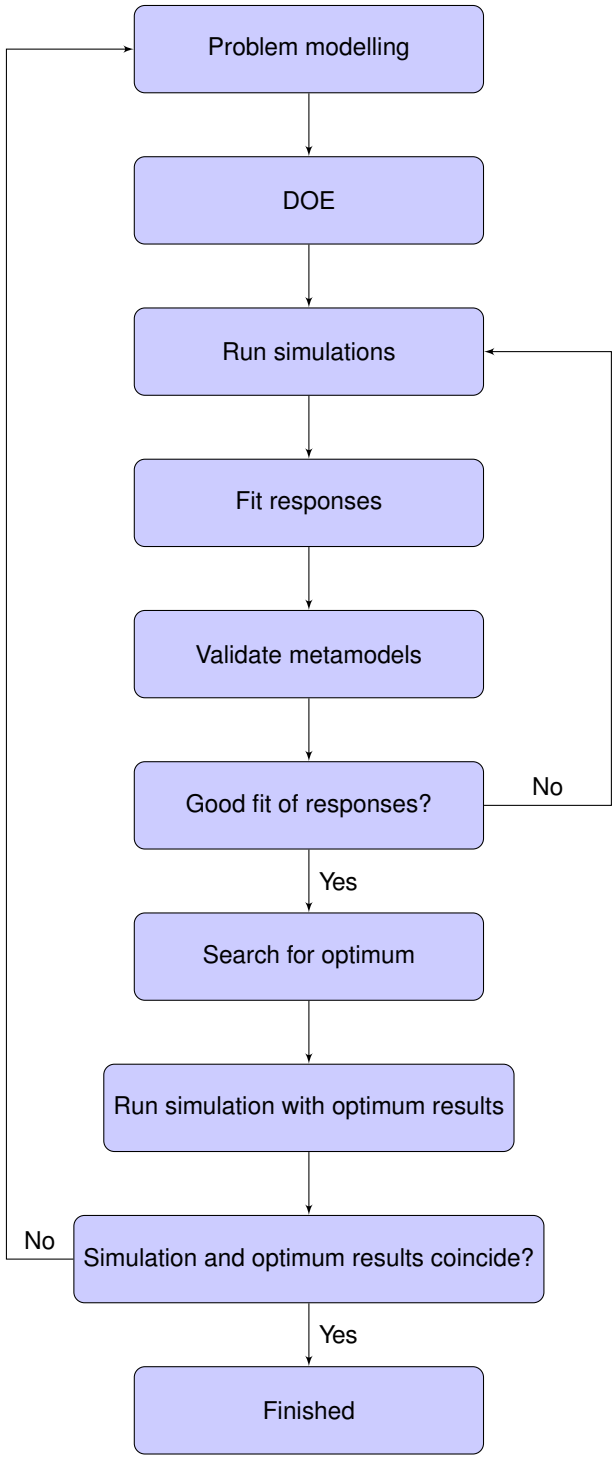

Figure 4.1: An approximate optimisation algorithm

The RBF method is used in this study. This method can interpolate response data, or it can be used as a regressive method. The metamodel obtained with the RBF method is given by

$$f(x) = \sum_{i=1}^{n} \omega_i \phi \left(\|x - x_i\| \right) \ , \tag{4.1}$$

where ω_i are coefficients that have to be determined and x_i are the n design points. $\|x - x_i\|$ is the Euclidean norm or radius. The Gaussian RBF is usually used

$$\phi(\|x - x_i\|) = \mathrm{e}^{-(\lambda \|x - x_i\|)^2} \ , \tag{4.2}$$

where λ is a constant [30].

4.2.3 Design of experiments

The number of DOE points is selected such that it is large enough to fit an accurate metamodel, but small enough to save time on the number of finite element analyses. The DOE depends on the metamodelling technique. Three properties that a DOE should have for interpolating and regressive metamodelling techniques are given in Table 4.1.

Geometry based DOE strategies have the properties that interpolating metamodelling techniques require. Statistically based DOE strategies have the properties that regressive metamodelling methods require [31]. Statistically based DOE strategies can also be used for interpolating metamodelling techniques. It has however been found that geometry based DOE strategies is more accurate and have more uniform projection properties than statistically based DOE strategies [28].

An example of a geometry based DOE strategy is the latin hypercube design. A latin hypercube design has one random design point per stratum per dimension as shown in Figure 4.2. A latin hypercube design has good projection properties which makes this DOE strategy suitable for screening purposes. If the significance of some dimensions are unknown at the beginning, all designs in those dimensions can be omitted. The experiments can then be projected onto the omitted dimensions after running the experiments [28].

Table 4.1: DOE properties related to different metamodelling techniques [28]

	Metamodelling techniques	
DOE property	**Interpolating**	**Regressive**
Goodness of fit	Space-filling design	The metamodel is assumed to have the same shape as the true response and DOE points should be taken on the boundary of the design space to minimise the variance of the regression coefficients.
Test for lack of fit and estimation of the pure error	Not applicable, because the shape of the metamodel is not presumed and there is no random error present. If there is an error present, it is a bias error. There are no replicate runs in computer experiments.	If there are replicate runs available, blocking and randomisation should be used to avoid the influence of nuisance variables.
Cost-effectiveness	Sequential experimentation can be done by adding design points sequentially using an expected metamodel improvement measure.	Saturated design, or sequential experimentation by increasing the order of the response surface that is fitted.

The distance between design points can be optimised instead of dividing the design space into strata. Distance-based designs include minimax and maximin designs. The minimax design is the minimisation of the maximum distance between each design point and their nearest neighbours, whereas the maximin design is the maximisation of the minimum distance between each design point and their nearest neighbours. The goal of the maximin design is to make sure that design points are not too close together, whereas the goal of the minimax design is to prevent holes in the design [28].

These DOE strategies may sometimes result in a design that is not space-filling. It is recommended to combine DOE strategies in order to avoid this problem. A latin hypercube design can for example be combined with a maximin design which will result in a more robust space-filling DOE [28, 37]. Latin hypercube designs with maximin are used in this study.

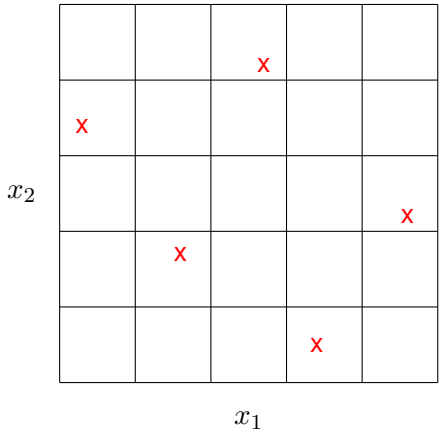

Figure 4.2: Latin hypercube DOE

An example of a statistically-based DOE strategy is factorial design. Full factorial design requires n^k experiments where n is the number of levels and k is the number of design variables. An example of a $n = 6$ and $k = 2$ full factorial design is shown in Figure 4.3. It can be observed that this DOE strategy is very expensive in comparison to the latin hypercube design.

A 2^k full factorial design is applicable to linear and interaction metamodels, but more levels are required for second order metamodels [28]. A full factorial design of $n = 11$ and $k = 2$ is used in this study. Refer to Section 4.3 for more information.

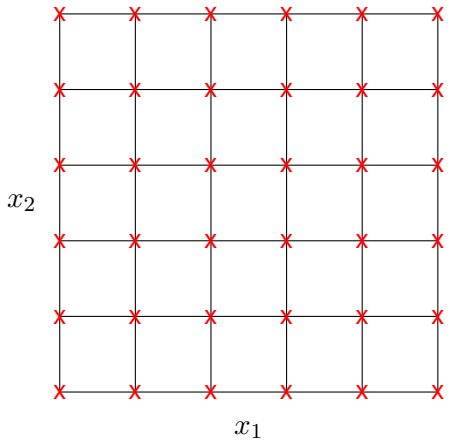

Figure 4.3: A full factorial design with $n = 6$ and $k = 2$

4.2.4 Metamodel validation

Metamodel validation involves testing the assumptions and accuracy of a metamodel. The accuracy of interpolating metamodels can be validated by means of assessing random validation points or with the method of cross-validation [28, 30, 37].

The first method requires comparing the response of the model at random design points that were not included in the DOE and comparing it to the metamodel's predicted results. This is not an attractive method since it requires the evaluation of extra experiments. The second method requires leaving out one i-th result (y_i) of the $\boldsymbol{y}_i$ measurements and fitting a metamodel through the remaining $\boldsymbol{y}_{-i}$ measurements. The Root Mean Square Error (RMSE) of the omitted result y_i and the predicted result $\hat{y}_{-i}$ is then calculated. This method is also called the Leave-One-Out Cross-Validation (LOOCV) method. The RMSE of the LOOCV method is given by

$$\text{RMSE} = \sqrt{\frac{\sum_{i=1}^{n} \left(y_i - \hat{y}_{-i}\right)^2}{n}}. \tag{4.3}$$

The cross-validation errors can be plotted against the predicted results $\hat{y}_{-i}$ in order to find the fit which gives the minimum cross-validation error.

4.2.5 Constrained optimisation

The optimisation algorithm can be applied after the best possible metamodel is fitted to the results. Evaluating metamodels are time-efficient and this property enables the use of adaptive search algorithms that require many function evaluations, or iterative optimisation algorithms with multi-start. These algorithms tend to find the global minima of nonlinear metamodels.

The iterative optimisation algorithm sequential quadratic programming with multi-start is used in this study. This method is explained by Arora [25]. This algorithm is available in Matlab as *fmincon*.

4.2.6 Sequential improvement

The metamodel's accuracy or the prediction of the global optimum can be sequentially improved, if the initial optimum found with the approximate optimisation strategy is unsatisfactory, or if the finite element model with the optimised design variables delivers results that are different from the optimum found with the approximate optimisation strategy.

The unsatisfactory optimum gives an initial indication where the true optimum can be found in the design space. The design space can be decreased in size (zooming) or moved to the expected position of the optimum (panning). Design points are resampled at the new position. The method of zooming in on the optimum can be done by decreasing the design space by a factor, or by excluding less important design variables, or with visual reasoning. Zooming for minimisation problems can be done by limiting the significant design variables to those points whose objective function value minus metamodel error is smaller than the optimum value plus the error of the optimum [28].

An accurate metamodel usually leads to a more accurate determination of the optimum solution. The global optimum can be improved directly by minimising a merit function, or with the method of maximum expected improvement [28].

4.3 OPTIMISATION PROBLEM FORMULATION

The objective is to minimise the final forming time t_f of the superplastic forming of a rectangular box subject to the final gap g_f between the die corner and sheet being less than or equal to an allowable maximum final gap value $g_{f,max}$, and the final sheet thickness h_f being greater than or equal to an allowable minimum final sheet thickness value $h_{f,min}$. The gap g is calculated according to Eq. (3.59). The finite element model of the superplastic forming of a rectangular box has been discussed in Chapter 3.

The actual final forming time does not necessarily match the final time of the pressure-time curve when a pressure-time curve is prescribed for a superplastic forming simulation. It is conceivable that the forming process is complete (sheet deformation stops due to full contact between the sheet and the die) before the final time of the pressure-time curve is reached.

It is also possible that the final pressure is inadequate to complete the forming process, in which case a gap remains between the deformable sheet and the die after the simulation is complete. The forming time is therefore estimated by post-processing the displaced geometry data after a simulation is completed.

The coordinates of the nodes on the bottom surface of the forming sheet are recorded every 10 s, and linear interpolation is used to interpolate between every data point. The estimated forming time is calculated as the time required for the maximum gap between the sheet and the die to reduce to less than $g_{\mathrm{f,max}}$. This method is illustrated graphically in Figure 4.4.

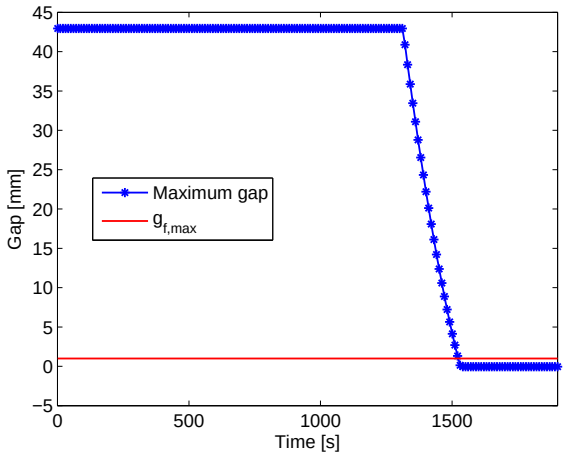

Figure 4.4: Illustration of how the final forming time is calculated

The final forming time is controlled by the pressure applied to the sheet. The pressure-time curve is described with two design variables in order to demonstrate the optimisation technique. The use of two design variables also allows for easy visualisation in order to verify that the optimisation problem formulation and solution are reasonable. The drawback of a two dimensional parametrisation of the pressure-time curve is that the user has no control over the shape of the pressure-time curve. The shape of the pressure-time curve is determined by the master curve.

The two dimensional optimisation problem investigated has $\boldsymbol{x} = \{\, x_1 \; x_2 \,\}$ where x_1 scales the time of a master pressure-time curve and x_2 scales the pressure of a master pressure-time curve. The master curve is a smooth curve fitted to the pressure calculated with the autopress

routine. The master curve is given by

$$p = 51.738\left(1 - \mathrm{e}^{-0.0049633t}\right) - 0.22417\mathrm{e}^{0.0042733t} \ . \tag{4.4}$$

Recall that the autopress routine changes the pressure such that a target strain rate is maintained in the forming sheet. The target strain rate is chosen as 10^{-3} s^{-1}. The master curve and the pressure calculated with the autopress routine are shown in Figure 4.5. A hundred discrete points along the pressure-time curve are used to describe the pressure in the Abaqus input file.

Regarding the choice of material models, the SV-sinh model has been demonstrated to be the most sensitive to an increase in forming rate. The SV-sinh model is therefore selected, using the set 3 material parameters, to perform all the simulations in this chapter. This should result in a conservative estimate of the final thickness, as compared to results obtained when using the other material models.

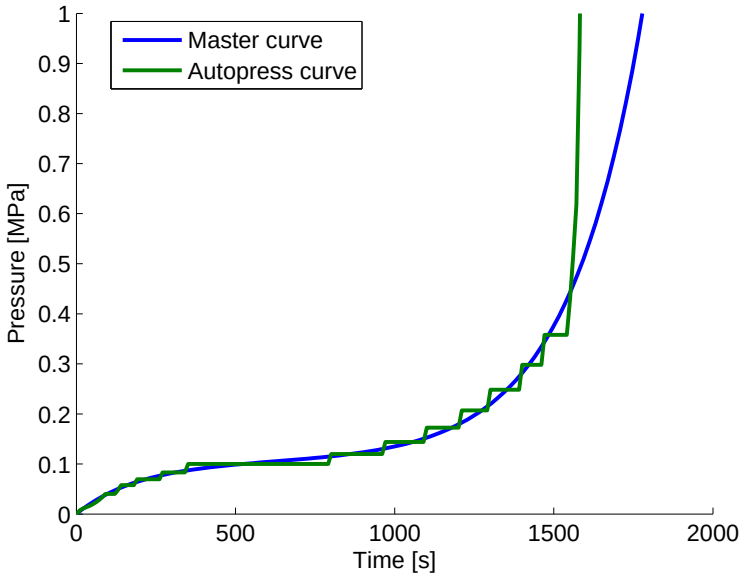

Figure 4.5: Master curve and autopress curve at 10^{-3} s^{-1} for set 3 of the SV-sinh model

A full factorial design of 11 × 11 finite element analyses is used for this two dimensional optimisation problem. This DOE is selected primarily to facilitate easier visualisation of the design functions namely forming time and minimum thickness. The final forming time results are used to construct the cost function or cost metamodel. The minimum thickness

results are used to construct the optimisation constraint function or constraint metamodel. The lower bounds of the design variables are $\mathbf{lb} = \{\, 0.4 \; 0.4 \,\}$. The upper bounds of the design variables are $\mathbf{ub} = \{\, 1 \; 2.4 \,\}$.

The RBF method is used to construct the metamodels. Interpolating and regressive RBF methods are investigated in this study. The number of data points is 121 and the length of $\boldsymbol{\omega}$ in Eq. (4.1) is selected as 50 for the regressive RBF method. The 50 points are selected using a combined latin hypercube and maximin sampling method. The optimum from the regressive RBF metamodels is dependent on the sampling method. Fifty different samples of 50 points each were evaluated in order to quantify the distribution of the optimum solution.

The LOOCV method is used to validate the interpolating RBF metamodels. The regressive RBF metamodels are validated by minimising the RMSE. The λ-value in Eq. (4.2) with the smallest RMSE is used to construct the metamodel. The λ-values investigated are limited to values between 10^{-1} and 0.2 in order to prevent overfitting.

4.4 RESULTS

4.4.1 Finite element analyses

A surface plot of the final minimum gap of the finite element analyses is shown in Figure 4.6. Simulations with a final gap greater than $g_{\mathrm{f,max}}$ indicate that the forming process is not complete, and they are excluded from the metamodel construction. The presented gap results are smaller than $g_{\mathrm{f,max}} = 1$ mm, and therefore all of the finite element results were used for metamodel construction. Negative gap values indicate mesh penetration.

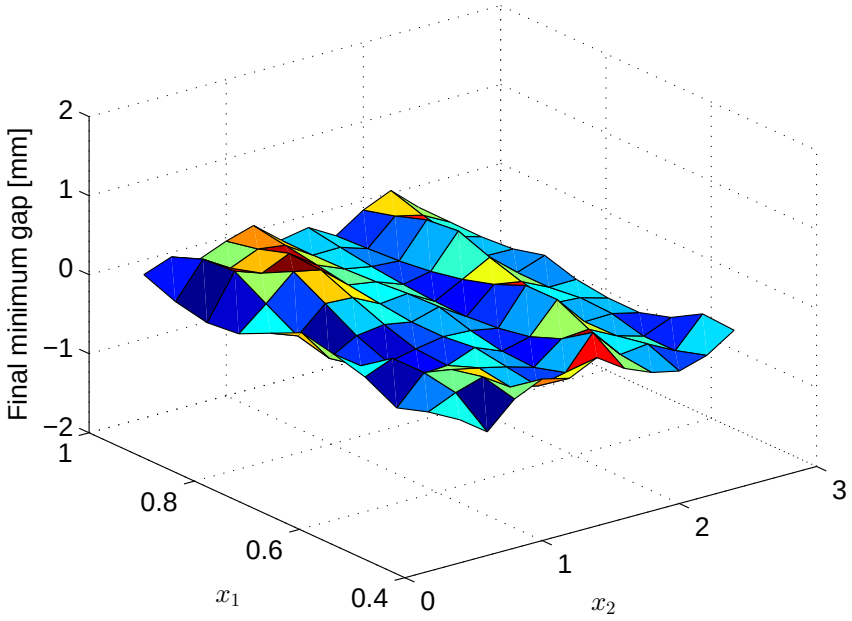

Figure 4.6: Surface plot of the final gap finite element results

Surface plots of the final minimum thickness and final forming time of the finite element analyses are given in Figures 4.7 and 4.8, respectively. The final thickness results are not as smooth as typical computer experiments. This may be due to the finite element method of the superplastic forming process being a path dependant due to plasticity and contact.

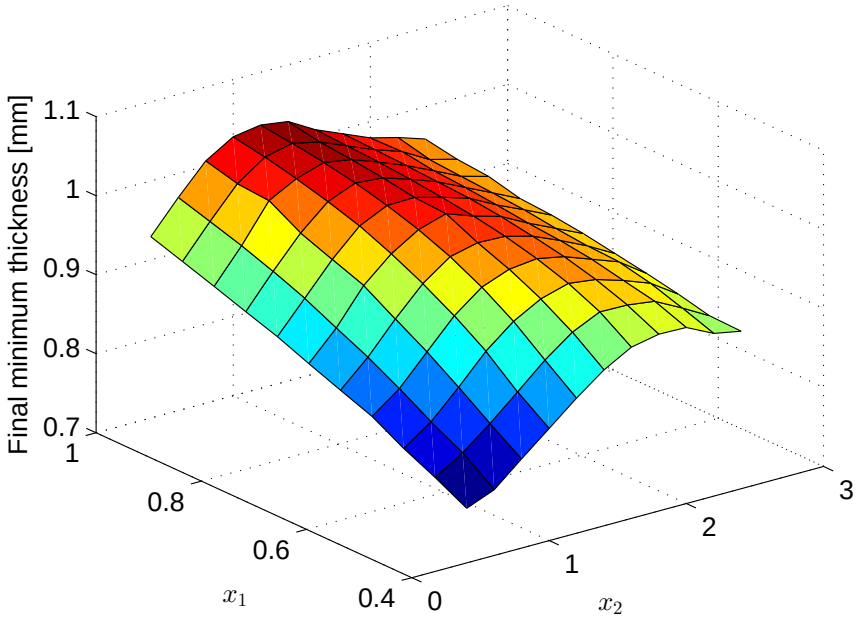

Figure 4.7: Surface plot of the final minimum thickness finite element results

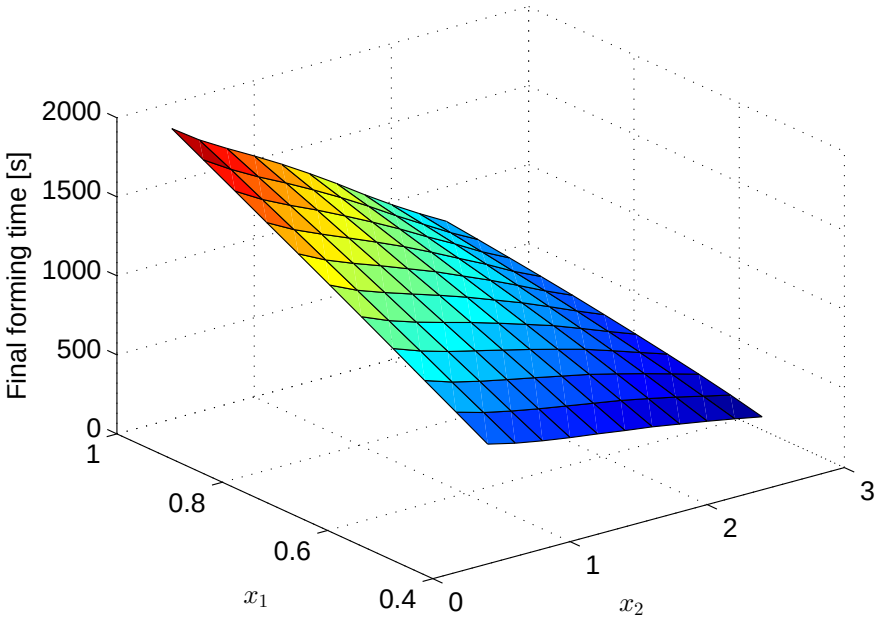

Figure 4.8: Surface plot of the final forming time finite element results

A contour plot of the final minimum thickness and final forming time of the finite element analyses are given in Figure 4.9. The contour plot verifies that the optimisation problem formulation is sound, and it provides a good starting point for the two dimensional optimisation algorithm. The starting point is selected as $\boldsymbol{x}_0 = \{\, 0.7 \;\; 1.3 \,\}$ for $h_{\text{f,min}} = 1$ mm and $g_{\text{f,max}} = 1$ mm.

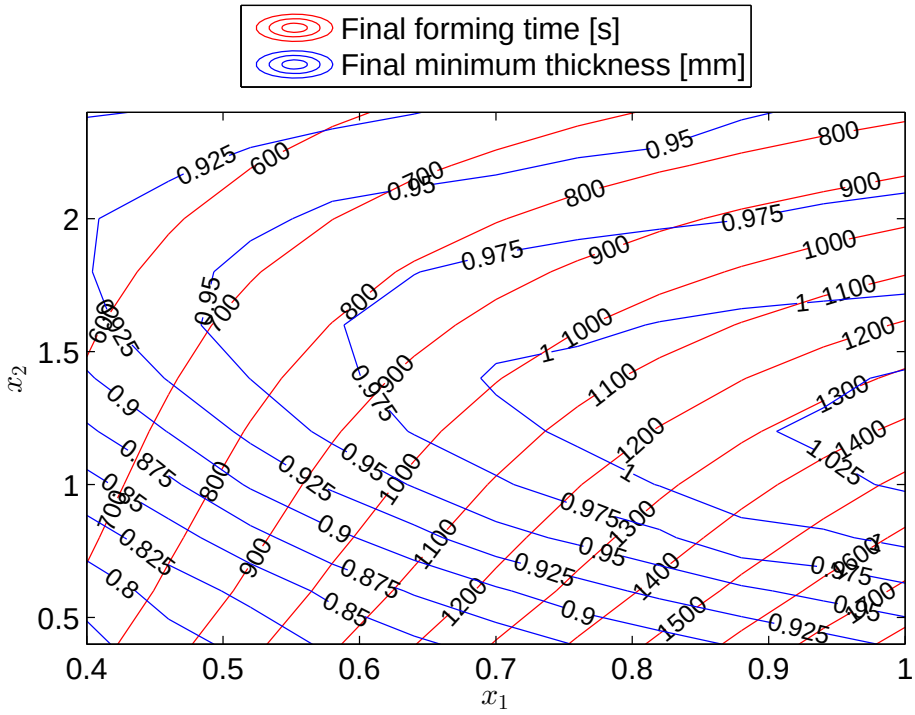

Figure 4.9: Contour plot of the final minimum thickness and final forming time finite element results

4.4.2 Metamodels

The RMSE is plotted against λ for the interpolating RBF metamodels in Figure 4.10. The λ-value for the final minimum thickness interpolating RBF is 5.7224. Its corresponding RMSE-value is 0.0119. The λ-value for the final forming time interpolating RBF is 5.214. Its corresponding RMSE-value is 0.26346.

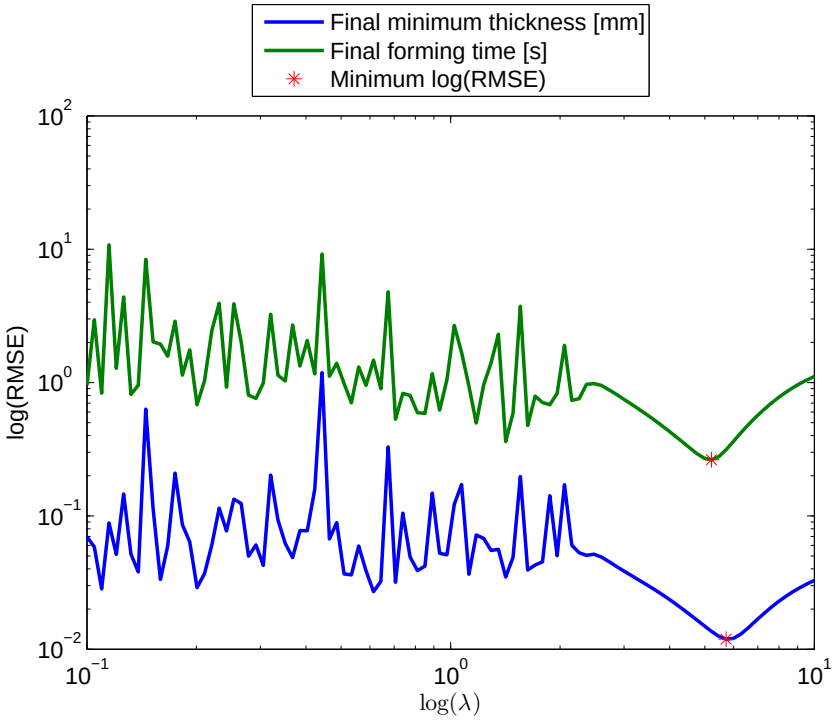

Figure 4.10: RMSE versus λ for the interpolating RBF metamodels

The RMSE is plotted against λ for one of the fifty samplings of the regressive RBF metamodels in Figure 4.11. The mean, minimum and maximum RMSE and λ-values of the regressive RBF metamodels for the fifty samplings are given in Table 4.2. The mean λ-value of the final thickness h_f regressive RBF metamodel differs by 73% from the λ-value of the final thickness interpolating RBF metamodel. The mean λ-value of the final forming time t_f regressive RBF metamodel differs by 71% from the λ-value of the final forming time interpolating RBF metamodel.

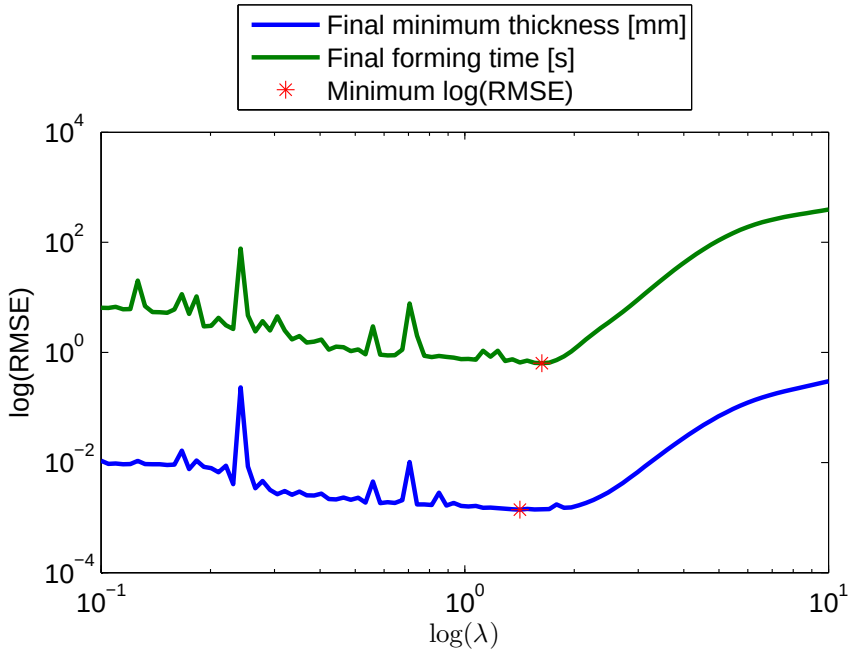

Figure 4.11: RMSE versus λ for the regressive RBF metamodels

Table 4.2: Mean, minimum and maximum RMSE and λ-values for the regressive RBF metamodels

RBF	RMSE_{min}	$\text{RMSE}_{\text{mean}}$	RMSE_{max}	λ_{min}	λ_{mean}	λ_{max}
h_{f}, regressive	1.2318×10^{-3}	1.3217×10^{-3}	1.4741×10^{-3}	1.4175	1.5352	1.5849
t_{f}, regressive	5.6377×10^{-1}	6.1463×10^{-1}	6.6910×10^{-1}	1.1989	1.5172	1.5849

The contour plots of the final minimum thickness and final forming time of the interpolating RBF metamodels are given in Figure 4.12. The contours of the metamodels are jagged at the lowest and highest values of x_2 making the function values unreliable there. This is due to high λ-values.

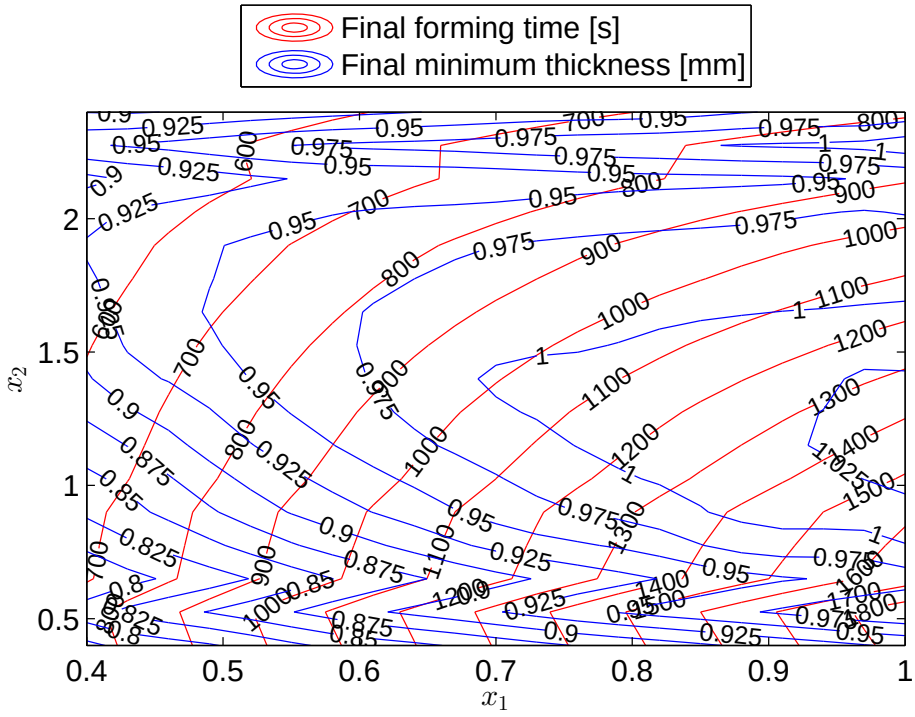

Figure 4.12: Contour plots of the final minimum thickness and final forming time interpolating RBF metamodels

The contour plots of the final minimum thickness and final forming time of regressive RBF metamodels for one latin hypercube design are given in Figure 4.13. The contours of the metamodels are smoother than for the interpolating RBF metamodels. This is due to lower values of λ.

The contour plots of the final minimum thickness and final forming time for the fifty different samplings of the regressive RBF metamodels are given in Figure 4.14. The regressive RBF metamodels are slightly different for each of the 50 samplings. The largest difference can be observed at the lowest and highest values of x_2, but the contour plots of the regressive RBF metamodels are smoother than that of the interpolating RBF metamodels at these values. The regressive RBF metamodels are used for the optimisation of the final forming time further in this study.

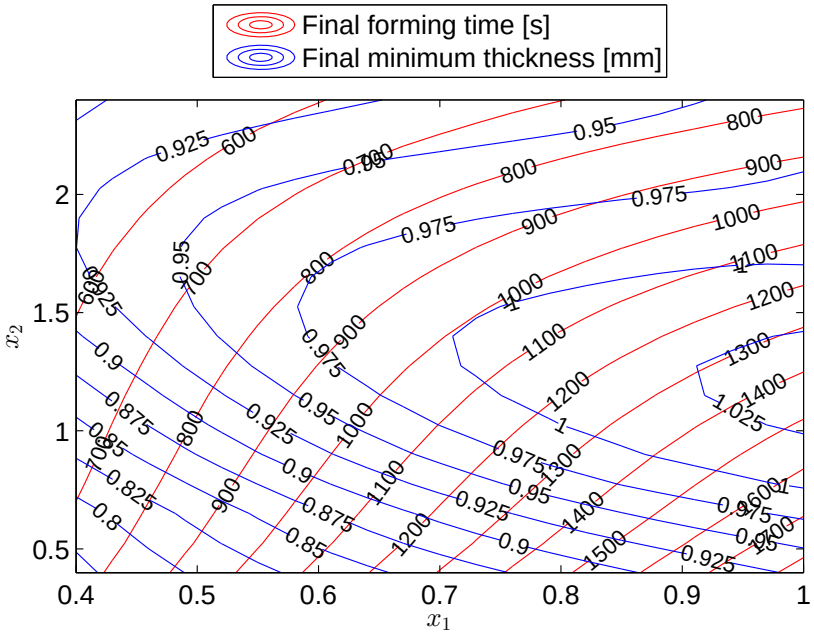

Figure 4.13: Contour plots of the final minimum thickness and final forming time regressive RBF metamodels

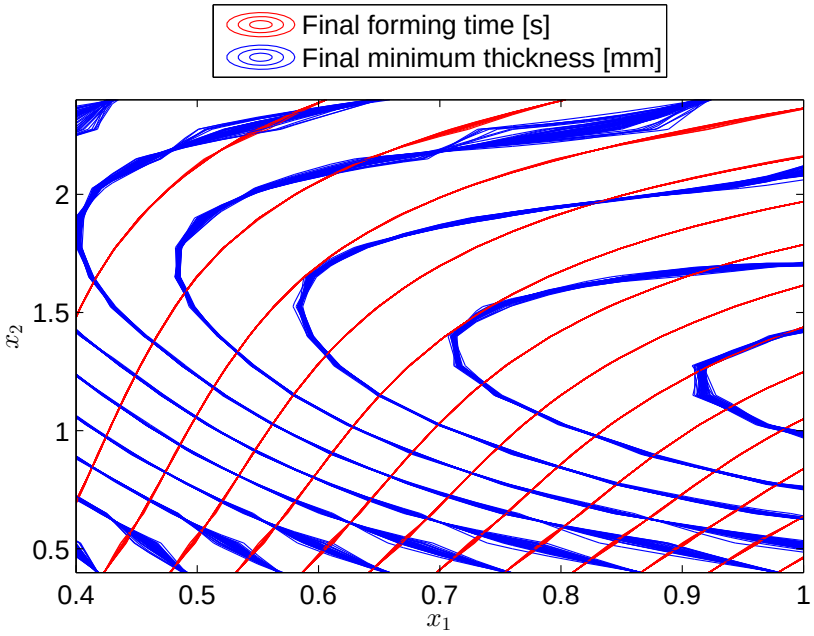

Figure 4.14: Contour plots of the 50 final minimum thickness and final forming time regressive RBF metamodels

4.4.3 Optimum

The optimisation problem is solved for $h_{\text{f,min}} = 1$ mm, 0.975 mm and 0.96 mm. This approach quantifies the trade-off between forming time and minimum thickness. The availability of cheap-to-evaluate metamodels allows such an investigation where changing design constraints and resolving for the optimum is now tractable. Constructing multiple metamodels are also tractable, with all the finite element analyses run off-line before the optimisation proceeds.

The optimum solutions for the fifty different samplings are shown as green stars in Figure 4.15. The solutions are clustered relatively close together.

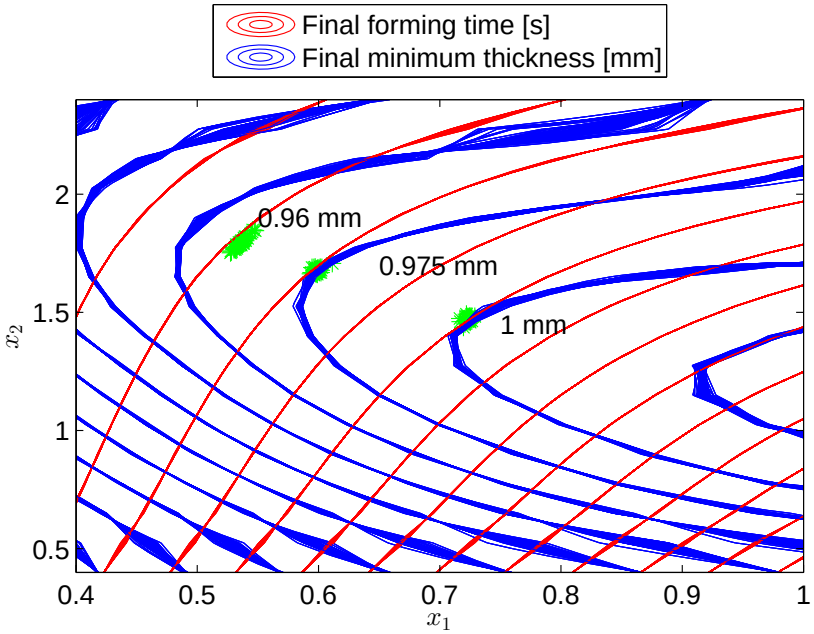

Figure 4.15: Contour plot of the optimum solutions of the fifty different latin hypercube designs

The distribution of the optimum solutions for $h_{\text{f,min}} = 1$ mm, 0.975 mm and 0.96 mm are given in Figures 4.17, 4.18 and 4.19, respectively. The optimum solutions with the highest frequency are given in Table 4.3. The average violation of the optimum solutions from $h_{\text{f,min}}$ is also given in Table 4.3. It can be observed that the final forming time decreases as the

pressure scale increases.

Table 4.3: Optimum solutions of the three minimum final thickness investigated

$h_{\text{f,min}}$ [mm]	$x_{1,\text{opt}}$ (time scaling)	$x_{2,\text{opt}}$ (pressure scaling)	$t_{f,\text{opt}}$ [s]	Average final thickness constraint violation [mm]
1	0.72457	1.4782	998.89	1.1174×10^{-4}
0.975	0.5997	1.6816	805.44	3.3097×10^{-7}
0.96	0.53867	1.8054	710.75	2.6008×10^{-7}

The optimum pressure-time curves are constructed from the optimum design variables with the highest frequency. The optimum pressure-time curves for $h_{\text{f,min}} = 1$ mm, 0.975 mm and 0.96 mm are compared to the master curve in Figure 4.16. The final forming times of the curves are given by the dashed lines. The minimum final thickness of the master curve is 1.0277 mm, and the final forming time of the master curve is 1523.7 s. The difference between the final minimum thickness of 1.0277 mm and 1 mm is 2.7%, but the difference between the final forming times is 38%. There is therefore big gains in time for a small reduction in final minimum thickness.

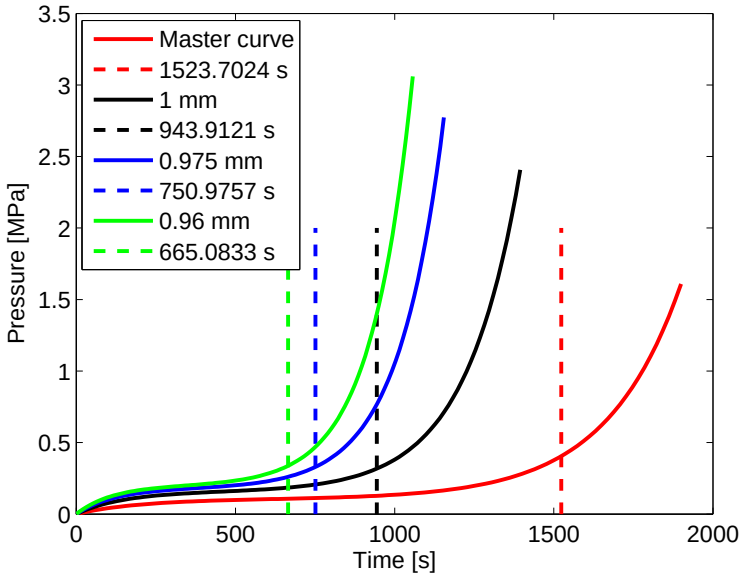

Figure 4.16: Optimum pressure curves compared to the master curve

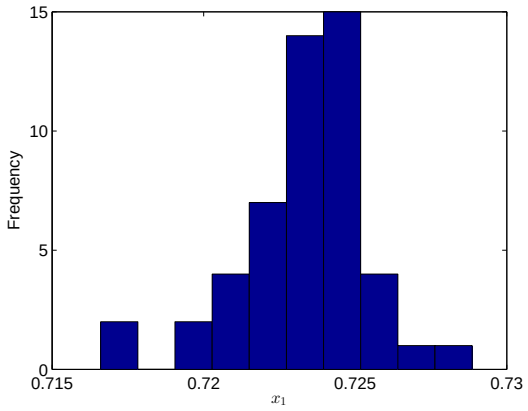

(a)

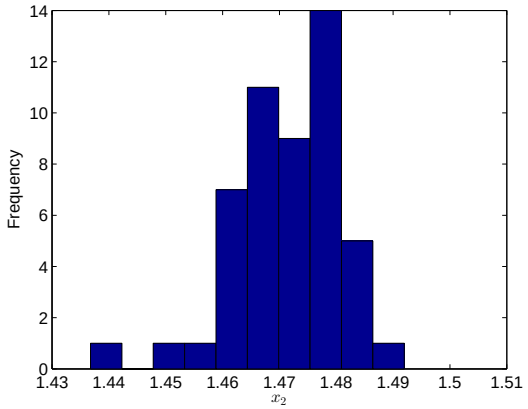

(b)

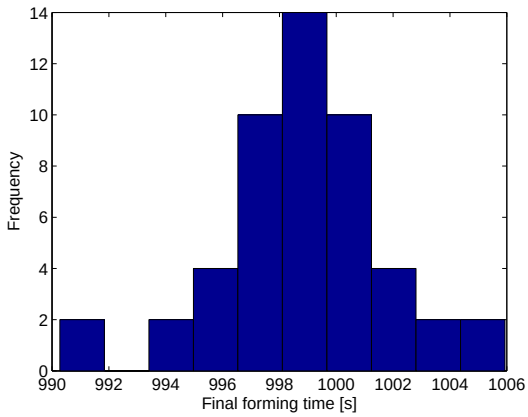

(c)

Figure 4.17: The optimum (a) x_1, (b) x_2 and (c) final forming time distributions for $h_{\text{f,min}} = 1$ mm

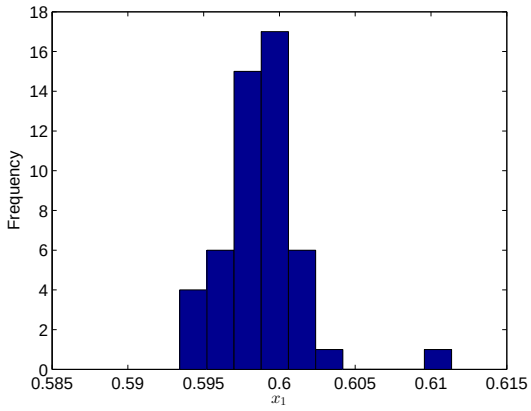

(a)

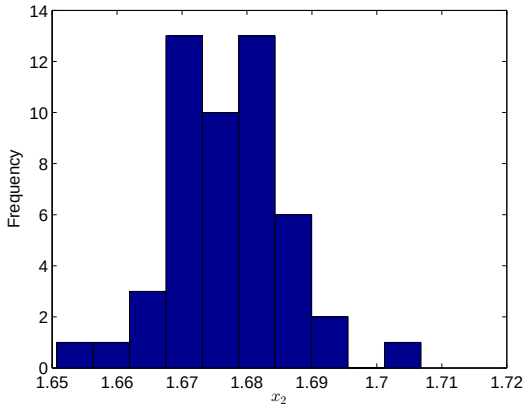

(b)

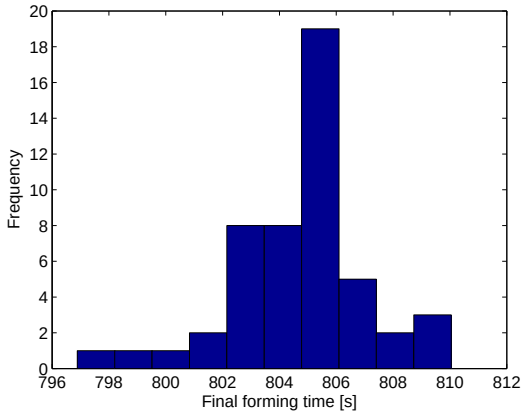

(c)

Figure 4.18: The optimum (a) x_1, (b) x_2 and (c) final forming time distributions for $h_{\text{f,min}} = 0.975$ mm

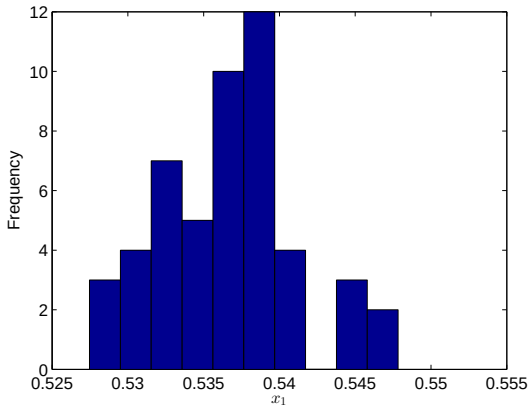

(a)

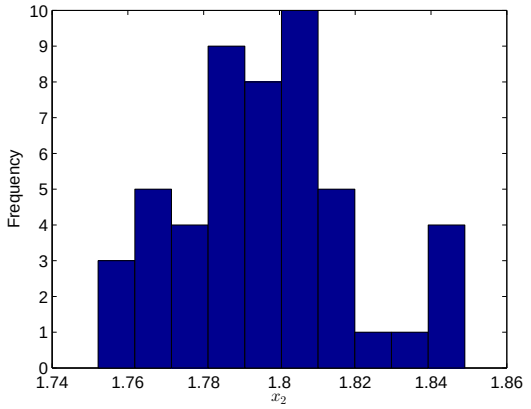

(b)

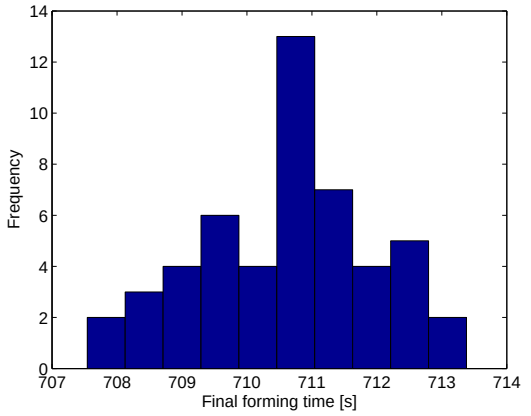

(c)

Figure 4.19: The optimum (a) x_1, (b) x_2 and (c) final forming time distributions for $h_{\mathrm{f,min}} = 0.96$ mm

The optimum solutions with the highest frequency are verified using the Finite Element Method (FEM). The finite element results for $h_{\text{f,min}} = 1$ mm, 0.975 mm and 0.96 mm are compared to the optimisation results in Table 4.4. The gap for the three optimum solutions are less than 1 mm. The final thickness of the finite element results $h_{\text{f,FEM}}$ differs by -0.21%, 0.16% and -0.02% from the optimum final thickness results for $h_{\text{f,min}} = 1$ mm, 0.975 mm and 0.96 mm, respectively. The final forming time of the finite element results $t_{\text{f,FEM}}$ differs by 0.11%, 0.13% and 0.07% from the optimum final forming time results for $h_{\text{f,min}} = 1$ mm, 0.975 mm and 0.96 mm, respectively. There is therefore no need to apply sequential improvement to the metamodels or optimum results.

The solutions are nonetheless encouraging. The metamodels predicted that allowing a 4% decrease in the minimum allowable thickness (1.0 mm to 0.96 mm) and a maximum gap of 1 mm between the sheet and the die, the forming time decreased by 28.84%. The finite element verification indicates that the final minimum thickness reduced by 3.8%, resulting in the forming time being reduced by 28.81%. The approximate optimisation strategy is more flexible than solving the pressure using the autopress routine where the user has no direct control over the minimum allowable thickness, and only the target strain rate can be specified. An increased target strain rate would reduce the forming time by applying a higher pressure, and the minimum thickness can only be reported after completing the forming simulation.

Table 4.4: Finite element results for the optimum solutions for $h_{\text{f,min}} = 1.0$ mm, 0.975 mm and 0.96 mm

$h_{\text{f,min}}$ **[mm]**	$h_{\text{f,min,FEM}}$ **[mm]**	$g_{\text{f,FEM}}$ **[mm]**	$t_{\text{f,FEM}}$ **[s]**	$t_{f,\text{opt}}$ **[s]**
1	0.99789	-0.26096	997.77	998.89
0.975	0.97659	-0.12575	804.42	805.44
0.96	0.95978	-0.02396	710.26	710.75

The final thickness results along the diagonal of the formed box for $h_{\text{f,min}} = 1.0$ mm, 0.975 mm and 0.96 mm are compared to the results of the master curve in Figure 4.20. The final minimum thickness is at the corner of the die. Recall that the final minimum thickness of the master curve is 1.0277 mm. The thickness at the centre of the die is 10% less for the $h_{\text{f,min}} = 0.96$ mm case than for the master curve.

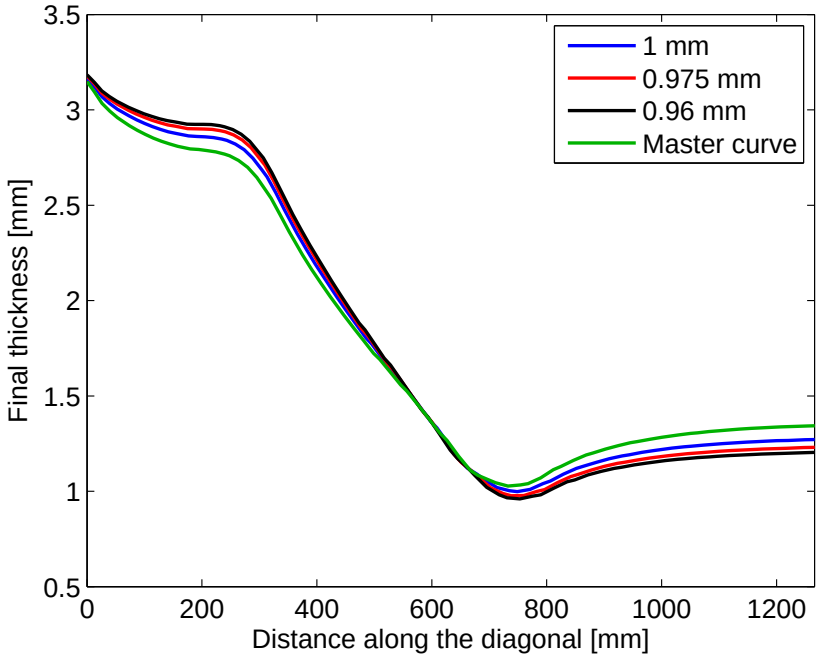

Figure 4.20: Final thickness results along the diagonal for the optimum solutions and the master curve

4.5 CONCLUSION

The final forming time of the superplastic forming of a rectangular box is successfully minimised while limiting the final minimum thickness. The metamodels predicted that allowing a 4% decrease in the minimum allowable thickness (1.0 mm to 0.96 mm) and a 1 mm gap between the sheet and the die corner the forming time is decreased by 28.84%. The finite element verification indicates that the final minimum thickness reduced by 3.8% and that the gap between the sheet and the die corner is less than 1 mm, resulting in the forming time being reduced by 28.81%.

The time savings on forming is bigger for the approximate optimisation strategy than for the Abaqus autopress routine which was used to compute the master curve. The minimum final thickness of the master curve is 1.0277 mm with a final forming time of 1523.7 s. The difference between the final minimum thickness of the master curve and the metamodel with a minimum allowable thickness of 1 mm is 2.7%, but the difference between the final forming times is 38%.

CHAPTER 5

CONCLUSION

5.1 SUMMARY OF FINDINGS

The objective of this study is to find a technique that can be used to minimise the forming time of a superplastic forming process while limiting the final minimum thickness. A finite element model of the superplastic forming of a rectangular box is used to demonstrate this technique.

The finite element model requires a material model that will show the correct behaviour at the higher strain rates of this forming method. Superplastic deformation changes from quasi-stable flow to localised thinning if a superplastic metal specimen is strained at the higher strain rates of this forming method. A material model that can show the onset of localised thinning at higher strain rates should be used to minimise the forming time of a superplastic forming process.

The strain rate sensitivity of four material models were compared. The material models are a simple power law model, a general tanh-model, a sinh-model by Lin [21], and Lin's model with a more flexible grain growth model, denoted as the SV-sinh model. Digitised data from Ghosh and Hamilton [15] for Ti-6Al-4V at three different initial grain sizes were used to calibrate the material models. The SV-sinh model was also calibrated with strain rate sensitivity-strain data, since the strain rate sensitivity affects the localised thinning of the material.

Three sets of different weights for the calibration of the SV-sinh model were investigated. Set 1 prioritises the stress-strain data, whereas set 2 prioritises the strain rate sensitivity-strain

data. Set 3 aims to balance the fit of the stress-strain data and strain rate sensitivity-strain data. The difference in final thickness results between the three sets of the SV-sinh model is insignificant.

The power law model does not show localised thinning with increasing strain rate. The SV-sinh model is the most sensitive to an increase in strain rate. The SV-sinh model is therefore selected to be used in the finite element model.

The minimisation of the final forming time is done with an approximate optimisation strategy. A metamodel is constructed using the responses of the finite element model. The metamodels are optimised instead of optimising one finite element model directly like with an adaptive optimisation strategy. The approximate optimisation strategy saves time in computation when different final minimum thickness constraints are investigated.

The forming time is minimised by manipulating the pressure-time curve which is applied to the forming sheet. The pressure-time curve is described with a master curve that is scalable in time and pressure. The master curve is a smoothed pressure-time curve calculated with the Abaqus autopress routine. The Abaqus autopress routine adjusts the applied pressure such that a target strain rate is maintained in the forming sheet.

The metamodels were constructed from the responses of 11×11 finite element models. One metamodel is constructed using the final forming time results. This metamodel is used as the objective function of the optimisation problem. Another metamodel is constructed using the final minimum thickness results. This metamodel is used as a constraint function. The metamodels were validated by minimising the root mean square error between the model and response values.

The radial basis function method was used to construct the metamodels. The regressive radial basis function metamodels proved to be more reliable at the design space boundaries than the interpolating radial basis function metamodels. The regressive radial basis function metamodels were therefore optimised in this study.

The number of response points is 121 and the length of $\boldsymbol{\omega}$ in Eq. (4.1) is selected as 50 for the regressive radial basis function metamodels. The metamodel points are sampled with a combined latin hypercubes and maximin sampling method. Fifty samplings were evaluated

in order to investigate the distribution of the optimum solution. The optimum solutions of the fifty samplings were clustered close together. The optimum solutions with the highest frequency were selected and verified using the finite element method. The difference between the results of the final finite element analysis and the optimum solution is insignificant, and sequential improvement the optimum solution is not required.

The final forming time of the superplastic forming of a rectangular box was successfully minimised. The approximate optimisation strategy showed that by allowing a 4% decrease in the minimum allowable thickness (1.0 to 0.96mm) and a 1 mm gap between the sheet and the die corner the forming time is decreased by 28.84%. The final forming time is reduced by 38% when the metamodel with an allowable minimum thickness of 1 mm is compared to the master curve finite element model which has a final minimum thickness of 1.0277 mm.

5.2 SUGGESTIONS FOR FUTURE RESEARCH

Future research can include

1. the effect of changing the shape of the pressure-time curve
2. calibrating the material model with the finite element method in the loop
3. the effect of friction between the sheet and die on the final thickness distribution
4. the effect of material cavitation and softening on the final thickness distribution
5. the effect of temperature on the forming process

The optimum obtained with this technique can be validated with real experiments for future research. Superplastic forming with different metals and alloys can also be investigated in the future.

REFERENCES

[1] G. J. Davies, J. W. Edington, C. P. Cutler, and K. A. Padmanabhan. Superplasticity: A Review. *Journal of Materials Science*, 5(12):1091–1102, 1970.

[2] X. Li and S. Soo. Numerical simulation and superplastic forming of Ti-6Al-4V alloy for a dental prosthesis. *Journal of Materials Engineering and Performance*, 20(3):341–347, 2011.

[3] T. G. Langdon. Fracture processes in superplastic flow. *Metal Science*, 16(4):175–183, 1982.

[4] A. K. Ghosh and C. H. Hamilton. Mechanical behavior and hardening characteristics of a superplastic Ti-6AI-4V alloy. *Metallurgical Transactions A*, 10(6):699–706, 1979.

[5] L. Carrino, G. Giuliano, and C. Palmieri. On the optimisation of superplastic forming processes by the finite-element method. In *Journal of Materials Processing Technology*, volume 143-144, pages 373–377, 2003.

[6] H. Sheikhalishahi and M. Farzin. A new approach for determining the optimum pressure-time diagram in superplastic forming process. *International Journal of Advanced Design and Manufacturing Technology*, 6(3):71–76, 2014.

[7] R. Hambli, A. Potiron, F. Guerin, and B. Dumon. Numerical pressure prediction algorithm of superplastic forming processes using 2D and 3D models. *Journal of Materials Processing Technology*, 112(1):83–90, 2001.

[8] P. S. Bate, N. Ridley, B. Zhang, and S. Dover. Optimisation of the superplastic forming of aluminium alloys. *Journal of Materials Processing Technology*, 177(1-3):91–94, 2006.

[9] M. A. Nazzal, M. K. Khraisheh, and B. M. Darras. Finite element modeling and optimization of superplastic forming using variable strain rate approach. *Journal of Materials Engineering and Performance*, 13(6):691–699, 2004.

[10] D Sorgente and L Tricarico. Pressure profile designing in superplastic forming based on the strain rate and on post-forming properties. *Journal of Materials Engineering and Performance*, 23:2025–2033, 2014.

[11] O. D. Sherby and J. Wadsworth. Superplasticity and superplastic forming processes. *Materials Science and Technology*, 1(11):925–936, 1985.

[12] T. G. Langdon. The physics of superplastic deformation. *Materials Science and Engineering: A*, 137:1–11, 1991.

[13] W. Stumpf. Creep Deformation at high temperatures. In *Mechanical Metallurgy NMM700*, chapter 4, pages 62–71. University of Pretoria, Pretoria, 2014.

[14] J. Hedworth and M. J. Stowell. The measurement of strain-rate sensitivity in superplastic alloys. *Journal of Materials Science*, 6(8):1061–1069, 1971.

[15] A. K. Ghosh and C. H. Hamilton. Influences of material parameters and microstructure on superplastic forming. *Metallurgical Transactions A*, 13(5):733–743, 1982.

[16] E. Alabort, D. Putman, and R.C. Reed. Superplasticity in Ti-6Al-4V: Characterisation, modelling and applications. *Acta Materialia*, 95:428–442, 2015.

[17] J. Bonet, A. Gil, R. D. Wood, R. Said, and R. V. Curtis. Simulating superplastic forming. *Computer Methods in Applied Mechanics and Engineering*, 195(48-49):6580–6603, 2006.

[18] A. J. Barnes. Superplastic Forming 40 Years and Still Growing. *Journal of Materials Engineering and Performance*, 22(10):2935–2949, 2007.

[19] N. Chandra, S. C. Rama, and Z. Chen. Critical issues in the industrial application of SPF-process modeling and design practices. *Materials Transactions, JIM*, 40(8):723–736, 1999.

[20] R. J. Nedoushan, M. Farzin, M. Mashayekhi, and D. Banabic. A microstructure-based

constitutive model for superplastic forming. *Metallurgical and Materials Transactions A*, 43(11):4266–4280, 2012.

[21] J. Lin. Selection of material models for predicting necking in superplastic forming. *International Journal of Plasticity*, 19(4):469–481, 2002.

[22] F. P. E. Dunne. Inhomogeneity of microstructure in superplasticity and its effect on ductility. *International Journal of Plasticity*, 14(4-5):413–433, 1998.

[23] M. A. Nazzal, M. K. Khraisheh, and F. K. Abu-Farha. The effect of strain rate sensitivity evolution on deformation stability during superplastic forming. *Journal of Materials Processing Technology*, 191(1-3):189–192, 2007.

[24] F. K. Abu-Farha and M. K. Khraisheh. On the high temperature testing of superplastic materials. *Journal of Materials Engineering and Performance*, 16:142–149, 2007.

[25] J. S. Arora. *Introduction to Optimum Design*. Academic Press, third edition, 2012.

[26] J. Lin and J. Yang. GA-based multiple objective optimisation for determining viscoplastic constitutive equations for superplastic alloys. *International Journal of Plasticity*, 15(11):1181–1196, 1999.

[27] A. P. Engelbrecht. Optimisation Theory. In *Computational Intelligence: An Introduction*, pages 551–579. John Wiley & Sons Ltd., Chichester, 2nd edition, 2007.

[28] M. H. A. Bonte. Solving optimisation problems in metal forming using FEM: A metamodel based optimisation algorithm. Technical report, University of Twente, Enschede, 2005.

[29] J. C. Lagarias, J. A. Reeds, M. H. Wright, and P. E. Wright. Convergence properties of the Nelder-Mead simplex method in low dimensions. *SIAM Journal on Optimization*, 9(1):112–147, 1998.

[30] H. S. Park and X. P. Dang. Structural optimization based on CAD-CAE integration and metamodeling techniques. *CAD Computer Aided Design*, 42(10):889–902, 2010.

[31] M. H. A. Bonte, A. H. Van Den Boogaard, and J. Huétink. An optimisation

strategy for industrial metal forming processes: Modelling, screening and solving of optimisation problems in metal forming. *Structural and Multidisciplinary Optimization*, 35(6):571–586, 2008.

[32] ASTM E2448-11. Standard Test Method for Determining the Superplastic Properties of Metallic Sheet, 2011.

[33] B. H. Cheong, J. Lin, and A. A. Ball. Modelling of hardening due to grain growth for a superplastic alloy. *Journal of Materials Processing Technology*, 119(1-3):361–365, 2001.

[34] Abaqus. *Abaqus 6.14 Documentation*. Dassault Systèmes Simulia Corp., Providence, RI, USA, 2014.

[35] S. Cooreman, D. Lecompte, H. Sol, J. Vantomme, and D. Debruyne. Identification of mechanical material behavior through inverse modeling and DIC. *Experimental Mechanics*, 48(4):421–433, 2008.

[36] R. Jin, W. Chen, and T. W. Simpson. Comparative studies of metamodeling techniques under multiple modeling criteria. *Structural and Multidisciplinary Optimization*, 23(1):1–13, 2001.

[37] N. V. Queipo, R. T. Haftka, W. Shyy, T. Goel, R. Vaidyanathan, and P. K. Tucker. Surrogate-based analysis and optimization. *Progress in Aerospace Sciences*, 41(1):1–28, 2005.

[38] Y. Chen, K. Kibble, R. Hall, and X. Huang. Numerical analysis of superplastic blow forming of Ti-6Al-4V alloys. *Materials & Design*, 22(8):679–685, 2001.

[39] S. G. Luckey, P. A. Friedman, and K. J. Weinmann. Correlation of finite element analysis to superplastic forming experiments. *Journal of Materials Processing Technology*, 193(1-3):30–37, 2007.

[40] R. D. Wood and J. Bonet. A review of the numerical analysis of superplastic forming. *Journal of Materials Processing Technology*, 60(1-4):45–53, 1996.

APPENDIX A

A.1 IMPLEMENTATION OF THE TANH-MODEL

The increment in equivalent plastic strain $\Delta\varepsilon_{\mathrm{p}}$ and its derivative with respect to Von Mises flow stress $\frac{\partial\Delta\varepsilon_{\mathrm{p}}}{\partial\sigma}$ have to be defined and updated in the Abaqus creep user subroutine. The tanh-model, which is given in Eq. (3.4), can be implemented into Abaqus using the Newton-Rhapson method

$$\frac{1}{\frac{\partial \mathrm{Res}}{\partial \log\dot{\varepsilon}}}\Delta(\log\dot{\varepsilon}) = -\mathrm{Res}\ , \tag{A.1}$$

where the residual Res is given by

$$\mathrm{Res} = \log\sigma - c_1\tanh\left(c_2\log\dot{\varepsilon} + c_2c_3\right) - c_1c_4 - c_5\log\dot{\varepsilon}\ , \tag{A.2}$$

and $\frac{\partial \mathrm{Res}}{\partial \log\dot{\varepsilon}}$ is given by

$$\frac{\partial \mathrm{Res}}{\partial \log\dot{\varepsilon}} = c_1c_2\left(\tanh\left(c_2c_3 + c_2\log\dot{\varepsilon}\right)^2 - 1\right) - c_5\ . \tag{A.3}$$

The increment in equivalent plastic strain $\Delta\varepsilon_{\mathrm{p}}$ is given by

$$\Delta\varepsilon_{\mathrm{p}} = 10^{\log\dot{\varepsilon}}\Delta t\ , \tag{A.4}$$

where Δt is the increment in time. The derivative of the equivalent plastic strain with respect to Von Mises flow stress $\frac{\partial\Delta\varepsilon_{\mathrm{p}}}{\partial\sigma}$ is given by

$$\frac{\partial\Delta\varepsilon_{\mathrm{p}}}{\partial\sigma} = \frac{10^{\log\dot{\varepsilon}}\Delta t}{\sigma\left(c_5 - c_1c_2\left(\tanh\left(c_2\log\dot{\varepsilon} + c_2c_3\right)^2 - 1\right)\right)}\ . \tag{A.5}$$

A.2 IMPLEMENTATION INTO ABAQUS

The subroutine of the tanh-model is given in Listing A.1. The programming language of the subroutine is Fortran. The flag LEXIMP indicates that implicit integration is used when it is equal to one. DECRA(1) and DECRA(5) are calculated when implicit integration is used. DECRA(1) is the increment in equivalent plastic strain $\Delta\varepsilon_{\mathrm{p}}$ and DECRA(5) is its derivative with respect to Von Mises flow stress $\frac{\partial\Delta\varepsilon_{\mathrm{p}}}{\partial\sigma}$.

Listing A.1: tanh-model subroutine

```
      SUBROUTINE CREEP(DECRA,DESWA,STATEV,SERD,EC,ESW,P,QTILD,
     1 TEMP,DTEMP,PREDEF,DPRED,TIME,DTIME,CMNAME,LEXIMP,LEND,
     2 COORDS,NSTATV,NOEL,NPT,LAYER,KSPT,KSTEP,KINC)
C
      INCLUDE 'ABA_PARAM.INC'
C
      CHARACTER*80 CMNAME
C
      DIMENSION DECRA(5),DESWA(5),STATEV(*),PREDEF(*),DPRED(*),
     1  TIME(3),EC(2),ESW(2),COORDS(*)
C
      DOUBLE PRECISION C1,C2,C3,C4,C6,LOGED
      REAL R,TOL
      INTEGER I
C
C     DEFINE CONSTANTS
C
      C1 = 1.20604260108782
      C2 = 0.596232135571322
      C3 = 3.69578433626352
      C4 = 1.13171090212027
      C6 = 0.167365079747966
C
C     NEWTON-RHAPSON METHOD TO FIND LOG OF STRAIN RATE
C
      R = 1E+03
      LOGED = -4E+00
      TOL = 1E-03
          I = 1
      DO WHILE (ABS(R).GT.TOL)
```

```
            R = LOG10(QTILD) - C1*TANH(C2*LOGED + C2*C3) - C1*C4 - C6*LOGED
          DRDLOGED = C1*C2*(TANH(C2*C3 + C2*LOGED)**2 - 1) - C6
            A = 1/DRDLOGED
          LOGED = LOGED - R*A
          I = I + 1
          IF (I.GE.100) R = (TOL + 1)
          END DO
C
C      BACKWARD EULER METHOD TO FIND THE EQUIVALENT CREEP STRAIN INCREMENT
C
          DECRA(1) = DTIME*10**(LOGED)
          IF (LEXIMP.EQ.1) THEN
          DECRA(5) = (DTIME*(10**LOGED))/(QTILD*(C6 - C1*C2*
        1             (TANH(C2*LOGED + C2*C3)**2 - 1)))
          END IF
C
          OPEN(UNIT=105,FILE='F:\results.dat')
          WRITE(105,*) QTILD,R,LOGED
          RETURN
          END
```

The subroutine of the SV-sinh model is given is Listing A.2. The material parameters of set 3 is used in Listing A.2. The material parameters are defined and then the state variables are calculated. The flag LEND indicates the end of the increment when it is equal to one. The state variables R and d are stored in STATEV(1) and STATEV(3) during the increment. The final values of the state variables R and d are stored in STATEV(2) and STATEV(4) at the end of the increment. The previous stress is required for the implicit trapezoidal method which is stored in STATEV(5) during the increment and in STATEV(6) at the end of the increment.

Listing A.2: SV-sinh model subroutine

```
      SUBROUTINE CREEP(DECRA,DESWA,STATEV,SERD,EC,ESW,P,QTILD,
     1 TEMP,DTEMP,PREDEF,DPRED,TIME,DTIME,CMNAME,LEXIMP,LEND,
     2 COORDS,NSTATV,NOEL,NPT,LAYER,KSPT,KSTEP,KINC)
C
          INCLUDE 'ABA_PARAM.INC'
C
          CHARACTER*80 CMNAME
C
```

```
      DIMENSION DECRA(5),DESWA(5),STATEV(*),PREDEF(*),DPRED(*),
     1  TIME(3),EC(2),ESW(2),COORDS(*)
C
      DOUBLE PRECISION gam,b2,k,a2,b,Q,a1,b1,gam0,phi,Rn,dn,
     1  Rn1,dn1,NrmR,sn1,sn,edn1,edn,Rdn1,Rdn,ddn1,ddn,
     2  dResRdRn1,dResRddn1,dResddRn1,dResdddn1,dResRdsn1,
     3  dResddsn1,dt,ResR,Resd,ddedsn1,ddedRn1,ddeddn1,
     4  dx(2,1),dxdsn1(2,1)
      REAL tol
      INTEGER ii
C
C     Constants (set 3)
C
      gam  = 2.42525494083261
      b2   = 0.115322709953736
      k    = 1.56027337605259e-15
      a2   = 0.0570885260943802
      b    = 1.03296596640274
      Q    = 4.50906065554077
      a1   = 9.02494952231401
      b1   = 1.734696932733
      gam0 = 4.80289778053948
      phi  = 6.91438021661459e-20
      tol  = 10E-8
      dt   = DTIME
      sn1  = QTILD
C
C     State variables
C
      R_DuringInc  = STATEV(1)
      R_EndPrevInc = STATEV(2)
      d_DuringInc  = STATEV(3)
      d_EndPrevInc = STATEV(4)
      s_DuringInc  = STATEV(5)
      s_EndPrevInc = STATEV(6)
C
C     Calculate Rn1 and dn1
C
      Rn   = R_EndPrevInc
      dn   = d_EndPrevInc
      sn   = s_EndPrevInc
```

```
      Rn1  = Rn + 1E-4
      dn1  = dn + 1E-4
      NrmR = 1000
      ii   = 0
      DO WHILE ((NrmR.GT.tol).AND.(ii.LT.10))
      ii = ii + 1
C
      edn1 = a2*SINH(b2*(sn1 - Rn1 - k))*dn1**(-gam)
      edn  = a2*SINH(b2*(sn - Rn - k))*dn**(-gam)
      Rdn1 = b*(Q - Rn1)*edn1
      Rdn  = b*(Q - Rn)*edn
      ddn1 = a1*dn1**(-gam0) + b1*dn1**(-phi)*edn1
      ddn  = a1*dn**(-gam0) + b1*dn**(-phi)*edn
C
      ResR = Rn1 - Rn - dt/2*(Rdn1 + Rdn)
      Resd = dn1 - dn - dt/2*(ddn1 + ddn)
      NrmR = SQRT(ResR**2 + Resd**2)
C
      dResRdRn1 = 1 - (dt*((a2*b*SINH(b2*(Rn1 + k -
     1             sn1)))/dn1**gam -(a2*b*b2*COSH(b2*
     2             (Rn1 + k - sn1))*(Q -Rn1))/dn1**gam))/2
      dResRddn1 = -(a2*b*dt*gam*SINH(b2*(Rn1 + k - sn1))
     1             *(Q -Rn1))/(2*dn1**(gam + 1))
      dResddRn1 = (a2*b1*b2*dt*COSH(b2*(Rn1 + k -
     1              sn1)))/(2*dn1**gam*dn1**phi)
      dResdddn1 = 1 - (dt*((a2*b1*gam*SINH(b2*(Rn1 +
     1             k - sn1)))/(dn1**phi*dn1**(gam + 1)) -
     2            (a1*gam0)/dn1**(gam0 + 1) + (a2*b1*phi*
     3             SINH(b2*(Rn1 + k - sn1)))/(dn1**gam*
     4             dn1**(phi + 1))))/2
C
      dx(1,1) = -(ResR*dResdddn1 - Resd*dResRddn1)/
     1            (dResRdRn1*dResdddn1 - dResddRn1*
     2             dResRddn1)
      dx(2,1) = -(dResRdRn1*Resd - dResddRn1*ResR)/
     1            (dResRdRn1*dResdddn1 - dResddRn1*
     2             dResRddn1)
      Rn1     = Rn1 + dx(1,1)
      dn1     = dn1 + dx(2,1)
      END DO
C
```

```
C       Update DECRA(1), DECRA(5) and STATEV(*)
C
        IF (LEND.EQ.1 .AND. LEXIMP.EQ.1) THEN
C
        IF (sn1.LT.(k+R_EndPrevInc)) THEN
        DECRA(1)  = 0
        DECRA(5)  = 0
        STATEV(1) = R_EndPrevInc
        STATEV(2) = R_EndPrevInc
        STATEV(3) = d_EndPrevInc
        STATEV(4) = d_EndPrevInc
        STATEV(5) = sn1
        STATEV(6) = sn1
        ELSE
        DECRA(1)   = -(dt*((a2*SINH(b2*(Rn + k - sn)))/
     1                dn**gam + (a2*SINH(b2*(Rn1 + k -
     2                sn1)))/dn1**gam))/2
C
        dResRdsn1   = -(a2*b*b2*dt*COSH(b2*(Rn1 + k - sn1))*
     1                (Q - Rn1))/(2*dn1**gam)
        dResddsn1   = -(a2*b1*b2*dt*COSH(b2*(Rn1 + k -
     1                 sn1)))/(2*dn1**gam*dn1**phi)
        dxdsn1(1,1) = -(dResRdsn1*dResdddn1 - dResddsn1*
     1                 dResRddn1)/(dResRdRn1*dResdddn1 -
     2                 dResddRn1*dResRddn1)
        dxdsn1(2,1) = -(dResRdRn1*dResddsn1 - dResddRn1*
     1                 dResRdsn1)/(dResRdRn1*dResdddn1 -
     2                 dResddRn1*dResRddn1)
C
        ddedsn1 = (a2*b2*dt*COSH(b2*(Rn1 + k - sn1)))
     1           /(2*dn1**gam)
        ddedRn1 = -(a2*b2*dt*COSH(b2*(Rn1 + k - sn1)))
     1            /(2*dn1**gam)
        ddeddn1 = (a2*dt*gam*SINH(b2*(Rn1 + k - sn1)))/
     1           (2*dn1**(gam + 1))
C
        DECRA(5)= ddedsn1 + ddedRn1*dxdsn1(1,1) +
     1           ddeddn1*dxdsn1(2,1)
C
        STATEV(1) = Rn1
        STATEV(2) = Rn1
```

```
      STATEV(3) = dn1
      STATEV(4) = dn1
      STATEV(5) = sn1
      STATEV(6) = sn1
      END IF
C
      ELSE IF (LEND.EQ.0 .AND. LEXIMP.EQ.1) THEN
C
      IF (sn1.LT.(k+R_EndPrevInc)) THEN
      DECRA(1)  = 0
      DECRA(5)  = 0
      STATEV(1) = R_EndPrevInc
      STATEV(2) = R_EndPrevInc
      STATEV(3) = d_EndPrevInc
      STATEV(4) = d_EndPrevInc
      STATEV(5) = sn1
      STATEV(6) = s_EndPrevInc
      ELSE
      DECRA(1)   = -(dt*((a2*SINH(b2*(Rn + k - sn)))/
     1               dn**gam + (a2*SINH(b2*(Rn1 + k -
     2               sn1)))/dn1**gam))/2
C
      dResRdsn1   = -(a2*b*b2*dt*COSH(b2*(Rn1 + k - sn1))*
     1               (Q - Rn1))/(2*dn1**gam)
      dResddsn1   = -(a2*b1*b2*dt*COSH(b2*(Rn1 + k -
     1                sn1)))/(2*dn1**gam*dn1**phi)
      dxdsn1(1,1) = -(dResRdsn1*dResdddn1 - dResddsn1*
     1                dResRddn1)/(dResRdRn1*dResdddn1 -
     2                dResddRn1*dResRddn1)
      dxdsn1(2,1) = -(dResRdRn1*dResddsn1 - dResddRn1*
     1                dResRdsn1)/(dResRdRn1*dResdddn1 -
     2                dResddRn1*dResRddn1)
C
      ddedsn1 = (a2*b2*dt*COSH(b2*(Rn1 + k - sn1)))
     1          /(2*dn1**gam)
      ddedRn1 = -(a2*b2*dt*COSH(b2*(Rn1 + k - sn1)))
     1           /(2*dn1**gam)
      ddeddn1 = (a2*dt*gam*SINH(b2*(Rn1 + k - sn1)))/
     1          (2*dn1**(gam + 1))
C
      DECRA(5)= ddedsn1 + ddedRn1*dxdsn1(1,1) +
```

```
     1            ddeddn1*dxdsn1(2,1)
C
        STATEV(1) = Rn1
        STATEV(2) = R_EndPrevInc
        STATEV(3) = dn1
        STATEV(4) = d_EndPrevInc
        STATEV(5) = sn1
        STATEV(6) = s_EndPrevInc
        END IF
C
        END IF
C
        OPEN(UNIT=105,FILE='D:\results.dat')
        WRITE(105,*) KINC,DECRA(1),DECRA(5)
C
        END SUBROUTINE
```

APPENDIX B

B.1 INTRODUCTION

The purpose of the element and mesh studies are to find the appropriate element type and mesh for the finite element models that are used in this study.

B.2 TENSILE TEST MESH STUDY

B.2.1 Method

Continuum, shell or membrane elements can be used for finite element analyses of superplastic forming processes [38]. The different elements investigated are described in Table B.1. Two and four layers of continuum elements through the thickness of the model are investigated. The model meshed with S4 elements has one layer of elements through the thickness of the model, and has 15 Gauss integration points through the thickness.

Table B.1: Element types investigated

Element types	Description
C3D8	Eight-node linear brick element
C3D20	Twenty-node quadratic brick element
S4	Four-node general purpose shell element with finite membrane strains

Two tensile test meshes were investigated and are shown in Figure B.1. Tensile test mesh 1

has a fine mesh of elements everywhere, and tensile test mesh 2 has an unstructured mesh of elements with smaller elements in the middle of the gauge section. The dimensions of the tensile test model are given in Figure 3.23.

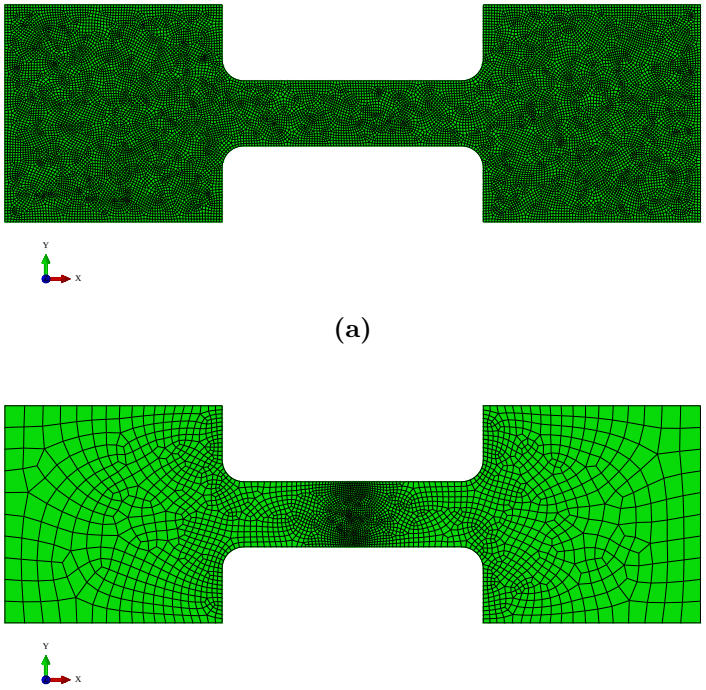

(a)

(b)

Figure B.1: Tensile test mesh (a) 1 and (b) 2

The boundary conditions of the tensile test model are described in Chapter 3. The specimen is pulled to 0.71 strain at a strain rate of 10^{-3} s^{-1} in order to investigate mesh dependence before localised thinning occurs. The specimen is also pulled to 250% strain at a strain rate of 10^{-3} s^{-1} and 5×10^{-3} s^{-1} in order to investigate mesh dependence after localised thinning occurs. The strain rate in the gauge is achieved with a velocity boundary condition which is given by Eq. (3.57).

The material is assumed to be isotropic Ti-6Al-4V with an initial grain size of 6.4 µm. Material parameters set 3 of the SV-sinh model, which is given in Table 3.2, is used for the mesh and element study of the tensile test model. The process is assumed to be isothermal at a temperature of 927°C.

B.2.2 Results

The final Von Mises stress distribution results of the different tensile test meshes with different element types for the pre-necking mesh investigation are given in Figures B.2, B.3, B.4, and B.5. There are no observable differences in stress results between the different tensile test meshes of different element types for the pre-necking mesh investigation. It can be observed that there is a significant change in shape in the fillet areas.

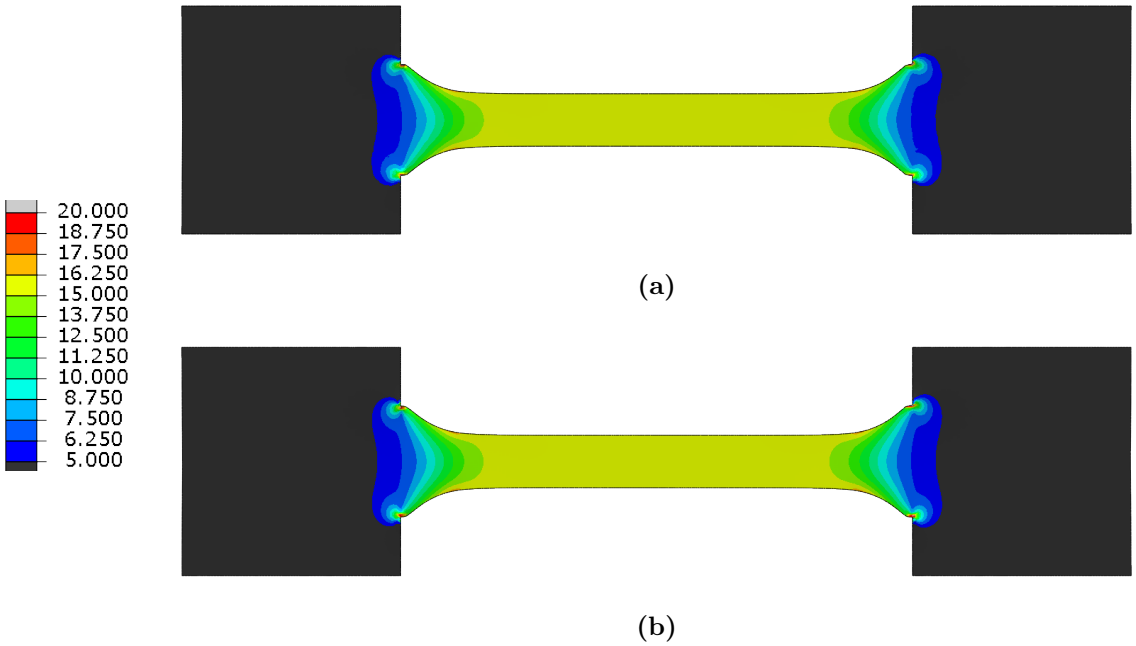

Figure B.2: Final Von Mises stress results of the tensile test for mesh 1 with 4 layers of (a) C3D8 and (b) C3D20 elements through the thickness for the pre-necking mesh investigation

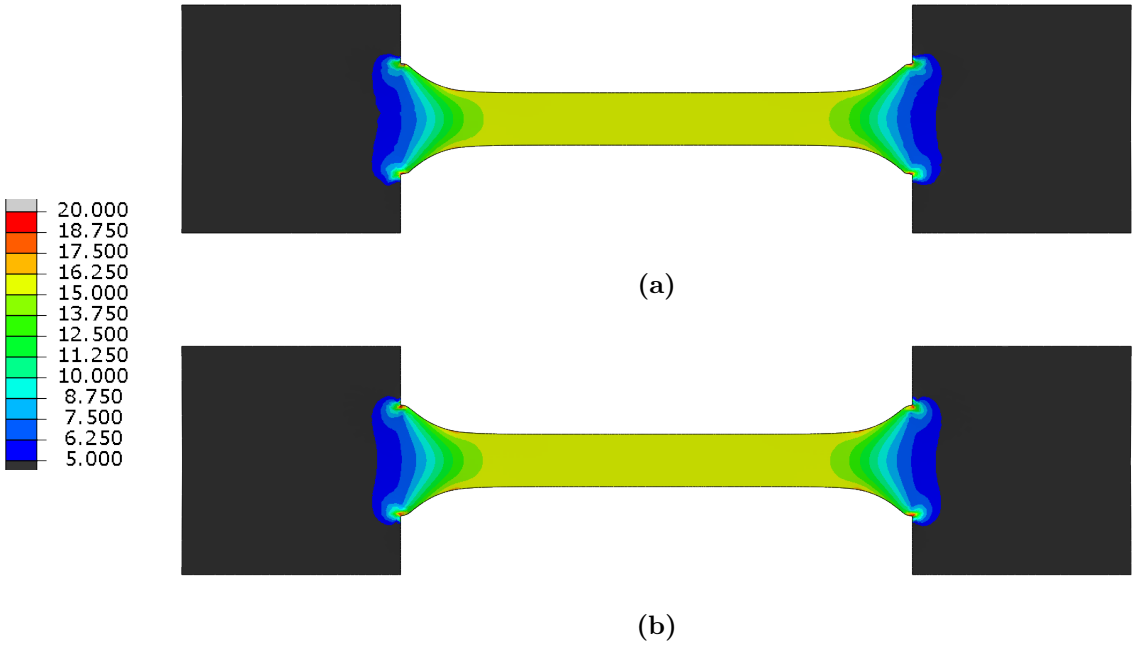

Figure B.3: Final Von Mises stress results of the tensile test for mesh 2 with 4 layers of (a) C3D8 and (b) C3D20 elements through the thickness for the pre-necking mesh investigation

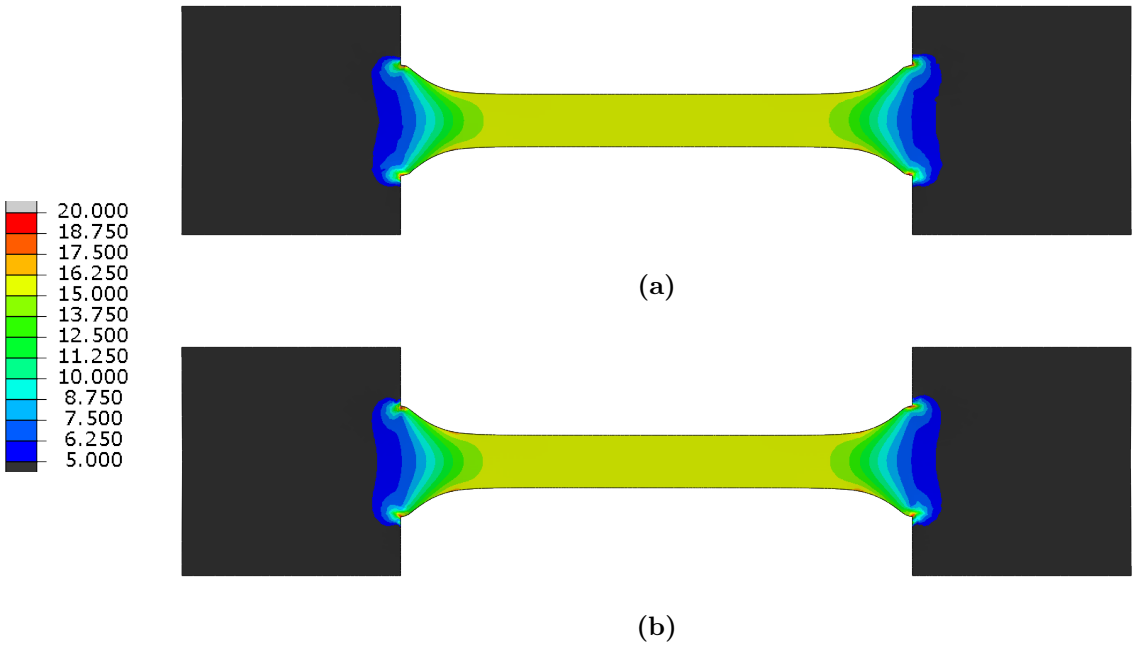

Figure B.4: Final Von Mises stress results of the tensile test for mesh 2 with 2 layers of (a) C3D8 and (b) C3D20 elements through the thickness for the pre-necking mesh investigation

Figure B.5: Final Von Mises stress results of the tensile test for mesh 2 with 1 layer of S4 elements through the thickness for the pre-necking mesh investigation

The final Von Mises stress results along the middle of the tensile test model for the different meshes with different element types for the pre-necking mesh investigation are given in Figure B.6. The stress results lie on top of each other. There is viscoplastic flow of material from the tabs to the gauge section.

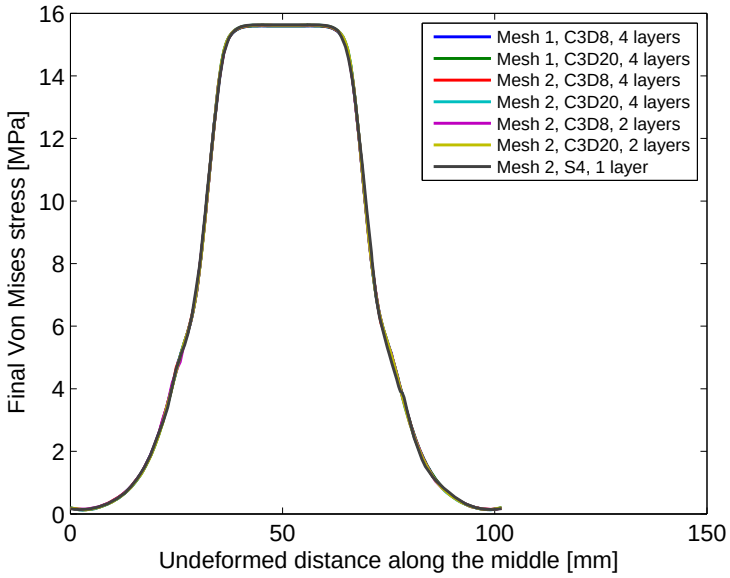

Figure B.6: Final Von Mises stress results along the middle of the tensile test model for the different meshes with different element types for the pre-necking mesh investigation

The final thickness distribution results of the different tensile test meshes with different element types for the pre-necking mesh investigation are given in Figures B.7, B.8, B.9 and B.10. In all of the figures it can be observed that there is thinning near the fillet area, but

that the thickness becomes more uniform towards the middle of the gauge section.

The field output variable STH is the through thickness in Abaqus, but it is only available for shell elements. The thickness values for the continuum elements are calculated using the field output variable COPEN. COPEN is the distance between two contacting surfaces. The thickness is the absolute value of the COPEN field output variable in this case. The method to calculate the thickness with the field output variable COPEN with Abaqus is given below.

1. Import the final formed sheet into Abaqus CAE.
2. Create a material with elastic properties $E = 1000$ MPa and $\nu = 0.3$.
3. Create a section property and assign it to the formed sheet.
4. Create an instance in the Assembly module.
5. Create a general, static deformation step in the Step module, and accept all of the default values.
6. Switch to the Interaction module. Create a contact interaction property with default geometric interaction properties.
7. Create a surface-to-surface contact interaction. In the case of the tensile test model, select the back surface as the master surface and the front surface as the slave surface. In the case of the superplastic forming of a rectangular box, select the surface closest to the die as the master surface and the surface furthest from the die as the slave surface.
8. Create a job. Right click on the job and run a data check on it.
9. Open the data checked job in Abaqus Viewer to see the field output COPEN.
10. Calculate the absolute value of COPEN using a Python script.

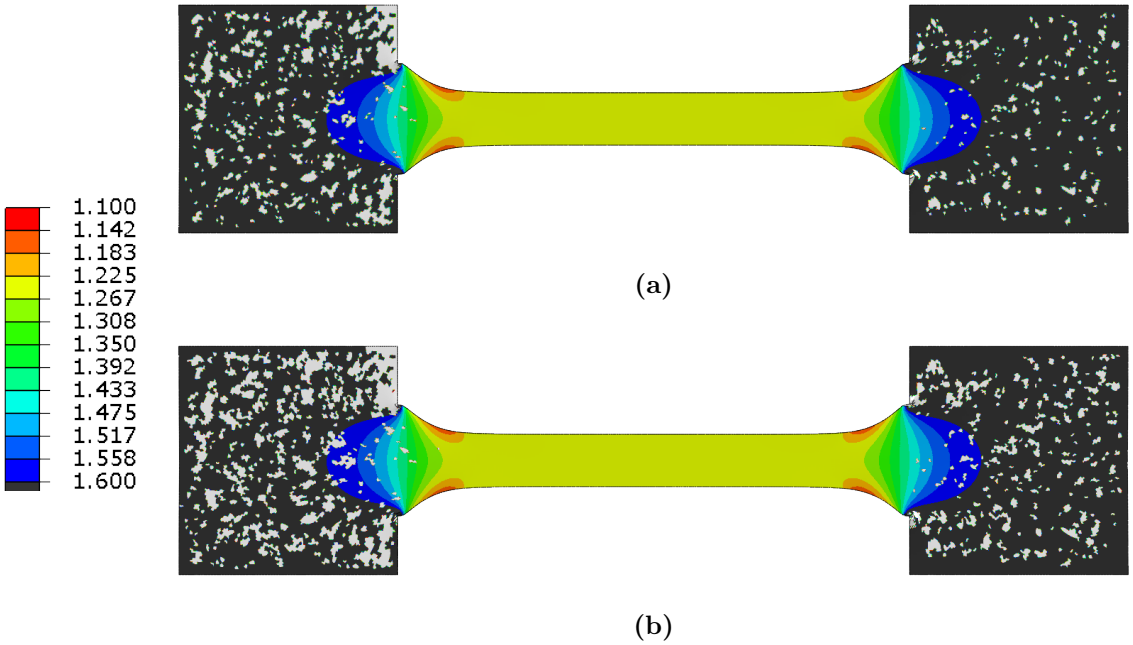

Figure B.7: Final thickness results of the tensile test for mesh 1 with 4 layers of (a) C3D8 and (b) C3D20 elements through the thickness for the pre-necking mesh investigation

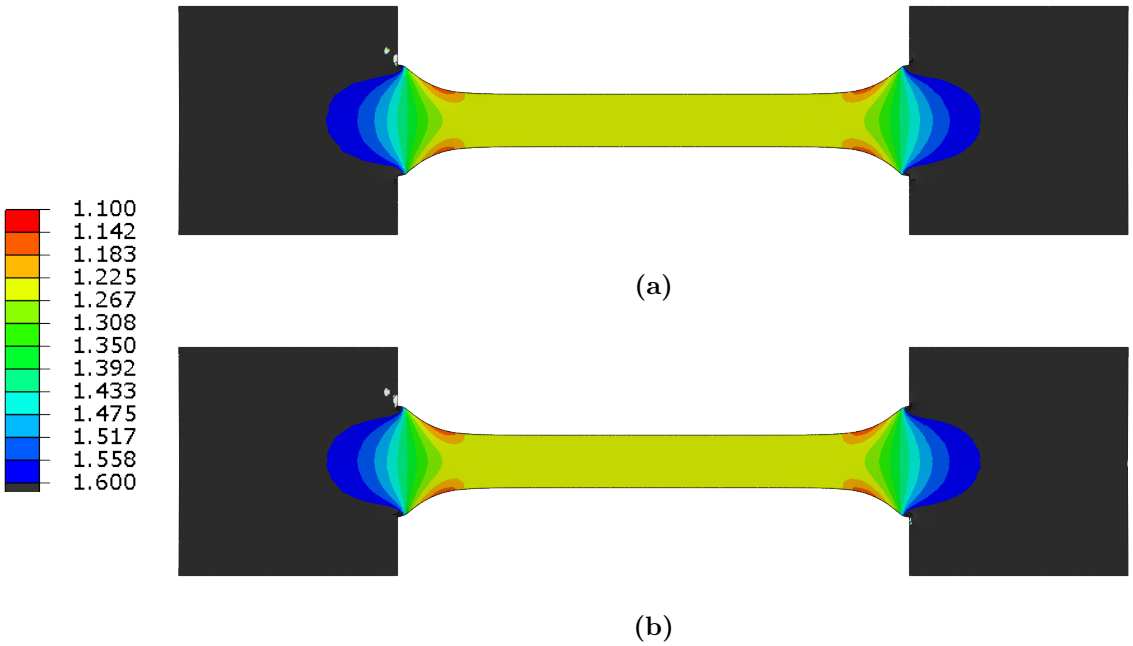

Figure B.8: Final thickness results of the tensile test for mesh 2 with four layers of (a) C3D8 and (b) C3D20 elements through the thickness for the pre-necking mesh investigation

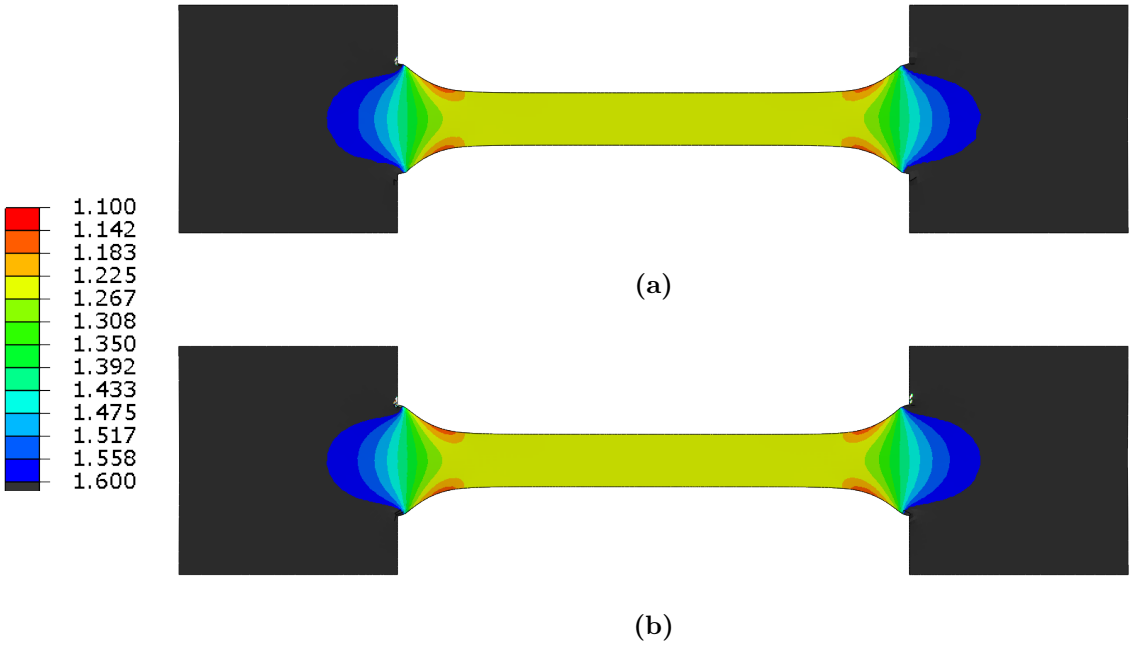

Figure B.9: Final thickness results of the tensile test for mesh 2 with 2 layers of (a) C3D8 and (b) C3D20 elements through the thickness for the pre-necking mesh investigation

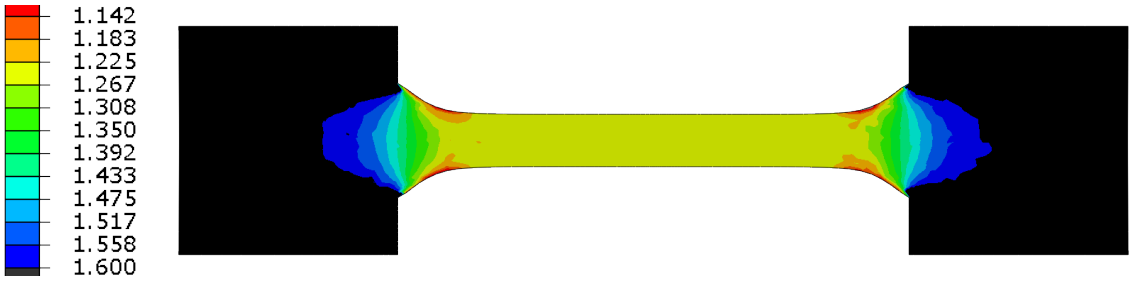

Figure B.10: Final thickness results of the tensile test for mesh 2 with 1 layer of S4 elements through the thickness for the pre-necking mesh investigation

The final thickness results along the middle of the tensile test model for the different tensile test meshes with different element types for the pre-necking mesh investigation are given in Figure B.11. The thickness results lie mostly on top of each other for the meshes meshed with continuum elements. The thickness results of the mesh with S4 elements is not as smooth as the thickness results of the meshes with continuum elements.

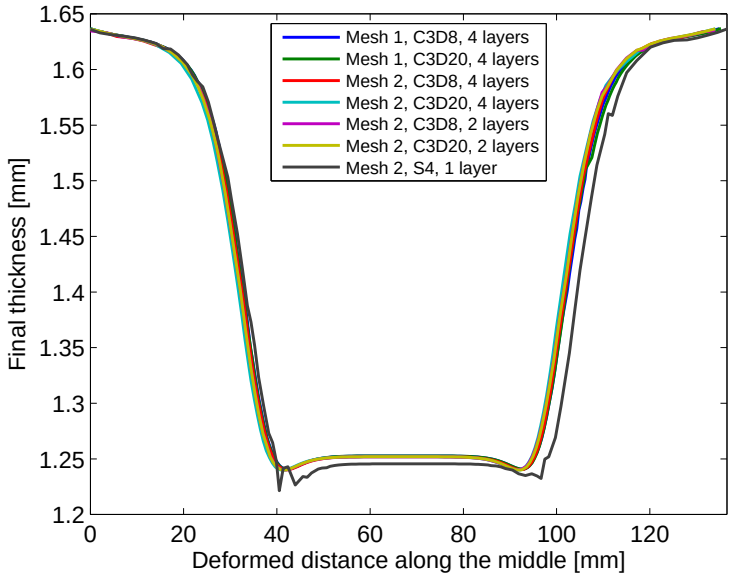

Figure B.11: Final thickness results along the middle of the tensile test model for the different meshes with different element types for the pre-necking mesh investigation

The mean final Von Mises stress $\sigma_{\text{f,Von Mises}}$ in the gauge section, mean final thickness h_{f} in the gauge section and the CPU time for the tensile test meshes with different element types for the pre-necking mesh investigation are given in Table B.2. Mesh 2 with S4 elements has the largest mean $\sigma_{\text{f,Von Mises}}$ value in the gauge section. This mesh also has the largest mean final thickness in the gauge section. Shell elements are not as expensive as solid elements in terms of CPU time, and a guideline for the ratio of the shell element size to radius has been reported by Luckey *et al.* [39].

Mesh 2 with two layers of C3D8 elements has the shortest CPU time which is less than the CPU time for mesh 2 with S4 elements. Mesh 1 with C3D20 elements has the longest CPU time. The number of elements through the thickness does not seem to have an effect on the final thickness results. It can be concluded that the tensile test for the pre-necking mesh investigation is not sensitive to the meshes with continuum elements.

Table B.2: Mean stress in the gauge section of the tensile test model for the different meshes with different element types for the pre-necking mesh investigation

Element type	**Tensile test mesh**	**Layers**	**Mean $\sigma_{\text{f,Von Mises}}$ in gauge [MPa]**	**Mean h_{f} in gauge [mm]**	**CPU time [s]**
C3D8	1	4	15.5977	1.25265	14 600
C3D20	1	4	15.598	1.25267	131 530
C3D8	2	4	15.6142	1.25205	2 085.2
C3D20	2	4	15.6242	1.25198	15 179
C3D8	2	2	15.6167	1.25184	891.20
C3D20	2	2	15.6192	1.25198	5 817.7
S4	2	1	15.6286	1.24556	2 062.9

The final Von Mises stress distribution results of the different tensile test meshes with different element types for the post-necking mesh investigation at 10^{-3} s^{-1} and 5×10^{-3} s^{-1} are given in Figures B.12 and B.13, respectively. There seems to be no significant differences between the Von Mises stress results of the models with different meshes and elements types at 10^{-3} s^{-1}.

The maximum Von Mises stress occurs in the area of localised thinning in Figure B.13. The Von Mises stress distribution is slightly different for each of the models in the region where localised thinning has occurred. This is because the material model cannot predict failure after localised thinning has occurred.

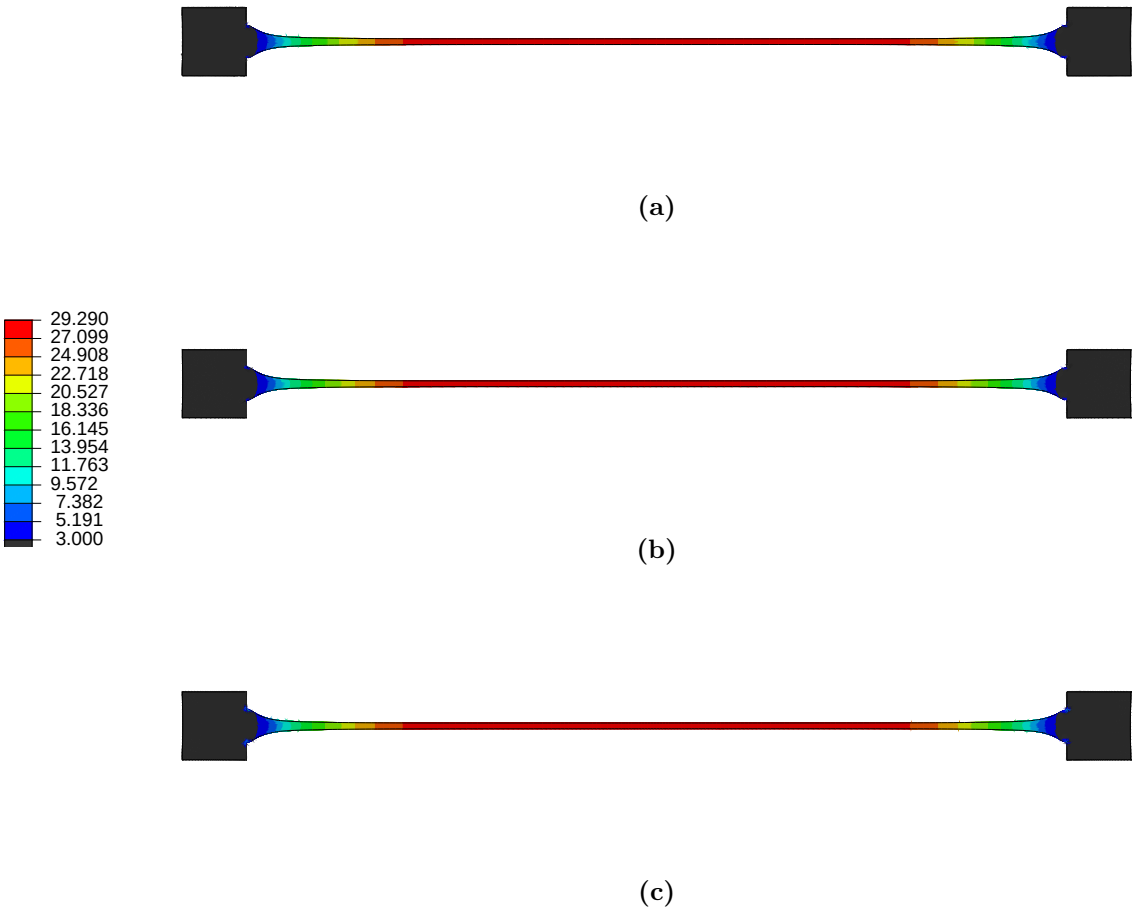

Figure B.12: Final Von Mises stress results of the tensile test for (a) mesh 1 with 4 layers of C3D8 elements, (b) mesh 2 with 4 layers of C3D8 elements, (c) mesh 2 with 4 layers of C3D20 elements for the post-necking mesh investigation at 10^{-3} s^{-1}

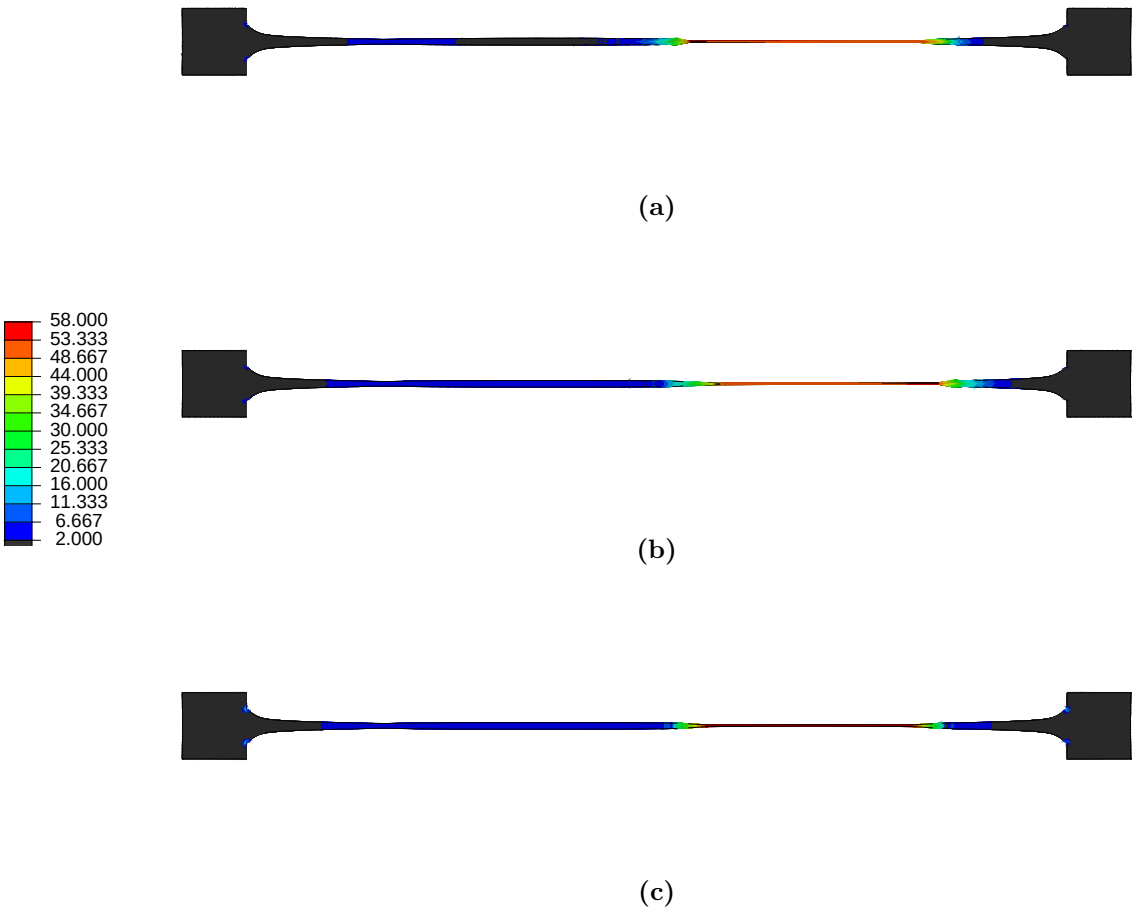

Figure B.13: Final Von Mises stress results of the tensile test for (a) mesh 1 with 4 layers of C3D8 elements, (b) mesh 2 with 4 layers of C3D8 elements, (c) mesh 2 with 4 layers of C3D20 elements for the post-necking mesh investigation at 5×10^{-3} s^{-1}

The final Von Mises stress results along the middle of the tensile test model for the different meshes with different element types for the post-necking mesh investigation are given in Figure B.14. There seems to be no difference between the Von Mises stress results of the model with mesh 2 of C3D8 elements and the model with mesh 2 of C3D20 elements at 10^{-3} s^{-1}. There is a slight difference in Von Mises stress results at 30 to 40 mm and 70 to 80 mm undeformed distance along the middle of the tensile test model for the model with mesh 1 of C3D8 elements and the model with mesh 2 of C3D8 elements at 10^{-3} s^{-1}.

The Von Mises stress results are unreliable at 5×10^{-3} s^{-1}, because the material model does

not account for failure after localised thinning has occurred.

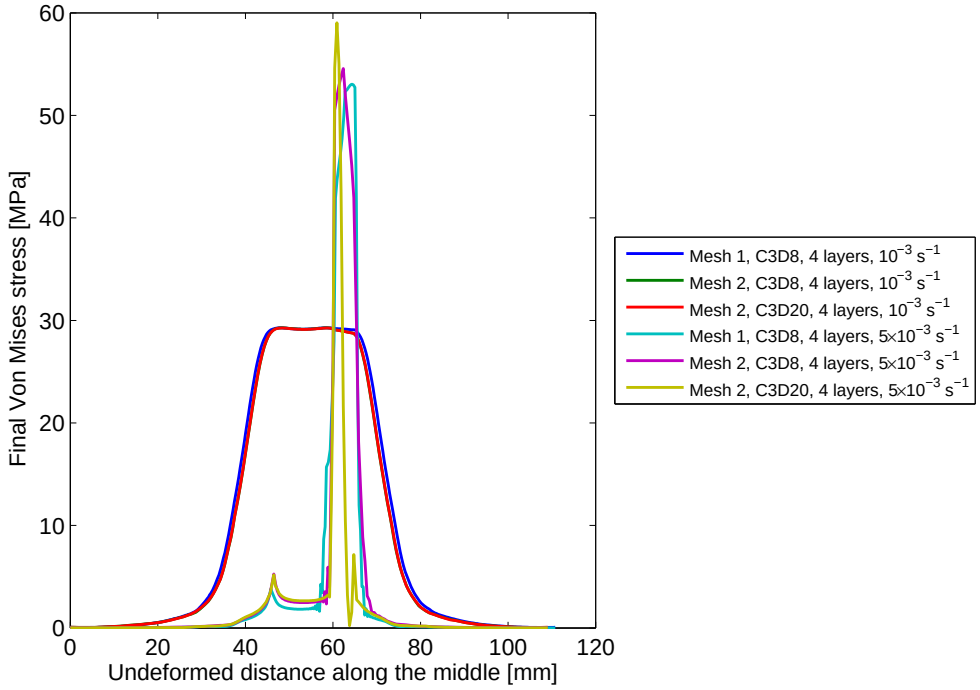

Figure B.14: Final Von Mises stress results along the middle of the tensile test model for the different meshes with different element types for the post-necking mesh investigation

The final thickness distribution results of the different tensile test meshes with different element types for the post-necking mesh investigation at 10^{-3} s^{-1} and 5×10^{-3} s^{-1} are given in Figures B.15 and B.16, respectively. The thickness results does not seem to be affected by the meshes and element types investigated at 10^{-3} s^{-1} and 5×10^{-3} s^{-1}.

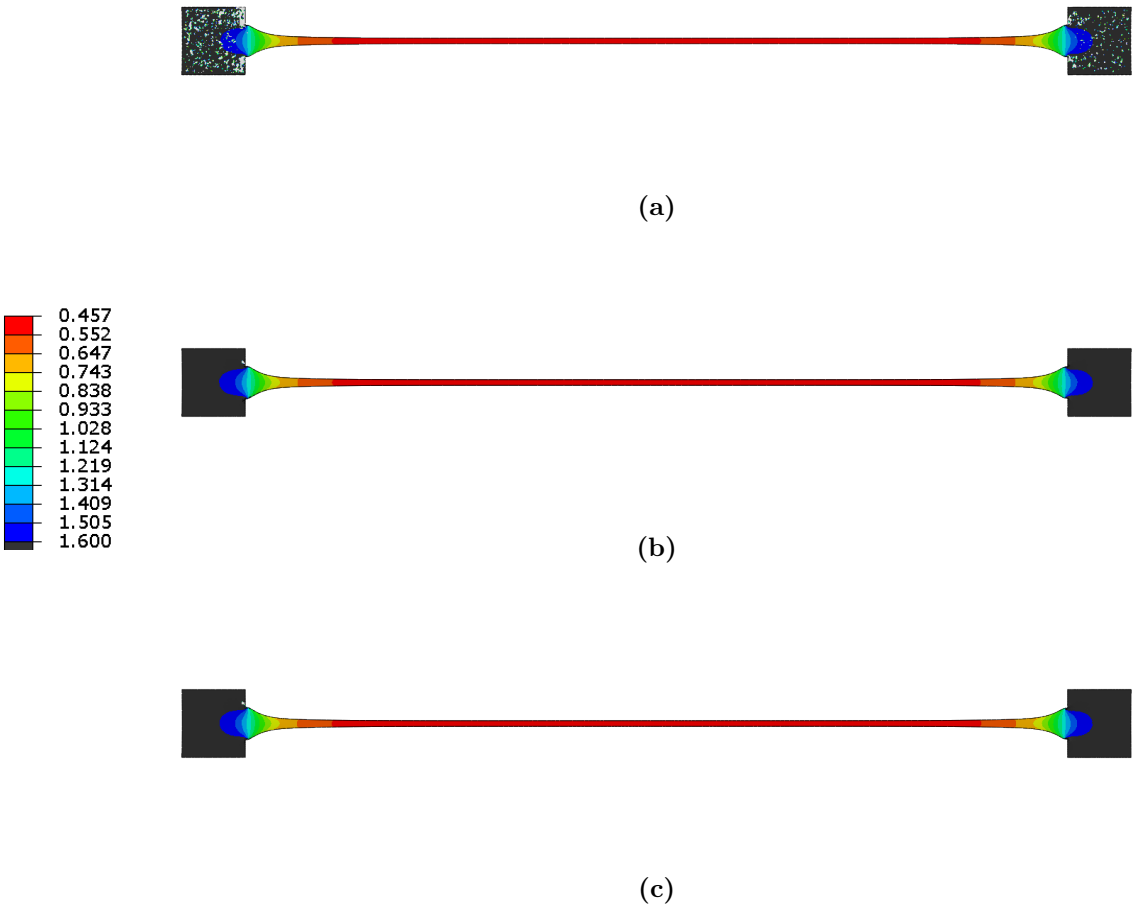

Figure B.15: Final thickness results of the tensile test for (a) mesh 1 with 4 layers of C3D8 elements, (b) mesh 2 with 4 layers of C3D8 elements, (c) mesh 2 with 4 layers of C3D20 elements for the post-necking mesh investigation at 10^{-3} s^{-1}

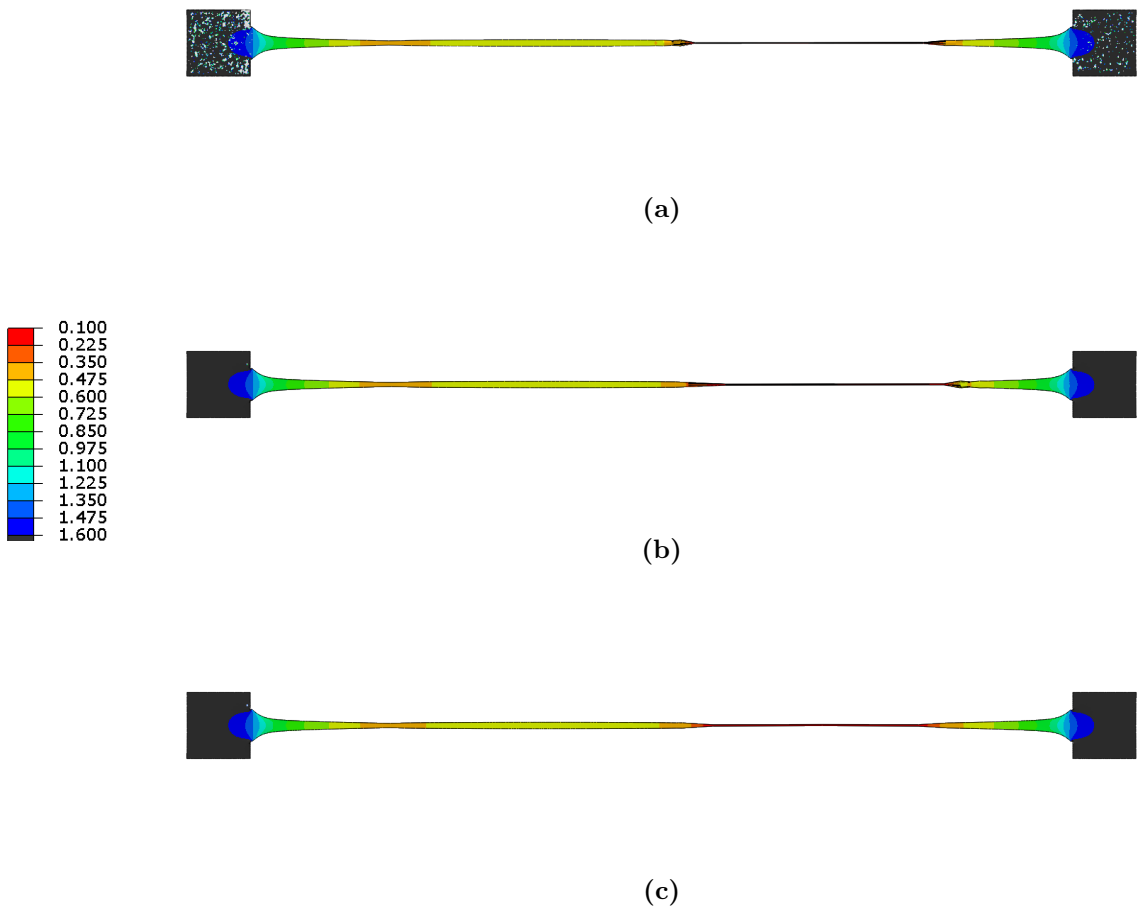

Figure B.16: Final thickness results of the tensile test for (a) mesh 1 with 4 layers of C3D8 elements, (b) mesh 2 with 4 layers of C3D8 elements, (c) mesh 2 with 4 layers of C3D20 elements for the post-necking mesh investigation at 5×10^{-3} s^{-1}

The final thickness results along the middle of the tensile test model for the different tensile test meshes with different element types for the post-necking mesh investigation are given in Figure B.17. The thickness results seem to be independent of the meshes and element types investigated at 10^{-3} s^{-1}.

The thickness drops almost to zero at 250 to 350 mm deformed distance along the tensile test model. Unstable thickness results can be observed in this region. The thickness results seem to be independent of the meshes and element types investigated before and after the unstable region.

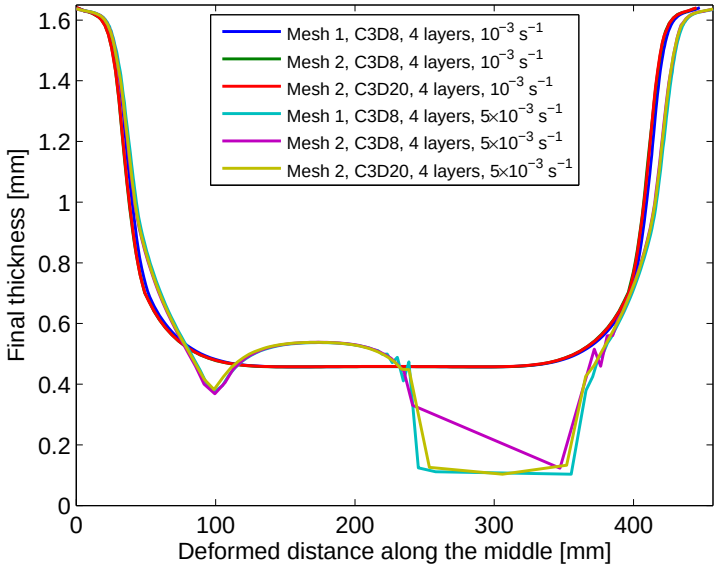

Figure B.17: Final thickness results along the middle of the tensile test model for the different meshes with different element types for the post-necking mesh investigation

B.3 MESH STUDY OF THE SUPERPLASTIC FORMING OF A BOX

B.3.1 Method

The deformable sheet does not initially require a fine mesh of elements, but as the sheet forms into the die cavity a refined mesh is required to capture the large deformations. Wood and Bonet [40] suggested an adaptive remeshing technique that uses a geometrical error measure based on computed and smoothed configurations as represented by deformation gradients. They added that a superplastic forming simulation cannot be accurate without remeshing the sheet as it is formed into the die. Adaptive remeshing for large deformations is not investigated, but an element and mesh study for the superplastic forming of a rectangular box is conducted.

The sheet size is 558.8 mm $\times$ 812.8 mm $\times$ 3.3 mm. Initial sheet mesh sizes of $22 \times 32 \times 1$, $44 \times 64 \times 1$ and $60 \times 100 \times 1$ elements are investigated. C3D8 and C3D20R elements are investigated. Twenty-node quadratic brick element with reduced integration. One and two layers of elements through the thickness of the sheet are also investigated.

The different die meshes investigated are shown in Figure B.18. The main difference between the three meshes is the mesh refinement at the radii, where die mesh 3 has the finest mesh at the radii. Die mesh 2 is used for the sheet element and mesh study. Rigid three dimensional three-node triangular (R3D3) elements and rigid three dimensional four-node facet (R3D4) elements are used to mesh the die. The dimensions of the die are given in Figure 3.34.

The boundary conditions of the superplastic forming of a rectangular box are given in Figure 3.35. The pressure calculated with the autopress routine for set 3 of the SV-sinh model at a strain rate of 10^{-3} s^{-1}, which is given in Figure 3.36, is used for this mesh and element study.

The material is assumed to be isotropic Ti-6Al-4V with an initial grain size of 6.4 µm. Material parameters set 3 of the SV-sinh model is used for this mesh and element study. The superplastic forming process is assumed to be isothermal at a temperature of 927°C.

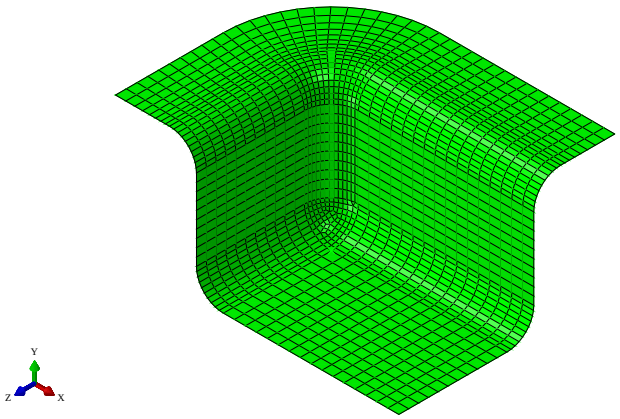

(a)

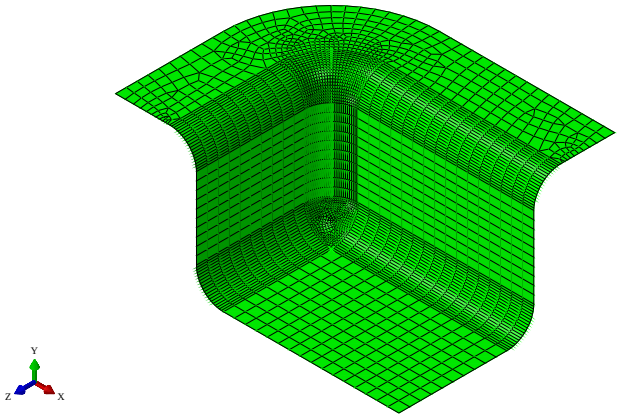

(b)

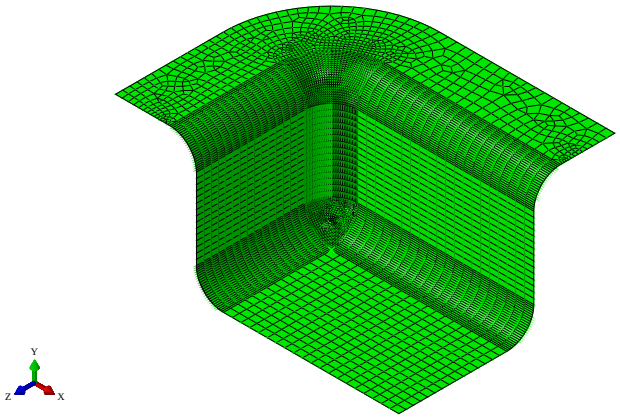

(c)

Figure B.18: Die mesh (a) 1, (b) 2 and (c) 3

B.3.2 Results

The final thickness distribution results for the different sheet meshes investigated are given in Figure B.19. Die mesh 2 is used for the sheet mesh study. The thickness results of the sheet mesh of $22 \times 32 \times 1$ C3D8 elements is not as smooth as the other sheet meshes investigated. There is no other significant differences in thickness results observable between the sheet meshes investigated in Figure B.19.

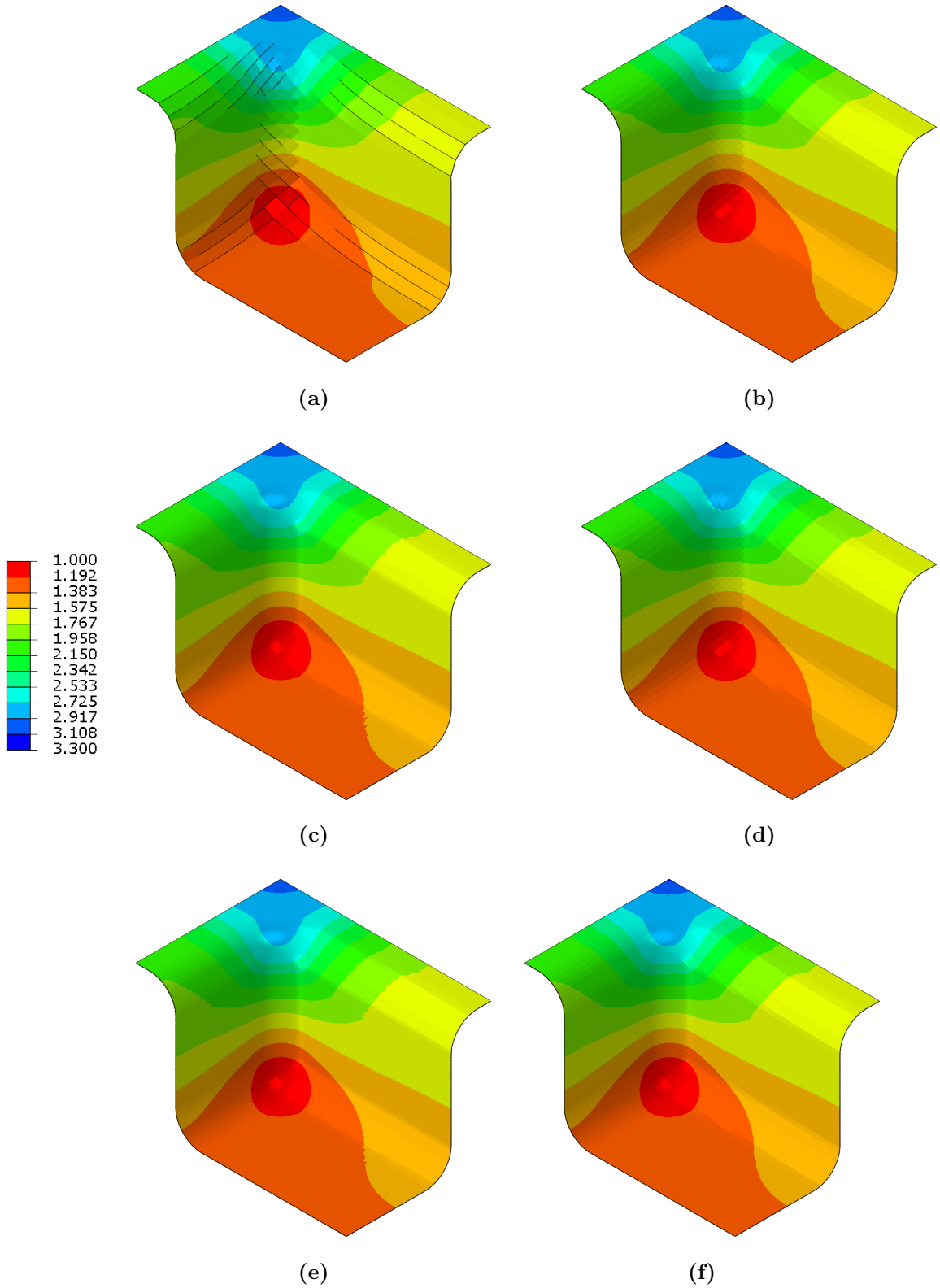

Figure B.19: Final thickness distribution results of the formed box for the with sheet mesh (a) $22 \times 32 \times 1$ C3D8, (b) $44 \times 64 \times 1$ C3D8, (c) $44 \times 64 \times 1$ C3D20R, (d) $44 \times 64 \times 2$ C3D8, (e) $44 \times 64 \times 2$ C3D20R, and (f) $60 \times 100 \times 1$ C3D8 elements

The final thickness results along the diagonal of the model for the different sheet meshes investigated are given in Figure B.20. The diagonal is the path 45° from the top corner of the sheet. The final minimum thickness $h_{\mathrm{f,min}}$, final gap between the die corner and formed sheet g_{f} and CPU time for the different sheet meshes investigated are given in Table B.3.

The final thickness along the diagonal for the sheet mesh of $60 \times 100 \times 1$ C3D8 elements differs slightly from the other sheet meshes investigated. The final minimum thickness of the sheet mesh of $44 \times 64 \times 1$ C3D20R elements is the smallest, but it only differs 0.14% from final minimum thickness of the sheet mesh of $60 \times 100 \times 1$ C3D8 elements.

There is significant final gap differences between the different sheet meshes investigated. The sheet mesh of $22 \times 32 \times 1$ C3D8 elements has the largest penetration into the die mesh. The final gap of the sheet mesh of $60 \times 100 \times 1$ C3D8 elements with die mesh 2 is the closest to zero. The sheet meshes with C3D20R elements seem to be stiffer than the C3D8 elements, because there is a positive gap value at the end of the simulation for the same applied pressure for the sheet meshes with C3D20R elements.

The number of elements through the thickness of the sheet has a small effect on the final gap. There is a 0.04% difference in final gap between the sheet meshes of $44 \times 64 \times 1$ C3D8 and $44 \times 64 \times 2$ C3D8 elements, and a 1.1% difference in final gap between the sheet meshes of $44 \times 64 \times 1$ C3D20R and $44 \times 64 \times 2$ C3D20R elements.

The CPU time of the sheet mesh of $44 \times 64 \times 2$ C3D20R elements is the highest due the large number of nodes. The CPU times increases 72% from the sheet mesh of $22 \times 32 \times 1$ C3D8 elements to the sheet mesh of $44 \times 64 \times 1$ C3D8 elements, and it increases 56% from the sheet mesh of $44 \times 64 \times 1$ C3D8 elements to the sheet mesh of $60 \times 100 \times 1$ C3D8 elements.

The sheet mesh of $60 \times 100 \times 1$ C3D8 elements will be used for investigations with the model of the superplastic forming of a rectangular box, because this mesh has the smoothest thickness results and its final gap value is the closest to zero.

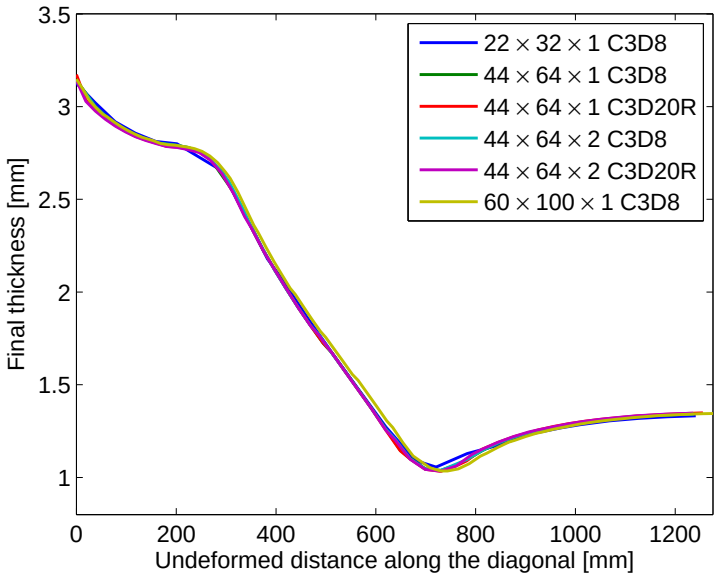

Figure B.20: Final thickness results along the diagonal for the different sheet meshes investigated

Table B.3: Final minimum thickness, final gap and CPU time for the different sheet meshes investigated

Sheet mesh	**Die mesh**	$h_{\mathrm{f,min}}$ **[mm]**	g_{f} **[mm]**	**CPU time [s]**
22 × 32 × 1 C3D8	2	1.0556	-1.2026	1 348.0
44 × 64 × 1 C3D8	2	1.0380	-0.7288	4 873.0
44 × 64 × 1 C3D20R	2	1.0333	0.1117	29 126
44 × 64 × 2 C3D8	2	1.0379	-0.7291	6 881.7
44 × 64 × 2 C3D20R	2	1.0339	0.1130	50 480
60 × 100 × 1 C3D8	2	1.0347	-0.0406	11 246

The final thickness results along the diagonal of the model for the three die meshes investigated are given in Figure B.21. A sheet mesh of 60 × 100 × 1 C3D8 elements are used for the die mesh study. The thickness results along the diagonal does not seem to be affected by the die mesh.

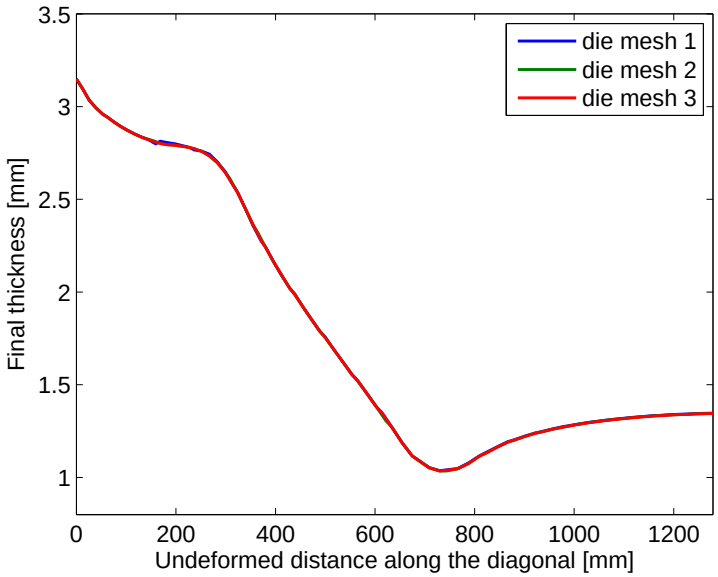

Figure B.21: Final thickness results along the diagonal for the three die meshes investigated

The final minimum thickness $h_{\mathrm{f,min}}$, final gap between the die corner and formed sheet g_{f} and CPU time for the different die meshes investigated are given in Table B.4. The final gap for die mesh 2 and 3 is the closet to zero.

The thickness is not significantly affected by the die mesh. There is a 0.2% difference in final minimum thickness between die mesh 1 and 2, and a 0.02% difference in final minimum thickness between die mesh 2 and 3. The CPU time is also not significantly affected by the die mesh. There is a 3% difference in CPU time between die mesh 1 and 2, and a 10% difference in CPU time between die mesh 2 and 3. Die mesh 2 is therefore chosen for investigations with the model of the superplastic forming of a rectangular box.

Table B.4: Final minimum thickness, final gap and CPU time for the different die meshes investigated

Die mesh	**Sheet mesh**	$h_{\mathrm{f,min}}$ **[mm]**	g_{f} **[mm]**	**CPU time [s]**
1	$60 \times 100 \times 1$ C3D8	1.0370	0.2115	11 617
2	$60 \times 100 \times 1$ C3D8	1.0347	-0.0406	11 246
3	$60 \times 100 \times 1$ C3D8	1.0349	-0.0404	12 606

B.4 CONCLUSION

The final thickness results and final Von Mises stress results of the tensile test models is not sensitive to the meshes with continuum elements, or the number of layers of continuum elements through the thickness for the pre-necking mesh investigation. The final thickness results and final Von Mises stress results of the tensile test models is not sensitive to the meshes with C3D8 and C3D20 elements for the mesh investigation at 10^{-3} s^{-1}. Localised thinning occurs in the tensile test models at 5×10^{-3} s^{-1}. The thickness results seem to be independent of the meshes and element types investigated before and after the thinned region. Tensile test mesh 2 of C3D8 elements are used for investigations with the tensile test model, because it has the shortest CPU time.

The sheet mesh of $60 \times 100 \times 1$ C3D8 elements is used for the forming sheet of the model for the superplastic forming of a rectangular box, because this mesh has the smoothest thickness results and it has the smallest penetration into the die mesh.

The sheet thickness is not significantly affected by the die mesh. Die mesh 2 is chosen for the die of the model for the superplastic forming of a rectangular box, because of the small sheet mesh penetration into the die with the sheet mesh of $60 \times 100 \times 1$ C3D8 elements.